https://doi.org/10.5194/amt-2022-14
Preprint. Discussion started: 21 April 2022

Atmospheric Measurement Techniques
Discussions

Atmospheric boundary layer height from ground-based remote sensing: a review of capabilities and limitations

Simone Kotthaus[1], Juan Antonio Bravo-Aranda[1,2,9], Martine Collaud Coen[3], Juan Luis Guerrero-Rascado[2,9], Maria João Costa[4], Domenico Cimini[5,6], Ewan J. O'Connor[7], Maxime Hervo[3], Lucas Alados-Arboledas[2,9], María Jiménez-Portaz[2,9], Lucia Mona[5], Dominique Ruffieux[3], Anthony Illingworth[8], and Martial Haeffelin[1]

[1]Institut Pierre Simon Laplace (IPSL), CNRS, École Polytechnique, Institut Polytechnique de Paris, 91128 Palaiseau Cedex, France
[2]University of Granada, Granada, Spain
[3]Federal Office of Meteorology and Climatology, MeteoSwiss, Payerne, Switzerland
[4]Earth Remote Sensing Laboratory (EaRSLab), Institute of Earth Sciences (ICT) and Physics Department, University of Évora, Évora, Portugal
[5]National Research Council of Italy, Institute of Methodologies for Environmental Analysis (CNR-IMAA), Potenza, Italy
[6]CETEMPS, University of L'Aquila, L'Aquila, Italy
[7]Finnish Meteorological Institute, Helsinki, Finland
[8]Department of Meteorology, University of Reading, Reading, United Kingdom
[9]Andalusian Institute for Earth System Research, Granada, Spain

Correspondence: Simone Kotthaus (simone.kotthaus@ipsl.fr)

Abstract. The atmospheric boundary layer (ABL) height defines the volume of air within which heat, moisture and pollutants released at the Earth's surface are rapidly diluted. Despite the importance for air quality interpretation, numerical weather prediction, greenhouse gas assessment and renewable energy applications, amongst others, quantitative knowledge on the temporal and spatial variation in ABL height is still scarce. With continuous profiling of the entire ABL vertical extent at high temporal and vertical resolution now increasingly possible due to recent advances in ground-based remote sensing measurement technology and algorithm development, there are also dense measurement networks emerging across Europe and other parts of the world. To effectively monitor the spatial and temporal evolution of the ABL continuously at continent-scale, harmonised operations and data processing are key. Autonomous ground-based remote sensing instruments, such as microwave radiometers, radar wind profilers, Doppler wind lidars or automatic lidars and ceilometers, each offer different capabilities. The overarching objective of this review is to emphasize how these instruments are best exploited with informed network design, algorithm implementation, and data interpretation. A summary of the capability and limitations of each instrument type is provided together with a review of the vast number of retrieval methods developed for ABL height detection from different atmospheric quantities (temperature, humidity, wind, turbulence, aerosol). It is outlined how the diurnal evolution of the ABL can be monitored effectively with a combination of methods, highlighting where instrument or methodological synergy promise to be particularly valuable. To demonstrate the vast potential of increased ABL monitoring efforts, long-term observational studies are reviewed summarising our current understanding of ABL height variations. The review emphasizes that harmonised data acquisition and careful data processing are key to obtaining high-quality products, which are essential to capture the spatial and temporal complexity of the lowest part of the atmosphere in which we live and breathe.

Contents

https://doi.org/10.5194/amt-2022-14
Preprint. Discussion started: 21 April 2022

1 Introduction

The Atmospheric Boundary Layer (ABL) is the lowest part of the atmosphere, defining the air we breathe, the winds harvested by wind turbines and the formation of fog or low-level clouds, amongst many other processes. It plays a crucial role for the exchange of momentum, heat, humidity, aerosols, as well as greenhouse and other atmospheric gases between the Earth's surface and the atmosphere (Palmén and Newton, 1969; Garratt, 1994; Stull, 1988). Improved process understanding and quantitative knowledge of ABL dynamics is hence crucial for a wide range of applications with high societal, economic and health impacts, including air quality assessment (Han et al., 2009), renewable energy generation (Peña et al., 2016), numerical weather prediction (NWP; Illingworth et al., 2019), sustainable urban planning (Barlow et al., 2017), and all aspects of transportation such as aviation, shipping, or road safety (Vajda et al., 2011). Still, the ABL presents the single-most under-sampled part of the atmosphere as its processes are not captured adequately, neither by surface-based station networks nor by the increasingly rich atmospheric profile data gathered by satellites. The latter reaching maximum uncertainty close to the Earth's surface (Zhang et al., 2016; Abril-Gago et al., 2021).

Sampling the ABL vertical profile has historically been mostly achieved using radiosonde. While these balloon ascends provide indispensable information, their temporal resolution is usually insufficient to capture the full diurnal evolution of the ABL dynamics. In recent decades, ground-based remote sensing has started to close this gap, providing high-resolution information, initially with a focus on the lowest kilometre of the atmosphere (see reviews by Wilczak et al., 1997; Emeis et al., 2008). Significant advances in ground-based remote sensing measurement technology and algorithm development now allow for continuous profiling of the entire ABL vertical extent at high temporal and vertical resolution (Illingworth et al., 2019; Cimini et al., 2020) and automatic detection of ABL layer heights from different atmospheric quantities (Collaud Coen et al., 2014; Duncan Jr. et al., 2021). With dense ground-based remote sensing networks emerging in Europe and other parts of the world, it is vital to recap capabilities and limitations of the various instruments and analytical approaches to support informed network design, algorithm implementation, and sound interpretation of the results.

The objective of this review is to provide a general overview on the latest ABL profiling techniques while making relevant details easily accessible. The sections hence offer multiple entry points (Figure 1) catering to a range of user backgrounds. The different atmospheric variables routinely analysed to gain insights on the ABL are presented in Section 1.1. Sensor types commonly used for ABL profiling are introduced in Section 2, highlighting their respective capabilities and limitations as well as their deployment in organised sensor networks. The wide range of ABL height retrieval methods is then reviewed in Section 3, linking potential retrieval errors to uncertainties inherent in the observed atmospheric quantity where appropriate. Quantification of layer height uncertainties is challenging, particularly due to the absence of an 'absolute truth' concept that could serve as the reference standard. Section 4 outlines how the various layer height retrievals based on different atmospheric quantities compare throughout the ABL diurnal evolution and depending on atmospheric stability or cloud conditions. This is to support a data users' assessment of how well a certain layer height product may characterise their process of interest. Finally, Section 5 provides an overview of the current knowledge on ABL heights globally, highlighting processes and geographic characteristics that drive spatial and temporal variations.

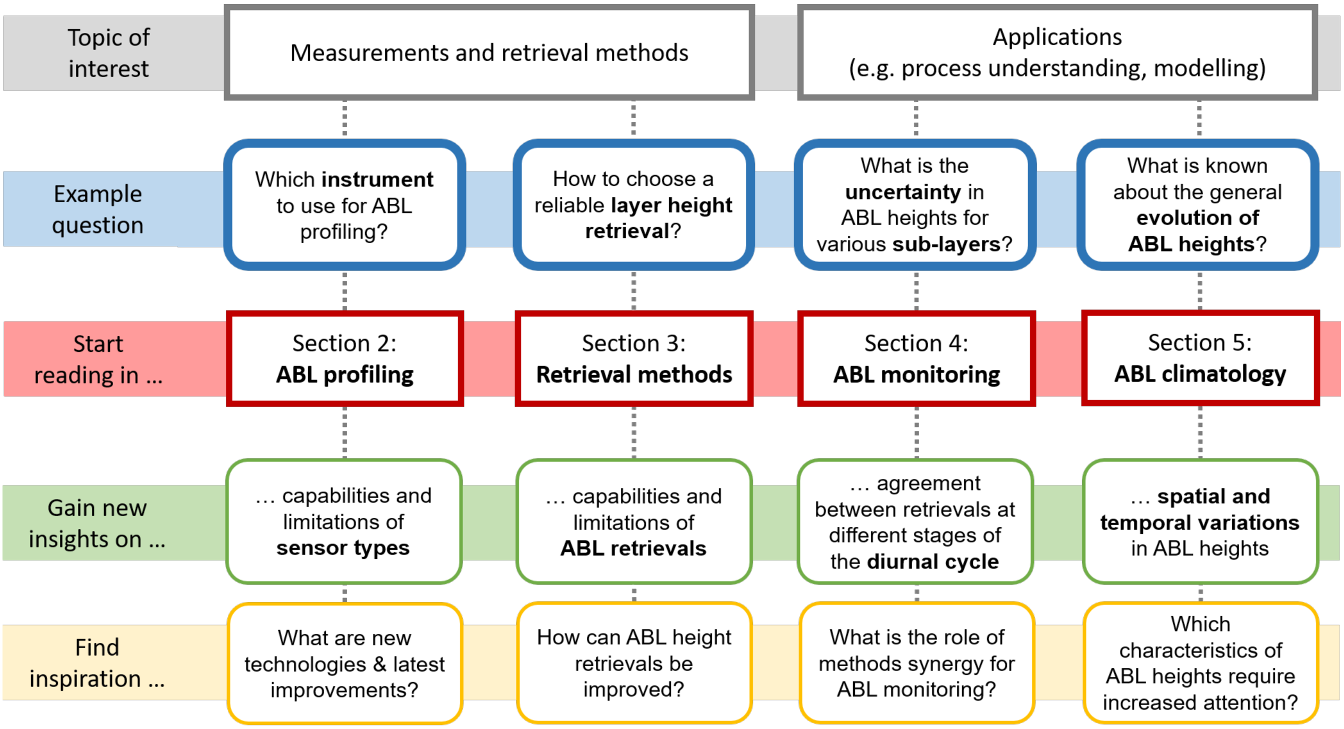

Topic of interest	Measurements and retrieval methods		Applications (e.g. process understanding, modelling)	
Example question	Which **instrument** to use for ABL profiling?	How to choose a reliable **layer height retrieval**?	What is the **uncertainty** in ABL heights for various **sub-layers**?	What is known about the general **evolution of ABL heights**?
Start reading in …	Section 2: **ABL profiling**	Section 3: **Retrieval methods**	Section 4: **ABL monitoring**	Section 5: **ABL climatology**
Gain new insights on …	… capabilities and limitations of **sensor types**	… capabilities and limitations of **ABL retrievals**	… agreement between retrievals at different stages of the **diurnal cycle**	… **spatial and temporal variations** in ABL heights
Find inspiration …	What are new technologies & latest improvements?	How can ABL height retrievals be improved?	What is the role of methods synergy for ABL monitoring?	Which characteristics of ABL heights require increased attention?

Figure 1. Entry points to this manuscript. The reader is invited to consult the respective section(s) related to their field of interest.

Ground-based profile remote sensing is a powerful tool to enhance our understanding of the atmospheric boundary layer. With careful, harmonised measurement network operations and processing procedures, increasingly detailed information can be collected that is very powerful to support many high-impact applications. The conclusions (Sect. 6) emphasise which aspects of data acquisition, algorithm development, data analysis and applications require additional attention to best advance this area of sensor development, scientific research and environmental monitoring operations.

https://doi.org/10.5194/amt-2022-14
Preprint. Discussion started: 21 April 2022

1.1 The atmospheric boundary layer and its sub-layers

The Atmospheric Boundary Layer[1] (ABL) is the lowest part of the troposphere where direct interactions with the Earth's surface (land and sea) take place (Seibert et al., 2000). It responds directly (or indirectly) to surface forcing at time scales of less than one hour (day) (Garratt, 1994). Exchange mechanisms include the transfer of momentum, radiation, heat, moisture, particles and gases. These can be driven by contrasts in surface cover, roughness, topography as well as wind shear (e.g., low-level jet) or cloud dynamics (Garratt, 1994; Seibert et al., 2000). The ABL defines the volume in which gases and aerosol particles emitted at the Earth's surface are primarily dispersed. Exchange with the free troposphere (FT) above takes place via ejection and entrainment processes (Stull, 1988).

The height of the ABL ($ABLH$) is here considered the height above ground where surface influence becomes low, i.e. the transition to the FT. Different sub-layers occur within the ABL depending on atmospheric stability. If surface-driven processes dominate over synoptic flow conditions on a warm, cloud-free day, the ABL tends to follow a textbook evolution (Figure 2) with a *convective boundary layer* (CBL) forming in the morning in response to solar heating of the ground and resulting turbulent heat fluxes. The height of the CBL ($CBLH$) increases during the morning and reaches its peak in the early afternoon when it extends over the whole ABL ($ABLH = CBLH$). Around sunset, radiative cooling of the surface induces the growth of a new layer near the ground, the *stable boundary layer* (SBL). At this time of reduced solar input and decaying buoyancy, the CBL breaks down and decouples from the surface, whereby converting into the *residual layer* (RL), now located above the SBL top ($SBLH$). The height of the RL top now coincides with the $ABLH$ ($ABLH = RLH$). On the following day again, the RL is usually entrained into the newly forming CBL during morning growth. While neutral atmospheric stability usually dominates the RL, it is less frequent near the surface (Collaud Coen et al., 2014) but may still occur when shear production of atmospheric turbulence is strong (Nieuwstadt and Duynkerke, 1996).

In response to surface-atmosphere exchanges, cloud processes or synoptic-scale dynamics, the ABL sub-layers often deviate from this idealised concept. In cold seasons or over cold surfaces (such as snow and ice), the SBL may also dominate during daytime and no RL may form leading to $ABLH = SBLH$ during both day and night. The vertical profile of air temperature in the SBL often shows a characteristic surface-based temperature inversion, whose height ($SBIH$) can be very meaningful in restricting vertical dilution. In the presence of a low-level jet (LLJ), jet core defines the top of the surface-based shear layer acting as an upper bound for turbulent transport (Banta et al., 2006; Mahrt et al., 1979).

But also unstable conditions may persist at night where the surface remains relatively warm even after sunset (e.g., urban areas). In this case, no SBL is present at night. Still, a shallow mixing layer may form around sunset (decoupled from the RL) as the nocturnal surface buoyancy is now only driven by storage (and potentially anthropogenic) heat fluxes and is hence weaker than the mixing during daytime. The term *mixing boundary layer* (MBL) is a general term referring here to the ABL sub-layer closest to the ground. Its height ($MBLH$) can refer to either $CBLH$ or $SBLH$, whichever is present at the given moment. The $MBLH$ terminology is applied when no information on atmospheric stability is available to differentiate between SBL and CBL.

---

[1] synonymous with the term *planetary boundary layer* (PBL), also commonly used

When buoyancy-driven turbulence is present, exchange between the CBL and the FT (or the RL) occurs via two processes: the penetration of the CBL thermals into the air aloft and the entrainment of warm and (in the absence of clouds) dry air into the CBL. The *entrainment zone* (EZ) refers to this region of interaction around the $CBLH$ and its depth (EZD) is related to the contrasts between the air in the CBL and the above FT (or RL), respectively. The EZ is associated with intermittent turbulence in time and a vertical decline in intensity of the turbulence (Gryning and Batchvarova, 1994). EZD is greater when the temperature gradient between ABL and FT is weak (AMS, 2017). At the top of the neutral RL or the SBL, the transition to the FT is marked by a strongly positive temperature lapse rate, the *capping inversion* (CI). The CI often coincides with a sharp vertical decrease in specific humidity and significant vertical wind shear.

The interaction of clouds and ABL dynamics depends on the cloud type (Harvey et al., 2013). Cumulus clouds (Cu) forming at the CBL top can be understood as generating a deep EZ and thus, the $ABLH$ may be located above the *cloud base height* (CBH), i.e. somewhere within the Cu. Radiative cooling in stratocumulus clouds (Sc) induces top-down mixing from the cloud layer toward the surface during day and night (Hogan et al., 2009; Wood, 2012) so that $ABLH$ may rather coincide with the cloud top. If deep convective clouds are present, e.g., cumulonimbus (Cb) before the occurrence of precipitation, the ABL may present higher relative humidity, greater instability, stronger temperature inhomogeneity and less wind shear (Zhang and Klein, 2010) so that it becomes challenging to define the $ABLH$.

Layers of gaseous species or aerosols (e.g., dust, smoke, ash) can be present in the FT, e.g., through long-range transport, volcanic eruptions or pyrocloud convection (Fromm et al., 2010; Lareau and Clements, 2016). The lofted layer may remain decoupled from the local ABL but can also be (partially) entrained (Granados-Muñoz et al., 2012; Bravo-Aranda et al., 2015). Over heterogeneous surfaces or complex topography, the ABL-FT exchanges become more significant (Lehning et al., 1998). Several passive (e.g., flow blocking, flow channeling and lee waves) and active (thermally driven wind systems such as valley and slope winds or plain to mountain transport) mechanisms are involved in the ABL behavior and in vertical transport exchanges over complex terrain (De Wekker and Kossmann, 2015; Serafin et al., 2018). The ABL over mountainous terrain ($MoBL$) often exhibits a complex multilayered structure with successive stable and turbulent layers leading to three-dimensional patterns (Finnigan, 2003; Lehner and Rotach, 2018) that are influenced by micro- to mesoscale effects in time scales of up to one day.

https://doi.org/10.5194/amt-2022-14
Preprint. Discussion started: 21 April 2022

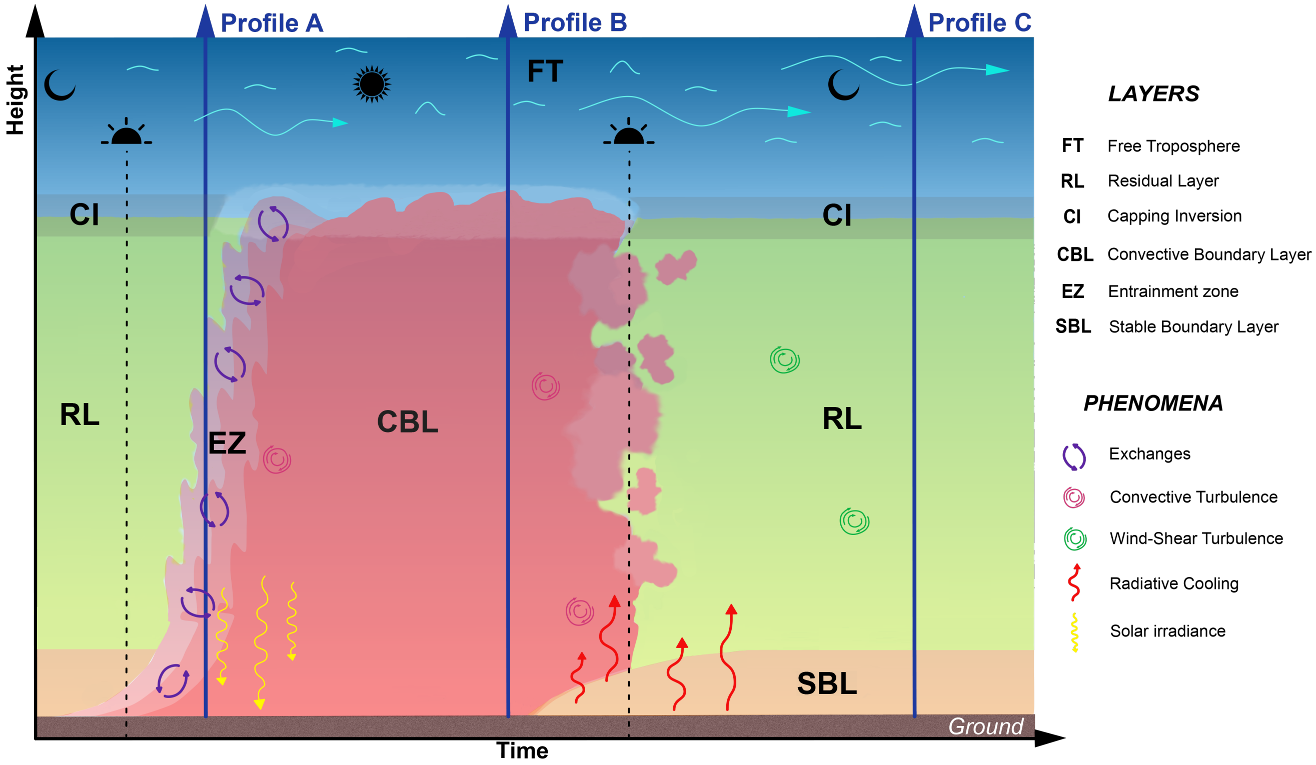

Figure 2. Idealised evolution of the atmospheric boundary layer (ABL) over flat terrain on a cloud-free day. Vertical dashed lines mark times of sunrise and sunset. Idealised vertical profiles of different atmospheric variables at times A, B, and C (here marked by vertical blue arrows) are shown in Figure 3.

2 Atmospheric boundary layer profiling

As stated by Beyrich (1997), profile observations should fulfill a series of requirements to adequately support the assessment of ABL dynamics and the detection of layer heights. Namely, they should (i) cover the full extent of the ABL (from the ground to the FT), (ii) have high vertical resolution of about 10-30 m, (iii) high temporal resolution of $\leq$1 h, and (iv) describe either the mixing itself or a result of mixing processes. We add that data with high temporal coverage (e.g., long time series) are necessary to determine variations in ABL dynamics at different temporal scales (synoptic, seasonal, annual, inter-annual) and measurements at multiple geographic locations enable horizontal variations to be assessed. Adequate atmospheric profiles (Sect. 2.1) can be captured by a series of different technologies (Sect. 2.2) that are increasingly operated in coordinated measurement networks (Sect. 2.3).

https://doi.org/10.5194/amt-2022-14
Preprint. Discussion started: 21 April 2022

2.1 Profile variables characterising the atmospheric boundary layer structure

Different quantities provide insights on ABL dynamics and can be analysed to derive the heights of the various sub-layers (Sect. 1.1). While *thermodynamic variables* capture atmospheric stability conditions at a given moment, *dynamic variables* describe the mixing processes induced by this stratification and *tracer variables* portray the result of recent mixing processes (Table 1). Figure 3 indicates how vertical profiles of selected exemplary atmospheric variables change throughout the idealised evolution of the ABL on a cloud-free day (Figure 2).

These variables can either be *measurement variables* that are somewhat defined by the observation technology and setup (e.g., radial velocity obtained by a Doppler wind lidar along its laser line-of-sight; Sect. 2.2.3) or *atmospheric variables* that describe a physical process or characteristic of the air rather independently of the observation technique. Some atmospheric variables are output directly by a certain sensor (e.g., air temperature measured with an in-situ thermometer of a radiosonde; Sect. 2.2.1), while others are retrieved during post-processing following methods of various complexity. Certain variables are calculated as a combination of multiple variables (e.g., potential temperature calculated from air temperature and atmospheric pressure, colour ratio determined from backscatter coefficient observed at two different wavelengths) or by applying higher order statistics (e.g., variance of vertical velocity) or both (e.g., turbulent kinetic energy calculated from variances of the three wind velocity components). Other variables require more complex retrieval algorithms, with a series of assumptions (e.g., retrieval of wind speed components from Doppler radial velocity) and even auxiliary information (e.g., retrieving air temperature from microwave radiometer brightness temperature).

Both atmospheric variables and measurement variables can be exploited for ABL height detection (Sect. 3). Those most commonly utilised, can be grouped by their physical relation to ABL dynamics (Table 1).

https://doi.org/10.5194/amt-2022-14
Preprint. Discussion started: 21 April 2022

Physical meaning	Measurement and atmospheric variables
thermodynamic processes	brightness temperature (T_b)
	air temperature (T)
	potential temperature (θ)
	virtual potential temperature (θ_v)
	relative humidity (RH)
	specific humidity (q)
	water vapour mixing ratio (r)
dynamic processes	refractive index structure parameter (${C_n}^2$)
	radial velocity (v_r)**
	horizontal wind speed (U)
	velocity components of the wind vector (u, v, w)
	variances of the velocity components (${\sigma_u}^2$, ${\sigma_v}^2$, ${\sigma_w}^2$)
	turbulent kinetic energy (TKE)
	eddy dissipation rate (ϵ)
tracers	attenuated backscatter coefficient (β_{att})
	mass or number concentration of particles and gases (ρ or c)
	volume depolarisation ratio (δ)
	particle depolarisation ratio (δ_p)
	particle extinction coefficient (α_p)
	particle backscatter coefficient (β_p)
	colour ratio
	signal-to-noise ratio (SNR)**
	carrier-to-noise ratio (CNR)**

Table 1. Atmospheric variables analysed for detection of ABL heights are relevant for thermodynamic and dynamic processes or act as atmospheric tracers. ***Measurement variables* (e.g., v_r, SNR) provide information on the probed atmosphere but are strongly dependent on sensor characteristics or measurement setup. Depending on the measurement technology, variables are directly observed, retrieved from measurements or calculated. Note: humidity can also be interpreted as an atmospheric tracer but is here grouped with air temperature due to its importance for thermodynamic processes.

https://doi.org/10.5194/amt-2022-14
Preprint. Discussion started: 21 April 2022

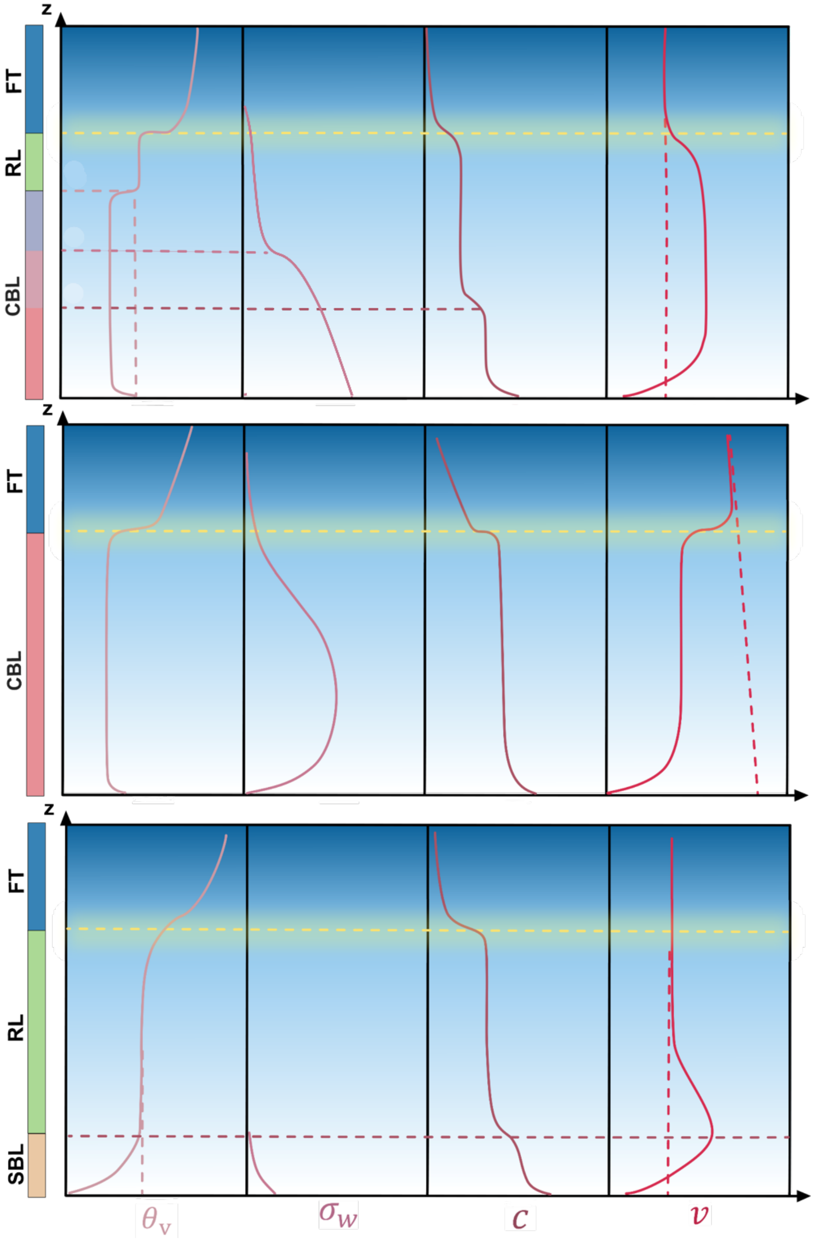

Figure 3. Idealised vertical profiles of exemplary atmospheric thermodynamic (mean virtual potential temperature θ_v), dynamic (vertical velocity standard deviation σ_w, mean horizontal velocity v), and tracer (mean atmospheric constituent c) variables at three selected times during the diurnal evolution of the atmospheric boundary layer (ABL, Figure 2) with the free troposphere (FT) above and extent of sublayers indicated by the sidebar: (top) morning growth of the convective boundary layer (CBL) into the residual layer (RL), (middle) peak CBL development, and (bottom) nocturnal stable boundary layer (SBL). Yellow horizontal dashed line and shading mark the height of the ABL. Horizontal pink line in (bottom) indicates the height of the SBL. Horizontal pink lines in (top) indicate height of the CBL depending on the indicator used; note those height contrasts are here exaggerated and the exact relation between heights derived from different indicators is subject to ongoing research. Idealised profiles adapted from De Wekker and Kossmann (2015); Beyrich (1997); Stull (1988).

https://doi.org/10.5194/amt-2022-14
Preprint. Discussion started: 21 April 2022

2.2 Measurement principles

A range of technologies (Table 2) is available to measure the quantities (Sect. 2.1) analysed for layer detection (Sect. 3). Atmospheric profile measurements can be achieved using tower-based or airborne in-situ sensors (Sect. 2.2.1) or with remote sensing techniques that again can be air-borne, space-borne or ground-based, respectively. While some passive radiometer technologies capture thermodynamic profiles (Sect. 2.2.2), most approaches actively emit a signal which is then record after its interaction with the probed atmosphere.

In addition to the ground-based techniques that are focus of this review, some ABL information can be gathered by space-borne technologies, including aerosol lidars (e.g., Cloud-Aerosol Lidar and Infrared Pathfinder Satellite Observations (CALIPSO); Jordan et al., 2010; Liu et al., 2015a; Zhang et al., 2016), Doppler wind lidars (e.g., Atmospheric Laser Doppler Instrument (Aeolus-ALADIN); Straume et al., 2020; Flamant et al., 2016), or radio-occultation systems (Global Navigation Satellite System Radio Occultation (GNSS-RO); von Engeln et al., 2005; Ao et al., 2012; Xie et al., 2012; Chan and Wood, 2013; Basha and Ratnam, 2009). Satellite microwave and near-infrared passive observations also allow for the quantification of boundary layer water vapor even beneath uniform marine clouds (Millán et al., 2016). Given their spatial coverage, space-borne data are particularly meaningful for global-scale analyses (Sect. 5). However, satellite observations are less applicable for the detection of very shallow layers (e.g., Aeolus-ALADIN is not suitable for the monitoring of shallow layer conditions, Abril-Gago et al., 2021) or sublayer heights (such as $SBLH$ and RLH) given the degradation of profiles at low altitudes above the surface (Seidel et al., 2010; Xie et al., 2012) and the relatively coarse horizontal resolution (e.g., ∼200 km for GNSS-RO and ∼87 km for Aeolus), which introduces additional uncertainty over coastal regions as well as in presence of complex terrain (Ao et al., 2012). Still, satellite-based ABL layer heights are very valuable, as they provide globally consistent estimates (Ho et al., 2015) whose seasonal cycle constitutes an important constraint on the behaviour of global atmospheric models (Chan and Wood, 2013; Liu et al., 2015a).

Ground-based remote sensing profilers generally provide data with the highest temporal and vertical resolution and best sensitivity in the ABL. The profiling sensors most commonly used to observe the ABL are here briefly introduced, grouped according to their characteristic output variables into thermodynamic profilers (Sect. 2.2.2), wind and turbulence profilers (Sect. 2.2.3), as well as lidars for the detection of aerosols and gases (Sect. 2.2.4). For further technical details, the reader is referred to relevant textbooks (e.g., Emeis, 2010).

2.2.1 In-situ profiling

In-situ sensors are attached to various kinds of platforms to gather atmospheric profile measurements. Instruments operated at multiple levels on **tall towers** are capable of capturing conditions in the lowest few hundred metres of the atmosphere based on profiles of temperature, humidity, wind, turbulence or atmospheric composition (Bosveld et al., 2020; Ramon et al., 2020; Neisser et al., 2002), often continuously at very high temporal and vertical resolution. A similar range of the atmospheric column can be probed by instruments hosted on **tethered balloons** (Keller et al., 2011; Spirig et al., 2004), however, the latter

Table 2. Instrument types used to gather vertical profiles of atmospheric and measurement variables (Sect. 2.1; Table 1) in the atmospheric boundary layer. These observations are increasingly organised in national and international monitoring networks (see Sect. 2.3 for definition of acronyms and further details)

Instrument type	Measurement and atmospheric variables	Network operations
airborne in-situ meteorological sensors	T, θ, θ_v, RH, u, v	IGRA, AMDAR
airborne in-situ chemistry sensors	ρ, c	IAGOS
microwave radiometer (MWR), infrared spectrometer (IRS)	T_b, T	EUMETNET E-PROFILE, ACTRIS-CCRES, MWRnet
differential absorption lidar (DIAL)	T, r, ρ, c	ACTRIS-CREGAR, NDACC
radio acoustic sounding system (RASS)	T	
Raman lidar	r, ρ, c	NDACC
Doppler wind lidar (DWL)	v_r, u, v, w, σ_w, σ_u, σ_v, TKE, ϵ	EUMETNET E-PROFILE, ACTRIS-CCRES
Radar wind profiler (RWP)	u, v, w, σ_w, σ_u, σ_v	EUMETNET E-PROFILE
sodar	c_n^2	
Automatic lidars and ceilometers (ALC)	β_{att}, δ	EUMETENET E-PROFILE, ACTRIS-CCRES, ACTRIS-CARS
Aerosol lidar	β_{att}, β, α_p, δ, δ_p	CARS-ACTRIS, EARLINET, LALINET

are still mostly operated manually during dedicated field campaigns only. Such methods are sometimes used in conjunction with radon measurements (Griffiths et al., 2013; Williams et al., 2013).

Other airborne measurements of meteorological variables and atmospheric composition tend to reach higher atmospheric levels, including in-situ sensors attached to radiosonde balloons or on board of airplanes or **uncrewed aerial systems (UAS)**. UAS can gather data at very high temporal and vertical resolution often covering the full vertical extend of the ABL, however, they can not (yet) be operated fully autonomously and temporal coverage is often limited. Similarly, data from research aircraft flights (e.g., Guimarães et al., 2019) are scare. The air volume sampled by both UAS and research aircraft flights can be restricted by air traffic control regulations. **Networks of commercial passenger airplanes** gather atmospheric profile information more continuously. The initiatives *Aircraft Meteorological Data Relay*[2] (AMDAR) and *In-service Aircraft for a Global Observing System*[3] (IAGOS) collect e.g. temperature, humidity, wind speed, wind direction, and various atmospheric constituents during their flights whereby gathering vertical profile data near the airports during start and landing. Observation accuracy is generally similar to that of radiosondes (Berkes et al., 2017), however, the vertical resolution is lower and systematic biases have been reported (e.g., AMDAR air temperature bias of up to 0.5-1.0 K; Ballish et al., 2008). Further, the airplane flight paths are associated with a much greater horizontal displacement ($\sim$10 km km^{-1}) than radiosondes ($\sim$ 1 km km^{-1};

---

[2] https://public.wmo.int/en/programmes/global-observing-system/amdar-observing-system

[3] https://www.iagos.org/

Rahn and Mitchell, 2016). Naturally, the temporal resolution of IAGOS and AMDAR profiles depends on the frequency of reporting airplanes starting or landing in the region of interest. AMDAR data have been applied successfully to study the ABL in regions with multiple busy airports in close vicinity, such as Los Angeles, USA, (Rahn and Mitchell, 2016), London, UK, (Kotthaus and Grimmond, 2018a) or Paris, France, (Kotthaus et al., 2020), while Petetin et al. (2018) derive generalised ABL profiles for Northern hemisphere mid-latitudes from a climatology of IAGOS profiles.

Radiosondes are probably the most common data source used to derive $ABLH$ operationally. In-situ measurements of air temperature, pressure, humidity, and wind speed and direction are taken by sensors that are being lifted up by an helium-inflated aerostatic balloon. The balloon ascent allows profiles to be recorded up to ∼35 km above ground level (a.g.l.) with high and nearly constant vertical resolution at the order of tens of meters. The sounding takes 1.5-2.0 h to reach the maximum altitude before the balloon bursts (usually in the lower stratosphere). Typical uncertainties in radiosonde measurements are ±0.2-0.6 K for air temperature, 6 % for relative humidity, and 0.4-1.0 m s^{-1} for horizontal wind speed (Bian et al., 2011; Dirksen et al., 2014; Renju et al., 2017). Lightweight sondes attached to smaller balloons (Elie Quentin Bessardon et al., 2019) are not able to profile the entire troposphere, however, they usually ascend to heights above the $ABLH$. As they are technically easier to operate and do not require specific security clearance they are particularly useful for ABL profiling in populated environments such as cities.

The main advantages of radiosonde data are: (i) observations of temperature, pressure, humidity, wind speed and direction are collected simultaneously; (ii) coordinated radiosonde ascents are available at a high number of launch sites worldwide (Sect. 2.3); (iii) data are transmitted via international communication networks with very short time delay which makes them well-suited for operational use; and (iv) time series extend for decades, making radiosondes especially valuable for climatology studies (Sect. 5). It should be noted however, that only 177 sites (status 2021) meet the stringent requirements for climate monitoring (CIMO-TECO, 2018; Thorne et al., 2017; WMO, 2010).

The main shortcoming of radiosondes is their low temporal frequency. Most operational sites only launch the balloons twice daily at specified synoptic times (00 UTC, 12 UTC), with some up to four times daily. Even during special field campaigns, 1.5-3.0 h is typically the closest interval between launches. This low temporal resolution hampers the investigation of the diurnal cycle of ABL sub-layer heights and the comparison of $ABLH$ maxima at different locations. Note that some radiosonde data products of routine ascends limit the vertical information to standard, significant pressure levels for real-time dissemination and archiving. If such data sets are being explored, details of the ABL structure may be obscured. Other specific problems that can result in systematic errors in derived ABL characteristics include humidity sensor uncertainties in cold and dry or cloudy conditions (Seidel et al., 2010; Wang and Wang, 2014), errors in the wind profiles at low levels that can be caused by site-dependent tracking (Seibert et al., 2000), and significant horizontal displacement of the balloon (Schween et al., 2014).

2.2.2 Thermodynamic profiling

Different ground based remote-sensing technologies are available to obtain vertical profiles of air temperature and humidity: Raman lidars or differential absorption lidars (DIAL; see Sect. 2.2.4), radio-acoustic sounding systems (RASS), and radiometers.

https://doi.org/10.5194/amt-2022-14
Preprint. Discussion started: 21 April 2022

The standard **RASS** configuration combines a radar wind profiler with a source of acoustic pulses (e.g., sodar) transmitted into the vertical beam of the radar (e.g., Emeis, 2010). The frequency of the acoustic pulses are varied in time and Bragg scattering of the radar signal occurs when the wavelength of the acoustic pulse is half the wavelength of the radar. The Doppler shift of the Bragg-scattered radar signal provides the speed of sound as a function of altitude, from which the profile of virtual temperature can be deduced. The uncertainty in temperature can be < 0.5 K (Görsdorf and Lehmann, 2000). Temporal resolution depends on the application with 10 minutes averaging being typical. The vertical resolution of the profile depends on the length of the pulse transmitted by the radar, with RASS systems usually configured to have a resolution of 30-60 m. Although it is possible to obtain measurements above 1 km, the maximum range is usually about 500 m. However, as the acoustic signal disturbs both humans and animals RASS profiling is now rarely deployed despite its capability.

Two types of ground-based profiling radiometers measure the downwelling radiance naturally emitted by the atmosphere at selected band channels: **microwave radiometers (MWR)** and **infrared spectrometers (IRS)**. The measured radiance is internally converted to atmospheric brightness temperature (T_b). As T_b holds information on atmospheric thermodynamic conditions, further atmospheric variables (e.g., temperature, humidity, water liquid path and integrated water vapour content) can be derived, using retrieval methods aided by some *a priori* knowledge. The atmospheric variables obtained from MWR and IRS depend on the number and spectral range of channels utilised by a given sensor.

In the 20-60 GHz frequency (0.5-1.5 cm wavelength) range, the atmospheric thermal radiance is mostly emitted by atmospheric gases (primarily oxygen and water vapour) and hydrometeors (mainly liquid water droplets). MWR operating at several channels in the 20-30 GHz and 50-60 GHz frequency bands observe temperature and humidity profiles, respectively. Vertical resolution of the obtained temperature profiles is higher in the lowest 2 km where most of the information content resides. For humidity profiles the information is spread along the vertical range with generally coarser resolution. Most common MWR profilers provide information on tropospheric temperature and specific humidity and the column-integrated liquid water content (Solheim et al., 1998; Westwater et al., 2004; Rose et al., 2005) at high temporal resolution (∼1 min). When compared to nearby radiosonde ascents, MWR retrievals agree within 0.5-2.0 K root mean square error (RMSE) for temperature (decreasing from surface up) and 0.2-1.5 g m^{-3} for absolute humidity. The mean RMSE value within the boundary layer is ∼0.8 K for the temperature retrievals (Liljegren et al., 2005; Cimini et al., 2006; Löhnert et al., 2009; Löhnert and Maier, 2012). IRS exploit high spectral resolution radiances measured in the thermal infrared spectrum to retrieve temperature and water vapor profiles in cloud-free air. The Atmospheric Emitted Radiation Interferometer (AERI) is a Fourier transform IRS operating in the thermal infrared range (3000-520 cm^{-1} wavenumber, 3.3–19 μm wavelength) (Knuteson et al., 2004a, b) specifically designed to record downwelling radiance at high spectral resolution ($0.5\ cm^{-1}$). The observed radiance observed is processed to retrieve temperature and water vapor profiles up to cloud base, and in addition cloud properties and trace-gas concentrations (Feltz et al., 2003; Turner and Löhnert, 2014; Turner and Blumberg, 2018), with a temporal resolution of 30 s. When compared to nearby radiosonde ascents, IRS retrievals agree within 1 K RMSE for temperature and ∼0.8 g kg^{-1} for water vapor mixing ratio (e.g., Blumberg et al., 2015; Wulfmeyer et al., 2015; Weckwerth et al., 2016). Synergy of IRS with active remote sensing technologies, such as DIAL or Raman lidar temperature profiling, can help to achieve an improved accuracy of the moisture gradient across the entrainment zone (Smith et al., 2021).

https://doi.org/10.5194/amt-2022-14
Preprint. Discussion started: 21 April 2022

MWR and IRS techniques both measure atmospheric natural radiation that is then inverted to estimate thermodynamic variables. Thermodynamic profiles from MWR or IRS have been demonstrated to be useful to estimate $ABLH$ (Cimini et al., 2013) and atmospheric stability indices (Feltz and Mecikalski, 2002; Wagner et al., 2008; Cimini et al., 2015). However, despite their similarities they provide partially complementary information. In general, IRS data have greater information content than MWR, resulting in higher vertical resolution for temperature and humidity profiles, and sensitivity to trace gases and cloud particle size. IRS also provides higher sensitivity to low cloud liquid water path, though the signal saturates above ∼40 g m^{-2}. MWR again are only slightly affected by liquid water, which gives them an advantage in capturing profiles even within or above clouds (unlike IRS, which is limited to cloud base). Further can MWR be used within light precipitation (Cimini et al., 2011; Bianco et al., 2017) because the antenna is protected by a radome with hydrophobic coating and a continuous tangential air flow. Still, periods under precipitation are usually excluded from analysis, as the above measures may not be sufficient under moderate to heavy precipitation, thus degrading the quality of retrieved profiles.

The most prominent limitation of ground-based radiometric profiling is its low-to-moderate vertical resolution. The information content of ground-based radiometry on the vertical distribution of atmospheric thermodynamics resides in the differential absorption of multi-frequency and multi-angle observations. However, contributions from different layers to the observed T_b (i.e. the weighting functions, Westwater et al., 2004) show significant overlap, leading to substantial redundancy in the observations. Although the retrievals of atmospheric profiles from passive instruments like MWR and IRS are usually provided on fine vertical grids (e.g., ∼50, 100, and 250 m at <500 m, 500–2000 m, and >2000 m, respectively), this spacing should not be confused with the actual vertical resolution, which by definition is the minimum distance at which differences in the vertical profile can be appreciated. More than one method is used to quantify the vertical resolution of radiometric profiling, e.g., degrees of freedom for signal (DFS), the inter-level covariance, and averaging kernels. Löhnert et al. (2009) showed that for a generic MWR operating in the 20-60 GHz range the DFS, i.e. the number of independent levels that can be retrieved, range from 1 to 4 for both temperature and humidity profiles. In more detail, for temperature profiles the DFS strongly depend on the number of elevation observations (from DFS 2 for zenith only to DFS 4 for some 10 elevation angles) but only slightly on atmospheric conditions, while for humidity the DFS are almost independent of the number of elevation observations but depend noticeably on the water vapor content (from DFS 1-2 at mid-latitude to DFS 2-3 at tropics). In general, DFS are higher for IRS than for MWR, but also more dependent on atmospheric conditions. For temperature (humidity) IRS DFS vary from 4-9 (4-10) in mid-latitudes to 3-5 (3-7) in the tropics.

Liljegren et al. (2005) used the inter-level covariance (ILC) to quantify the vertical resolution of radiometric profiles. For ground-based MWR profilers, ILC typically decreases almost linearly with height (z): for temperature, ILC ranges from ∼100 m at the surface to ∼6 km at 10 km (ILC ∼0.5·z + 0.1 [km]); for absolute humidity, ILC increases from ∼400 m at the surface to ∼3.5 km at 10 km (ILC ∼0.3·z + 0.4 [km]) (Cimini et al., 2006). ILC for temperature profiles can be kept within 1 km throughout the vertical domain by adopting an optimal estimation inversion method initialized with NWP analysis (i.e. 1DVAR, Cimini et al. (2006)). Blumberg et al. (2015) use the vertical resolution definition proposed by Rodgers (2000), i.e. the reciprocal of the diagonal of the averaging kernel matrix, to compare vertical resolutions of MWR and IRS. For temperature profiles they report a vertical resolution that varies linearly with height as by a factor of ∼2 for MWR and ∼1.4 for IRS, respectively. For example, at 1.5 km the temperature vertical resolution is ∼2 km for IRS while ∼3 km for MWR. The vertical resolution for the water vapor mixing ratio is less regular, but still roughly linearly with height (∼z+1 [km] for IRS).

Di Girolamo et al. (2020) reports results from an inter-comparison effort involving water vapor and temperature sensors, such as one MWR, two ground-based Raman lidars, one airborne water vapor DIAL, as well as airborne in-situ sensors (radiosondes, aircraft). At 5 min integration time, bias values between MWR and Raman lidar are within ±0.4 g kg^{-1} (or ±20 %) for water vapor mixing ratio measurements, while root mean square deviations are smaller than 1 g kg^{-1} (25-55 %). For temperature measurements, bias values are within 0–1.2 K and root mean square deviation values are 0.6-1.8 K. Similarly, Bianco et al. (2017) reports results from an inter-comparison effort involving two MWR and two RASS, as well as radiosondes and instrumented tower. For the layer of the atmosphere covered by the RASS, results show lower statistical differences with respect to radiosondes for RASS than the MWR. Methods to combine MWR and/or IRS with active instruments, such as DIAL and RASS, have also been proposed (e.g., Turner and Löhnert, 2021; Djalalova et al., 2021).

To summarise, passive radiometers provide better coverage of temperature and humidity profiles compared to research lidars because they can gather data continuously. Vertical resolution is greater for IRS between 0.5-2.0 km and greater for MWR above 4 km; IRS and MWR provide partially complementary information despite their substantial similarities, given the higher vertical information content of IRS in the ABL and the capability of the MWR to gather information within and above clouds and within light precipitation.

2.2.3 Wind and turbulence profiling

Several technologies allow for the vertical profiles of mean wind speed, direction and turbulence to be captured, including sodars, radar wind profilers (RWP) and Doppler wind lidars (DWL). Where profiles of both turbulence and temperature fluctuations (e.g., from RASS; Sect. 2.2.2) are observed, profiles of turbulent heat fluxes can be obtained (Engelbart and Bange, 2002; Behrendt et al., 2020).

Sodars send out pulses of sound to probe the atmosphere. The sodar technique is based on fluctuations in the refractive index of the air (Sect. 2.1) and the amplitude of the return signal is related to the structure function for temperature (CT^2; Singal, 1997; Bradley, 2007). Based on these, turbulent structures in the ABL can be characterised (Emeis et al., 2008; Kramar et al., 2014). Compared to most other remote sensing profiling systems, sodars have a particular advantage in being capable of sensing close to the instrument, typically within 20 m, hence very shallow ABL can also be measured even in challenging polar locations (Kouznetsov, 2009), especially when combined with sonic anemometers (Argentini et al., 2005). Their main disadvantage is that the sound signal can often be a disturbance for humans and animals which makes them difficult to operate continuously in many locations.

RWP operate on Doppler technology, either in the the very-high frequency (VHF) domain (20-300 MHz) or ultra-high frequency (UHF) domain (0.4-2 GHz) with boundary layer RWP usually around 1 GHz (*L-Band*). UHF RWP are better suited for probing the ABL thanks to their higher vertical resolution and lower cost. An electromagnetic pulse is emitted towards the zenith and two to four 15°-tilted, off-zenith directions. The angle can be achieved with different antennas or with a single phased-array antenna. In the UHF band, the return signal intensity depends mainly on humidity and temperature gradients in the atmosphere. It is recorded and analyzed in real-time by the system: a succession of coherent averaging and noise filtering steps are followed by a fast Fourier transform (FFT). The frequency spectrum obtained for each range gate is characterized by four moments: noise level, signal power, spectral width and Doppler shift. By combining the Doppler shift of the three beams, mean wind speed and wind direction are calculated at each range gate (Ecklund et al., 1988). Vertical resolution is at the order of 100-400 m, depending on the measurement setup.

The main advantage of RWP is their capability to operate under all weather conditions at moderate cost. They even provide useful information inside cloud or fog layers and when aerosol concentrations are very low, an advantage over most lidar systems. Large errors in RWP profile data are mostly caused by larger objects, such as birds (Lehmann and Teschke, 2008). RWP complement DWL observation capabilities and, provided suitable scan patterns, averaging strategies and quality control, the uncertainties and biases in RWP profiles are comparable to DWL. With less than 100 RWP operated worldwide (Sect. 2.3), their limited number is a clear disadvantage when it comes to spatial coverage.

DWL are active remote sensing systems similar to aerosol backscatter lidars (Sect. 2.2.4). There are two types of DWL: one uses the molecular backscatter component and applies narrow-band spectral filters to measure the frequency shift while the other type (*heterodyne Doppler lidar*) uses the aerosol-particle backscatter component and coherent mixing with a reference beam to detect the Doppler shift between the emitted and backscattered radiation. Ground-based commercial DWL capable of probing the full depth of the ABL typically use the heterodyne principle. They generally operate at wavelengths between 1.5-2.0 μm, taking advantage of components developed for the telecommunication industry.

Heterodyne DWL work with continuous-wave technology or by emitting short-laser pulses. For continuous-wave heterodyne systems, the radiation transmission is continuous and the range information is obtained through varying the focus of the telescope. The maximum range for continuous-wave DWL systems is limited to about 250 m as the range-weighting function becomes very broad beyond this distance (Kavaya and Suni, 1991). Pulsed DWL systems emit very short pulses of radiation and the range information is obtained from the round trip time between the transmit pulse and the received echo. The maximum unambiguous range is greater than for continuous-wave systems and depends on the pulse repetition frequency. For example, a pulse repetition frequency of about 15 kHz corresponds to a maximum unambiguous range of about 10 km. Wind velocity information is obtained through measuring the slight shift in frequency between the outgoing pulse and the backscattered return. This Doppler frequency shift can be measured directly, using different types of interferometers such as Fabry-Perot, Mach-Zehnder, or Michelson interferometers. DWL using this so-called *direct-detection* usually operate at visible and UV wavelengths (e.g., 532 or 355 nm) and are optimised towards backscattering from molecules (e.g., Lolli et al., 2013). The frequency shift can also be measured using the heterodyne principle, where the return signal is mixed with a stable local oscillator signal of known frequency and converted to an electrical signal by a quadratic detector (Grund et al., 2001). Since the frequency of the local oscillator signal is known, the original frequency shift can be determined from the measured heterodyne or 'beat' frequency. Given their negligible terminal fall velocities, backscattering aerosol particles and cloud droplets are ideal tracers to track the wind motion. All DWL exploit the Doppler shift along the line-of-sight, or *radial*, to measure the *radial Doppler velocity*. Note that attenuated backscatter (Sect. 2.1) can also be retrieved from DWL observations, if the instrument telescope function is accounted for (Pentikäinen et al., 2020).

https://doi.org/10.5194/amt-2022-14
Preprint. Discussion started: 21 April 2022

Pointing to nadir (zenith), the radial Doppler velocity observed from aerosol or cloud droplets is the vertical air motion w; for larger particles the observed radial Doppler velocity is the sum of the vertical air motion speed w and the fall velocity of the particles. For beams tilted away from zenith, the radial Doppler velocity contains components of both the horizontal wind and the vertical motion. Combining scans from multiple directions permits the horizontal wind component to be derived using trigonometry under the assumption of horizontal homogeneity of the wind field in the observed volume (Banta et al., 2013; Päschke et al., 2015; Teschke and Lehmann, 2017). Comparisons with sonic and cup anemometers on towers or masts show that winds can be derived from DWL with sufficient accuracy for wind energy applications (Peña et al., 2008; Pichugina et al., 2012). In ideal conditions, the DWL precision is within the uncertainty of the anemometer measurements used as a reference (Gottschall et al., 2012).

If winds are sampled at very high temporal frequency, higher order moments, such as velocity variances (Sect. 2.1) and even skewness, kurtosis, turbulent kinetic energy (TKE) or eddy dissipation rate (ϵ) can be determined (e.g., Cohn, 1995). Being direct measures of turbulence, TKE and ϵ are best suited for fair site and instrument inter-comparisons and can be obtained from various scan strategies, including vertical stare, multi-beam, conical scanning (Banakh and Smalikho, 1997; Banakh et al., 2010; Sathe et al., 2015; Bonin et al., 2017; Smalikho and Banakh, 2017; Yang et al., 2020), or a combination of scan types (Bonin et al., 2018). TKE can also be obtained by scanning at the specific elevation angle of 35.5° (Eberhard et al., 1989). These methods usually include measurements of the wind profile to provide the horizontal length scales required (O'Connor et al., 2010). Combining observations from multiple instruments permits direct retrievals of the three-dimensional wind vector and its fluctuations (Sathe and Mann, 2013). DWL retrievals of the physical quantities describing atmospheric turbulence have been successfully evaluated against data gathered by sonic anemometers on masts (Bonin et al., 2016; Bodini et al., 2018; Bonin et al., 2018), tethered-balloons (Frehlich et al., 2008; O'Connor et al., 2010), radiosondes (Tucker et al., 2009), or a combination of these (Wildmann et al., 2019). For a review on pulsed DWL including descriptions of the various scan strategies, the reader is referred to e.g., Liu et al. (2019b).

The intrinsic uncertainty in the measured Doppler radial velocity is directly related to the DWL SNR (Rye and Hardesty, 1993; O'Connor et al., 2010). As the latter depends on both the lidar system and the aerosol load of the atmosphere, uncertainty estimates should take into account the sampling strategy and potential instrument-specific corrections (Manninen et al., 2016; Vakkari et al., 2019). Increased uncertainties have been reported in pristine conditions such as the Arctic (e.g., Hirsikko et al., 2014). As for all lidar systems (Sect. 2.2.4), the incomplete optical overlap of DWL usually means data in the lowest range gates need to be treated with caution and are often discarded from analysis. For DWL that are able to gather profiles up to several kilometres range and are hence able to capture $ABLH$ peaks during deep afternoon convection this *blind zone* may hinder the assessment of very shallow ABL sublayers. Other *mini*DWL systems can observe wind profiles also in the very near range at high vertical resolution but then have the trade-off of a maximum range limited to several hundred metres (generally <1 km). The issue of incomplete optical overlap in the near range can also be somewhat overcome by scanning DWL systems that are able to combine multiple scan patterns. By adding low–level scanning strategies to higher elevation scan patterns, the vertical extent of the sampled wind profile can cover practically the entire ABL (Banta et al., 2006; Pichugina and Banta, 2010; Vakkari et al., 2015).

Instrument noise can play a role when measuring turbulence statistics if high-frequency variations are introduced into the signal (Tucker et al., 2009; Lenschow et al., 2000). Gravity waves and other larger-scale atmospheric motions can hamper the simple interpretation of velocity fluctuations as a proxy for turbulent motion. Methods are under development to diagnose and account for such situations (Banakh and Smalikho, 2016; Bonin et al., 2018). In general, it is crucial to assess the implications of noise filtering, sampling frequency, integration time, and measurement volume on turbulence observations (Bonin et al., 2017; Pichugina et al., 2008)

Precipitation can have a similar impact, since rapid variation in terminal fall velocities for different sizes of large precipitation particles, such as drizzle or rain drops and most ice particles, will manifest itself as vertical velocity fluctuations that look similar to turbulence. In other words, significant terminal fall velocity superimposed on the air motion of the measurement volume will impart biases if not accounted for. Methodologies using the associated variations in the signal backscattered from precipitation particles are being developed to identify such cases.

DWL can operate under all weather conditions at high temporal (<1 min) and vertical (<100 m) resolution. The resolution, spatial extent, and accuracy of the retrieved wind information depends on the instrument model and the scan strategy. A major advantage of DWL with scanning capabilities is that a series of different measurement setups can be alternated to gather optimised sampling strategies for several advanced data products simultaneously. This proves valuable not only for the detection of ABL heights but also for in-depth characterisation of ABL dynamics (Sect. 4).

2.2.4 Aerosol and gas profiling

Lidar systems are active remote sensing instruments that emit short and intense laser pulses which are then scattered by aerosol particles, droplets, and molecules. A fraction of this radiation is backscattered towards the instrument and collected by a telescope. A set of optical devices lead the radiation signal to the optical detectors, converting it into an electrical signal. The round trip time of each emitted laser pulse determines the distance between the lidar and altitude at which the radiation has been backscattered, allowing the generation of vertical profiles of backscattered signal. The backscattered lidar signal is proportional to the concentration and size of particle scatterers. Thus, the recorded signal increases with the amount of atmospheric scatterers in form of aerosol particles and cloud/rain droplets. Thick water clouds fully attenuate the lidar signal, so that the recorded backscatter reduces to noise at some depth inside the cloud. Noise levels further increase due to the background signal induced by solar radiation. Ground-based lidar systems available for the profiling of aerosols and gases differ greatly in laser power and wavelengths utilised. It can be generally differentiated between high-power lidar systems and the comparatively low-power automatic lidars and ceilometers (ALC).

High-power lidars include aerosol research lidars, Raman lidars, and DIAL. Aerosol research and Raman lidars widely use Nd:YAG lasers at tens Hz typical repetition rates, with extremely high pulse energy reaching of >1 J at the fundamental wavelength (1064 nm) and up to hundreds of mJ at the second (532 nm) and third (355 nm) harmonics. Depending on the laser repetition rate and pulse energy, temporal resolution ranges from seconds to minutes. Range resolution is defined by the speed of the data acquisition system ((e.g., a 100 ns laser pulse length has a 15 m folded scattering length, Weitkamp, 2005), with very high resolution (7.5 m or even higher) possible. **Raman lidar** systems transmit at one or multiple wavelengths and detect

https://doi.org/10.5194/amt-2022-14
Preprint. Discussion started: 21 April 2022

the Raman-shifted scattering by molecular excitation at other wavelengths, enabling the determination of the constituent of interest, e.g., water vapour mixing ratio (Wulfmeyer et al., 2010), the particle extinction coefficient Ansmann et al. (1992) and the temperature profile (Sect. 2.2.2) using the rotational Raman technique (Behrendt et al., 2015). **DIAL** transmit laser beams at two different wavelengths exploiting the differential attenuation (Lammert and Bösenberg, 2006) to derive vertical profiles of water vapour (Behrendt et al., 2007) or trace gases such as CO_2 (Gibert et al., 2008), CH_4 (Robinson et al., 2015), ozone (Banta et al., 1998), or NO_2 (Piters et al., 2012).

ALC are compact, simple lidars which operate at wavelengths mostly in the infrared or visible spectral region, e.g., 532 nm, 808 nm, ∼910 nm, 1064 nm are common wavelengths. ALC record the attenuated backscatter (Sect. 2.1) signal, which often needs to be absolutely calibrated during post-processing (Wiegner and Geiß, 2012; Hopkin et al., 2019). While most ALC are monochromatic, few models with multiple wavelength do exist and first sensors with depolarisation capabilities start to emerge. Typical ALC are the micro pulse lidars (MPL) and ceilometers, originally designed as cloud base height (CBH) recorders. CBH is the standard output variable for all ALC in addition to the attenuated backscatter profiles. Retrievals of ABL heights are also increasingly incorporated into the ALC firmware versions.

The most striking disadvantage of ALC compared to high-power lidars is the comparatively lower SNR. Given the latter not only depends on atmospheric composition but is largely determined by the laser power and optics of the lidar system (Heese et al., 2010), data from DIAL and Raman lidars are often able to capture more details of the atmosphere vertical structure and high-quality information can be obtained over a greater vertical extent. But also among ALC the SNR capabilities vary greatly (Caicedo et al., 2020; Kotthaus et al., 2016, 2020) due to the wide range models available from various manufacturers. ALC performance may be especially limited in pristine environments where aerosol load is low or at elevated heights above the sensor (e.g., deep ABL development). While data from high-power lidars and high-SNR ALC can usually be analyzed at the recorded temporal resolution, averaging was found to improve the SNR of low-SNR ALC (e.g., Markowicz et al., 2008; Stachlewska et al., 2012; Lee et al., 2019; Mues et al., 2017; Min et al., 2020; Caicedo et al., 2020; Tsaknakis et al., 2011). It should be noted that some instrument-related artifacts have been detected that may be associated with specific hardware or firmware versions (Kotthaus et al., 2016; Kotthaus and Grimmond, 2018a).

For all lidar systems, the incomplete optical overlap between the field of view of the receiver telescope and the emitted laser beam (Freudenthaler et al., 2018; Simeonov et al., 1999) can significantly increase the uncertainty in the lowest several hundred meters. The extent of the profile affected, varies with instrument design (Haeffelin et al., 2012; Caicedo et al., 2020). High-power lidars have a significant blind zone while ALC usually reach full optical overlap at lower levels, giving them an advantage in monitoring shallow ABL layers. Although most ALC manufacturers supply optical overlap correction functions (at times specific to the individual sensor) more complex correction models can be necessary to dynamically account for variations in the overlap function (e.g., dependent on the instrument internal temperature; Hervo et al., 2016; Geiß et al., 2017).

The most prominent limitation in the exploitation of Raman and research lidars is their limited temporal coverage as they are generally not operated continuously as Raman channels can usually only be exploited when the natural background light is low, i.e. at night. In addition, as consumables of high-power lidars are expensive, most operators of limit measurements to times when no low-level liquid-water clouds are present which would completely extinguish the lidar signal at very low altitude.

As ALC can be operated continuously, and autonomously under all weather conditions with very low maintenance, their data have a much greater temporal coverage than those collected by research lidars which often focus on specific periods of interest. Finally, the strength of ALC is their unprecedented spatial distribution (Sect. 2.3). Aerosol profile information obtained from lidar systems can be analysed using aerosol-based ABL height retrievals (Sect. 3.3).

https://doi.org/10.5194/amt-2022-14
Preprint. Discussion started: 21 April 2022

2.3 Profiling Sensor Networks

Profile data of the atmospheric boundary layer gain value when gathered by coordinated and harmonised measurement networks as these add information on variations in the horizontal spatial domain. High-quality ABL network data not only provide unprecedented details for process studies but also show great potential for the advancement of NWP via data assimilation (Illingworth et al., 2019; Martinet et al., 2020; Tangborn et al., 2021). While radiosonde stations have been organised in coordinated networks for decades, collaborative measurement networks of RWP, DWL, MWR and ALC are now also emerging (Figure 4). Mobile platforms equipped with multiple instruments can be a powerful addition during intensive observation periods (Wagner et al., 2019).

Worldwide there are ∼1300 **radiosonde** launch sites (Figure 4a, WMO, 2017), with 100-200 stations making observations once or twice per day. A subset of upper-air stations (∼170) comprises the global climate observing system (GCOS) upper-air Network (GUAN, WMO, 2014). The GUAN Monitoring Centre is hosted at the European Centre for Medium-range Weather Forecasts (ECMWF). Analysis of GUAN data is optimised by the U.S. National Oceanic and Atmospheric Administration (NOAA) National Climatic Data Center (NCDC). NOAA/NCDC archives all GUAN data and makes them available through the Integrated Global Radiosonde Archive (IGRA[4]). A subset of GUAN has been selected to establish the GCOS reference upper-air network (GRUAN, WMO, 2013), providing radiosonde data from reference-quality stations with traceable uncertainty estimates (Bodeker et al., 2016). Higher vertical resolution radiosonde data, but spatially and temporally more limited, are provided by the Stratospheric-tropospheric Processes And their Role in Climate data center (SPARC[5] through the U.S. High Vertical Resolution Radiosonde Data (HVRRD[6]).

Off-the-shelf commercial **MWR** and DWL are now robust instruments that can be deployed for unattended, continuous operations, providing atmospheric profile observations in nearly all-weather conditions. However, for both technologies, networking at national and international level is still in its infancy (Hirsikko et al., 2014; Thobois et al., 2018), meaning MWR and DWL data could be exploited more effectively in the future. The U.S. ARM program[7] runs a network of several MWR (Cadeddu et al., 2013) and also IRS, though still at a limited number of stations. A first attempt at MWR network operation in Europe was the LUAMI (Lindenberg Upper-Air Method Intercomparison) campaign funded by the German Weather Service (DWD) to demonstrate the capabilities of MWR profiler systems for use in operational meteorology. A test network of eight MWR profilers supplied quality-checked data in near real-time to a network hub (Güldner, 2013, and references therein). Several European COST[8] actions taking place over the last fifteen years have worked towards the establishment of an international network of MWR (MWRnet[9]). MWRnet is a bottom-up network of users, currently grouping more than 100 MWR of different types worldwide (Figure 4b), with 25 profilers located in Europe. MWRnet activities demonstrate the potential of MWR observations for data assimilation (Caumont et al., 2016) and the maturity of these sensors for network deployment

---

[4] https://www.ncdc.noaa.gov/data-access/weather-balloon/integrated-global-radiosonde-archive

[5] http://www.sparc-climate.org/

[6] http://www.sparc-climate.org/data-center/data-access/us-radiosonde/

[7] www.arm.gov/capabilities/instruments/mwrp

[8] Cooperation in Science and Technology; https://www.cost.eu/

[9] http://cetemps.aquila.infn.it/mwrnet/

https://doi.org/10.5194/amt-2022-14
Preprint. Discussion started: 21 April 2022

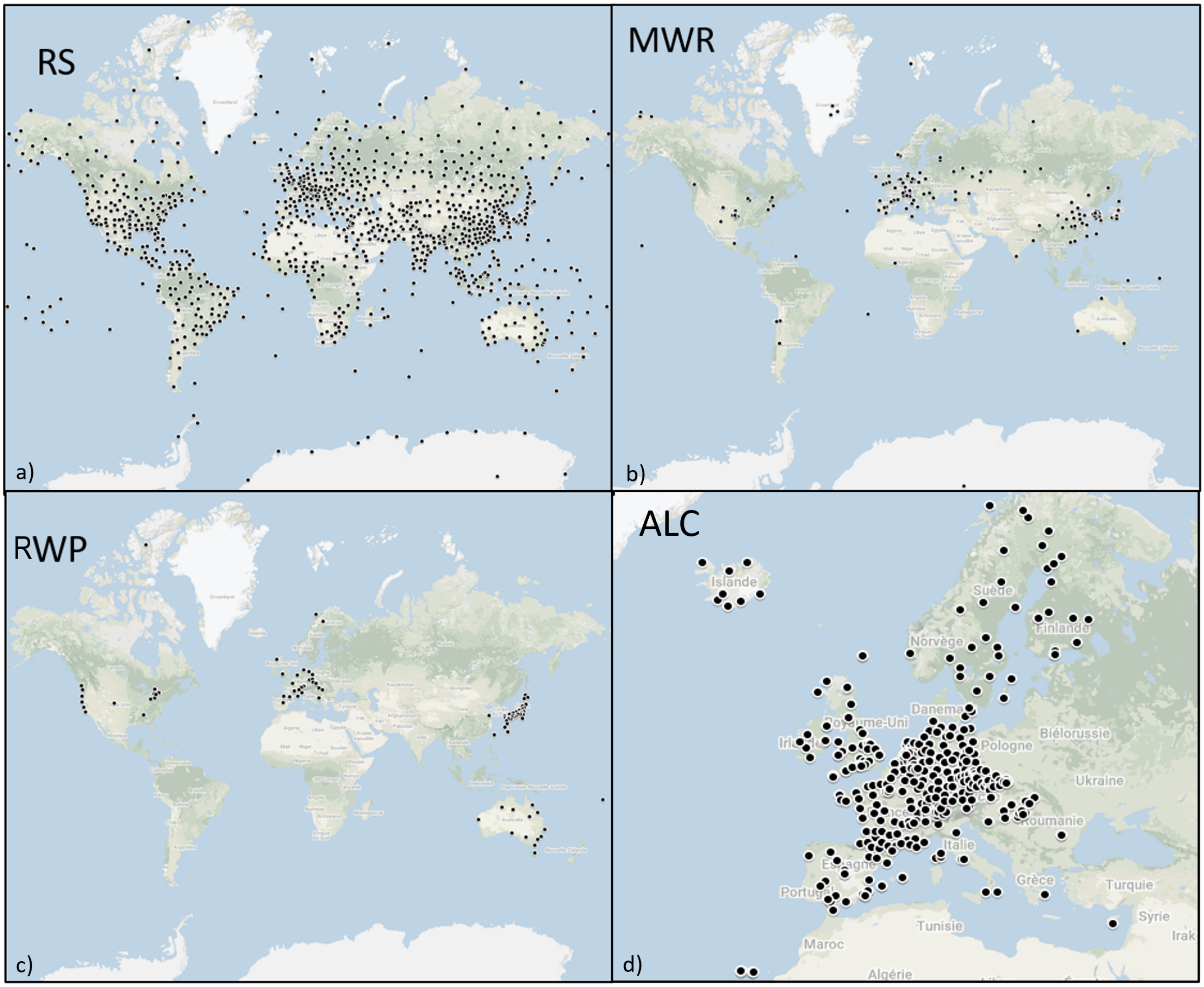

Figure 4. Operational networks of selected profile stations in December 2021: a) global distribution of radiosonde stations (RS) [WMO], b) global distribution of microwave radiometers (MWR) [MWRnet,MTP-5, RPG], c) global distribution of radar wind profilers (RWP) [JMA, NOAA, E-PROFILE], and d) European distribution of Automatic Lidar and Ceilometers (ALC) [E-PROFILE]. Backgroud map © Google Maps 2022.

(Illingworth et al., 2019). As a consequence, the European national meteorological services network (EUMETNET) accepted the business case for a European MWR network as part of the operational service E-PROFILE which will be implemented until 2023 (Rüfenacht et al., 2021).

The worldwide national **RWP** networks (Figure 4c) are operated in Australia (14 systems), China (128, Liu et al., 2020), Japan (33, JMA[10], Canada (7), United States (9, NOAA[11]), and in several European countries (32), covering various frequencies. EUMETNET E-PROFILE[12] coordinates the RWP network operations in Europe, Canada and Australia. However, many RWP are not yet integrated in such coordinated networks but are rather operated individually by national hydrological and meteorological services (NHMS), airports, private companies, or research institutions (Ruffieux, 2014).

In Europe, many of the **DWL** dedicated to meteorological applications are located at stations that also serve the Aerosol, Cloud and Trace gases Research Infrastructure (ACTRIS[13]) community. The US ARM program operates a network of several DWL alongside their MWR and cloud radars (Mather and Voyles, 2013). Operational DWL are incorporated in the urban meteorological observation system (UMS-Seoul) designed and installed in Seoul, South Korea (Park et al., 2017), the 3DREAMS network in Hong Kong, China (Yim, 2020), and are a major component of the New York State Mesonet (Thobois et al., 2018). There are now significant numbers of DWL deployed in commercial networks for wind energy applications mostly dedicated to observe winds at turbine level (around 50-150 m altitude) rather than the full extent of the ABL, and the data may be commercially sensitive.

ALC are the most widely used instruments in ground-based profile remote sensing networks. There are several network initiatives coordinating ALC measurements, such as the NASA-led Micro-Pulse Lidar Network (MPLNET[14]), the Photochemical Assessment Monitoring Stations (PAMS[15]) network of the U.S. Environmental Protection Agency (EPA), or the AD-Net in Asia (Shimizu et al., 2016). Currently, two ACTRIS thematic centers (Center for Aerosol Remote Sensing (CARS); Center for Cloud Remote Sensing (CCRES)) are developing services to enhance the quality of ALC measurements. And also the European research infrastructure Integrated Carbon Observing System (ICOS[16]) is increasingly operating ALCs to monitor the ABL height at their stations. E-PROFILE[17], part of the EUMETNET Composite Observing System (EUCOS), combines the majority of ALC networks established in Europe. In 2021, more than 370 units were transmitting data in near real-time (Figure 4).

DIAL and Raman lidars are mostly organised in research networks, such as ACTRIS/EARLINET[18], NDAAC[19], or PollyNet (Baars et al., 2016), providing observations of the full troposphere and even lower stratosphere. However, as these sensors are less autonomous compared to MWR, RWP, DWL, or ALC, spatial coverage tends to be lower for these networks.

---

[10] https://www.jma.go.jp/jma/en/Activities/windpro/windpro.html

[11] https://psl.noaa.gov/data/obs/datadisplay/

[12] https://e-profile.eu/

[13] https://www.actris.eu/

[14] https://mplnet.gsfc.nasa.gov/

[15] https://www.epa.gov/amtic/photochemical-assessment-monitoring-stations-pams#sites

[16] https://www.icos-cp.eu/

[17] https://www.eumetnet.eu/activities/observations-programme/current-activities/e-profile/

[18] https://www.earlinet.org

[19] https://www.ndsc.ncep.noaa.gov/

Several European COST actions have helped advancing ground-based profile remote sensing of the ABL and the development of layer height retrieval methods, including Action 710 (Harmonisation of the pre-processing of meteorological data for atmospheric dispersion models; Seibert et al., 2000), EG-CLIMET (European Ground-based observations of essential variables for CLImate and METeorology; Illingworth et al., 2015), and TOPROF (Towards Operational ground based PROFiling with ceilometers, Doppler lidars and microwave radiometers for improving weather forecasts; Illingworth et al., 2019). Following the progress made in this field over recent decades, the action PROBE[20] (PROfiling the atmospheric Boundary layer at European scale; Cimini et al., 2020, 2019-20234) now focuses on the harmonisation of operational procedures which is necessary to ensure also higher level products are comparable across Europe and even globally.

These EU COST actions are paramount for the exchange of knowledge and best practices between networks such as E-PROFILE, ACTRIS and ICOS. The networks not only collect and archive the observations but also aim to harmonise sensor settings and standardise file formats. In close collaboration with NHMS, academia and instrument manufacturers, standard operating procedures are being formulated and implemented, house-keeping data are closely monitored, detailed correction procedures are applied (e.g., Hervo et al., 2016) and advanced data products are developed, including the detection of ABL heights.

---

[20] http://www.probe-cost.eu/

https://doi.org/10.5194/amt-2022-14
Preprint. Discussion started: 21 April 2022

3 ABL height retrievals

Layer boundaries both within and at the top of the ABL (Sect. 1.1) constitute zones of transition between air of different characteristics. The various physical quantities (Sect. 2.1) derived from profile measurements (Sect. 2.2) each capture some aspects of the ABL development determining these layer heights (Figure 3). The most common methods developed to retrieve the ABL heights from profiles of temperature and humidity (Sect. 3.1), wind and turbulence (Sect. 3.2), or aerosol characteristics (Sect. 3.3), respectively, are outlined in this section.

Limitations and uncertainties are discussed and where possible linked to limitations of the sensors used for data collection. Two prominent effects reducing the capability of many active ground-based remote sensing instruments are a) a potential blind zone that reduces the capability of observing shallow layers in the near range and b) insufficient SNR in higher altitudes. Profilers with a certain blind zone (many aerosol and Doppler wind lidars) do not provide information in the first range rates near the sensor which means, when the signal is send upwards (e.g., DWL vertical stare or high elevation angles), the first reliable measurement level may be located above the $MBLH$ when layers are very shallow. In this case, the derived heights only provide an 'upper limit' of the true layer height. Similarly, observations obtained under low SNR conditions (e.g., due to low aerosol load) may not capture the full extent of the ABL (Liu and Liang, 2010) in which case derived layer heights should be considered a lower limit (Bonin et al., 2018; Krishnamurthy et al., 2021).

It is generally challenging to objectively quantify the performance of a method used for layer height detection, mainly because there is no absolute reference for ABL heights against which the derived product could be verified. Instead, evaluation is usually based on inter-comparisons, both between methods using the same quantity and between results obtained from different atmospheric variables. During interpretation it is hence key to consider that discrepancies not only reflect the errors of the respective height retrieval methods and the uncertainties in the atmospheric profiles analysed but may further be affected by a series of methodological aspects:

- a potential mismatch in the representation of the observed atmospheric quantity linked to data acquisition (e.g., profile vertical resolution, horizontal displacement of the sensor),
- potential difference in the signatures of atmospheric processes captured by the respective methods (e.g., when comparing thermodynamic layer estimates to aerosol-based layer estimates).
- all layer *heights* in reality relate to a transition *zone* between two atmospheric layers, so that the specific signature in the atmospheric profile associated with the respective layer height is relevant (e.g., is $CBLH$ located at the bottom, middle or top of EZ? Helmis et al., 2012).
- during times of pronounced temporal variations in layer heights (e.g., morning growth of CBL), temporal resolution and averaging can naturally affect the agreement between methods.

Due to the lack of a better alternative, thermodynamic layer heights (Sect. 3.1) derived from radiosonde profiles (Sect. 2.2.1) are most commonly used as a reference (Seibert et al., 2000). However, comparing balloon ascends and ground-based remote sensing data can be prone to some systematic discrepancies connected to horizontal and temporal variations in ABL dynamics.

- The horizontal drift of the balloon during the ascent means radiosondes may observe spatial variations in ABL dynamics that are not captured by the ground-based remote sensing instrument at a fixed location. This may impact the comparison especially where ABL dynamics respond to surface heterogeneities (e.g., Tang et al., 2016; Peng et al., 2017), but also the synoptic flow plays a role given radiosonde balloons are drawn into regions of convergence so that their profiles are more likely to trace convective activities (Schween et al., 2014).

- Spatial displacement between balloon ascends and the ground-based profile can be further altered if the remote sensing instrument is operating on a moving platform (e.g., ship-based observation; Tucker et al., 2009).

- At the EZ, convective plumes can cause variations of $ABLH$ at the order of several hundred metres ($\sim$150-250 m; Hennemuth and Lammert, 2006; Granados-Muñoz et al., 2012) within a few minutes. While some ground-based profiling sensors operate at very high resolution and can hence capture such temporal variations, the radiosondes only monitor the layer boundary at one given instance.

- The agreement between layer heights detected by methods based on different atmospheric quantities varies with atmospheric conditions (such as stability, cloud dynamics, etc.; 4.4). As these usually change through the course of a day, the timing of radiosonde ascents relative to the diurnal cycle of the ABL dynamics can affect the comparison statistics.

It should be noted that *standard sounding data*, i.e. radiosonde profiles reduced to significant pressure levels (Sect. 2.2.1), yield higher $ABLH$ than data at high vertical resolution which can introduce structural uncertainties of a few hundred meters in long-term statistics. Systematic performance errors of the radiosonde humidity sensors (Sect. 2.2.1) lead to reduced accuracy of humidity-based detection methods (Sect. 3.1) in the presence of clouds.

All these aspects should be considered when interpreting limitations and uncertainties of the various methods. In general, uncertainties in layer height detection vary with time of day and differ between the layer targeted. Uncertainty increases when multiple ABL sub-layers are present as layer boundaries not only have to be detected but a second, so-called *layer attribution* step is required. Particularly at times with significant temporal variation in ABL dynamics (e.g., formation of a low-level jet, advection of air masses, morning growth and evening decay of the CBL, formation of clouds or fog), multiple layer boundaries need to be interpreted with care.

3.1 Methods based on temperature and humidity

Detection methods for ABL heights based on temperature and/or humidity profiles rely on thermodynamic effects. They allow for the identification of daytime and nighttime layer heights, namely $CBLH$, $SBIH$, $SBLH$, and RLH (Sect. 1.1; Seibert et al., 2000; Seidel et al., 2010, 2012, and references therein). While some methods are directly applied to the profiles of air temperature, others utilise the potential temperature that considers atmospheric stability or the virtual potential temperature which accounts for atmospheric humidity effects in addition (Figure 3). Computation of θ (θ_v) requires atmospheric pressure (and humidity) which are at times obtained from external data sources (e.g., other sensors, reanalysis). Some methods directly explore profiles of relative humidity or specific humidity (Beyrich and Leps, 2012). Alternatively to air or potential temperature, the brightness temperature (Sect. 2.1) observed by radiometer profilers (Sect. 2.2.2), can be used as an input for layer height retrievals, as this physical quantity holds information on both temperature and humidity (similarly to the virtual potential temperature).

Temperature and humidity methods can be applied to profile data from in-situ measurements (Sect. 2.2.1), radiometers, DIAL or Raman lidars (Sect. 2.2.2) but are also very commonly implemented in numerical modelling when ABL heights are provided as a diagnostic variable determined from the model output (e.g., Cohen et al., 2015).

3.1.1 Methods

The two most commonly applied temperature-based approaches for the detection of $CBLH$ are the parcel method (Holzworth, 1964) and the bulk-Ridchardson method (Vogelezang and Holtslag, 1996). The parcel method defines $CBLH$ as the height to which an air parcel with ambient surface air temperature can rise adiabatically from the ground by convection and is obtained by following the dry adiabat from the surface up to its intersection with the temperature profile. The parcel method is only applicable in unstable atmospheric conditions. The bulk Richardson number Ri_b represents the ratio of turbulence induced by thermal buoyancy and wind shear, respectively. It can essentially be interpreted as an advanced parcel method that considers the shear contribution. Profiles of both temperature and horizontal wind velocity are required to calculate Ri_b. The bulk Richardson method can be applied to detect the $CBLH$ and indicates when the atmospheric stratification is stable but does not provide a layer height estimate in the latter case. These layer heights are detected as the heights where Ri_b exceeds a critical threshold. Typical thresholds for the bulk Richardson method are 0.10-0.40 (Sørensen et al., 1996) and 0.25-0.50 (Seibert et al., 2000) with the value 0.25 used to estimate $ABLH$ provided in ERA-Interim re-analysis data (von Engeln and Teixeira, 2013). The choice of the threshold value has a relatively modest impact on the layer detection accuracy (Seidel et al., 2012; Guo et al., 2016; Beyrich and Leps, 2012; Cimini et al., 2013). As the bulk Richardson method and the parcel method are identical if the threshold value is set to 0, the bulk Richardson method, by definition, gives a higher layer result than the parcel method. This increment was found to be about 20 m on average for the $CBLH$ (Collaud Coen et al., 2014). Given moisture lightens the air and allows it to convectively rise to greater altitudes, the parcel and the bulk-Richardson methods based on θ_v instead of θ (Sect. 2.1) result in slightly greater layer heights (3–8% Collaud Coen et al., 2014).

Both the parcel and bulk Richardson method highly depend on the accuracy of the ambient air temperature at the surface. A temperature excess corresponding to the strength of convective thermals can be added to θ_v at the surface under unstable conditions (Holtslag and Nieuwstadt, 1986; Seibert et al., 2000). This excess temperature is usually applied when the surface air temperature is measured at a height exceeding the standard 2 m, as in e.g., radiosoundings or NWP model data (Stohl et al., 2005).

In addition to the commonly used Parcel and bulk Richardson methods, several others thermodynamic methods are available to detect ABL heights, including:

1. $SBIH$ and $SBLH$ under stable conditions
    - As a clear indicator of a stable boundary layer, the height of the SBI is diagnosed from air temperature profiles (Bradley et al., 1993; Seidel et al., 2010).
    - At the transition between the SBL and the neutral residual layer, $SBLH$ is marked by a vertical gradient of θ equal to zero, that corresponds to the theoretical lapse rate (Collaud Coen et al., 2014) or equal to a critical lapse rate determined by the maximal variance of the gradient (Min et al., 2020).
    - Liu and Liang (2010) refine $SBLH$ detection by choosing the first height above ground that either shows a minimum in the potential temperature gradient or local maximum in horizontal wind speed if a LLJ is present. The method uses surface classification (land, ocean, ice) to determine critical thresholds. It should be noted that the accuracy of $SBLH$ (and to some extend $SBIH$) detection highly depends on the vertical resolution of the analysed temperature profile. In contrast to the parcel method or the Ri_b method, no vertical interpolation or smoothing of the profile data should be performed.
2. $CBLH$ under unstable conditions
    - The *Heffter method* determines $CBLH$ as the minimum height where the vertical gradient of θ exceeds 0.005 K m^{-1} while θ changes by more than 2 K across the inversion layer (L., 1980).
    - The minimum height where θ reaches a certain increment compared to its ABL minimum can mark the $CBLH$ (Nielsen-Gammon et al., 2008).
    - The maximum negative vertical gradient of refractivity (Sect. 2.1) or humidity was found to mark the $CBLH$ (Seidel et al., 2010).
    - Schmid and Niyogi (2012) improve the detection of $CBLH$ by allocating heights where a change in the vertical θ_v gradient coincides with a dew point temperature inversion.
3. $MBLH$ independent of atmospheric stability
    - The vanishing gradient in the air temperature profile marks the base of an elevated temperature inversion that serves as a cap to mixing below and can be considered the $MBLH$ (Seidel et al., 2010).

- Cimini et al. (2013) apply a multivariate statistical regression method trained with real observations to derive $MBLH$ directly from T_b. This method exploits all the information in the MWR observations and is independent of uncorrelated retrieval errors in the temperature and humidity profiles (Sect. 2.2.2) as both systematic and random errors are inherently accounted for.
- To ensure continuous layer detection, different temperature-based methods can be combined depending on atmospheric stability as the most applicable method may vary during the course of the day and between land cover types. Maybe the most common method synergy is the combination of the parcel method ($CBLH$) and the $SBIH$ at night.
- Some disagreement between temperature- and humidity-based methods stems from the presence of clouds, which create a complex vertical ABL structure (Sect. 4.6). While humidity-based methods tend to respond to the layer boundary at the cloud top (large negative humidity gradient), the maximum gradient of θ usually occurs in the middle of the EZ above the cloud. To overcome this issue, $ABLH$ can be assigned to the level where all of the above variables exhibit pronounced variations simultaneously, rather than looking for the strongest change in one specific profile variable.

3.1.2 Capabilities and limitations

Long-term, multi-site comparisons reveal some systematic differences between the various temperature- and humidity-based methods (e.g., Seidel et al., 2010; Beyrich and Leps, 2012). The Heffter method often overestimates $MBLH$ and the definition of thresholds was found challenging (see discussion in Caicedo et al., 2020, and references therein). Sinclair et al. (2021) find agreement and sign of systematic biases depend on atmospheric stability. The T_b regression method (Cimini et al., 2013) provides height estimates that are mostly consistent with the bulk-Richardson approach. Methods based on finding extreme vertical gradients are in better agreement with each other than those based on locating elevated temperature inversions (Seidel et al., 2010).

It is generally concluded that uncertainties in layer detection are closely linked to uncertainties in the atmospheric profiles analysed (e.g., errors in surface wind speed, vertical interpolation and vertical resolution; Seidel et al., 2012). Given such errors are much more pronounced (10-80 %) for low layer heights (<1-2 km), relative uncertainties of the layer detection can be large (>50 %) for shallow layers but usually remain below 20 % for layer heights >1 km (Seidel et al., 2012; Aryee et al., 2020; Guo et al., 2016). Methods agree better when applied to radiosonde profiles at midday compared to midnight conditions (Beyrich and Leps, 2012). This further highlights that $CBLH$ layer boundary is better defined while detection of $SBLH$ is more ambiguous.

As the parcel method is more likely to capture shallow layer heights, Seidel et al. (2010) conclude that diurnal and seasonal variations based on this method generally tend to have a greater amplitude and can be considered more consistent than those derived from other approaches. This is in agreement with the MWR analysis of Collaud Coen et al. (2014) who found the parcel method to be more robust (compared to the bulk Richardson method or the analysis of surface-based temperature inversions or humidity gradients) and hence better suited for automatic real-time detection of the $MBLH$, as it provides good results under a wide range of meteorological conditions. The parcel method is sensitive to surface-level data (Sect. 3.1.1). For example, a change in surface temperature by $\pm$0.5 K leads to uncertainties at the order of $\pm$50-150 m for the maximum $CBLH$ in the early afternoon (Collaud Coen et al., 2014) at a mid-latitude continental site. Careful quality control of the measurements is hence required to ensure physically reasonable coupling of the surface air temperature value to the first values of the temperature profile (Beyrich and Leps, 2012). Horizontal and/or vertical separation between the site of the surface measurements and the radiosonde launch site can cause artificially large vertical gradients in the combined temperature profile which may result in significant average differences in the derived $ABLH$ of up to several hundred metres (Seidel et al., 2010). In such cases, it is preferable to initialise the parcel method with the first reported upper air level instead of surface observations.

The presence of clouds increases uncertainty in $CBLH$ retrievals for all methods (Sect. 4.6), so that temperature-based methods applied to radiosondes and MWR profile data show better agreement during clear-sky days (Cimini et al., 2013). When the parcel method is applied to temperature profile data obtained from radiosondes and MWR, the latter tend to significantly under-estimate the $MBLH$ (Cimini et al., 2013). Up to now, no quantitative, comparison analysis has been performed regarding $MBLH$ estimates from different MWR types, although there have been field campaigns where multiple commercial MWR were operated side-by-side, such as the Joint CALibration experiment (JCAL, Pospichal et al., 2016) or the recent Field Experiment on submesoscale spatio-temporal variability in Lindenberg (FESSTVaL[21]).

The method using T_b regression analysis (Cimini et al., 2013) relies on "independent training data". Given there is no absolute reference when it comes to ABL heights, the choice of training data and potential systematic differences in the physical representation of ABL dynamics by the observed quantity analysed (Sect. 1.1) and the respective detection approach (Sect. 4) may affect the performance of this method. Still, even when trained with aerosol-derived layer estimates (Sect. 3.3), the T_b regression method shows better agreement with layer estimates from the bulk-Richardson method applied to radiosonde profiles compared to the parcel method and θ_v-gradient method applied directly to the MWR temperature and humidity data.

---

[21] https://fesstval.de/

3.2 Methods based on wind or turbulence

Methods exploiting wind profile observations to detect ABL heights can generally be grouped into those using components of the mean wind and those based on turbulence indicators. The objective of these methods is to identify the height of the turbulent layer connected to the surface. The mixing is either caused by buoyancy-driven turbulence (in case of the CBL), or shear-driven turbulence (in case of the SBL), or a combination of the two. Intermittant turbulence in the residual layer can affect the performance of layer detection algorithms (Pichugina and Banta, 2010) but wind and turbulence methods are usually not applied to detect RLH.

3.2.1 Methods

Using mean wind profiles (Figure 3), $SBLH$ can be identified as the height of a local maximum in horizontal wind speed or a local minimum in vertical wind speed or wind shear, respectively (Balsley et al., 2006; Banta et al., 2006; Pichugina and Banta, 2010; Lemone et al., 2014). Johansson and Bergström (2005) find significant changes in the mean ascent rate of radiosonde balloons indicate the transition from turbulent to non-turbulent regimes, whereby exploiting a mean quantity to diagnose turbulence indicators indirectly (Lemone et al., 2014). Due to advances in high-resolution ground-based profiling, direct measures of atmospheric turbulence can be determined quantitatively with increasing accuracy (Sect. 2.2.3).

Turbulence can be diagnosed from the refractive index (Sect. 2.1) observed by sodar and RWP (Sect. 2.2.3). The peak in the vertical profile of the refractive index caused by small-scale buoyancy fluctuations across the entrainment zone has been found to coincide with the $MBLH$ (White, 1993; Angevine et al., 1994; Wilczak et al., 1997). RLH can also be detected by analyzing profiles of C_n^2, but only for specific (mostly cloud-free) weather conditions. $ABLH$ is diagnosed from space-borne GNSS-RO observations as the strongest negative gradient in refractivity (Ao et al., 2012; Chan and Wood, 2013), that is associated with the strong moisture and temperature gradients usually present at the top of the ABL (Xie et al., 2012).

Estimates of atmospheric turbulence can also be obtained from temporal and/or spatial fluctuations in high-resolution wind profiling data. The most commonly exploited turbulence variables derived from high-frequency wind components are the variance of vertical velocity, variance in horizontal velocity, turbulent kinetic energy and the eddy dissipation rate (Sect. 2.1). To ensure layer detection relies on the measurement of turbulence intensity, it is important to remove non-turbulent fluctuations from the wind field components (Bonin et al., 2018). Applying a high-pass filter was found to be a simple but effective means to sufficiently reduce the influence of sub-mesoscale motions, drainage flows, and low atmospheric waves (Bonin et al., 2017, 2018), with frequencies on the order of minutes to tens of minutes (Finnigan et al., 1984). Berg et al. (2017) chose to detect layer heights based on the normalised vertical velocity variance to reduce the impact of coherent vertical motions above the ABL.

During convective atmospheric conditions, the vertical velocity variance from vertically pointing profile observations is the most direct measure of the instantaneous mixing within the CBL. The $CBLH$ is commonly assigned to the height above ground where the vertical velocity variance falls below a set threshold (Figure 3), with both absolute (0.04-0.16 $\mathrm{m}^2\ \mathrm{s}^{-2}$; Tucker et al., 2009; de Arruda Moreira et al., 2018; Barlow et al., 2011; Huang et al., 2017; Vakkari et al., 2015) and relative values (e.g., 10 % of profile maximum, Barlow et al., 2011) implemented successfully. Given the gradual decay of turbulence in the afternoon and evening CBL, Schween et al. (2014) find $CBLH$ detection to be particularly sensitive to the threshold value during these periods. The choice of threshold value can depend on the ABL structure (Tucker et al., 2009; Huang et al., 2017) and the scanning strategy-dependent noise levels (Bonin et al., 2018). When shear-driven turbulence dominates, horizontal velocity variance becomes a better indicator for the layer boundaries. The vertical profile of horizontal velocity variance depends on atmospheric stability, with a near-surface peak under slightly stable conditions, a rather constant vertical distribution under medium stable conditions, and a maximum aloft near the core of the LLJ under strongly stable conditions (Banta et al., 2006). Tucker et al. (2009) use the same threshold values as for the vertical velocity variance to determine shallow layer heights from horizontal velocity variance.

Turbulent kinetic energy or eddy dissipation rate are other quantitative measures of turbulence useful for layer detection. Lemone et al. (2014) find a relative value of 5% of the profile maximum TKE most suitable for the detection of $SBLH$ while LeMone et al. (2013) apply fixed values (0.101 and 0.200 $\mathrm{m^2\ s^{-2}}$) to determine $CBLH$ from model data. Vakkari et al. (2015) assign $CBLH$ to the height where the eddy dissipation rate falls below $10^{-4}\ \mathrm{m^2\ s^{-3}}$ while Frehlich et al. (2006) examine the strongest negative gradient of this quantity. For specific scan patterns, the variance of radial velocity (i.e. the native variable obtained form Doppler wind lidar measurements) is directly related to TKE (Sect. 2.2.3) and is hence also exploited for layer detection. Pichugina and Banta (2010) determine the $SBLH$ as the height of the first significant local minimum in the vertical profile of the radial velocity variance.

Under well-mixed, convective conditions, i.e. when $CBLH$ coincides with $ABLH$, turbulence-based detection methods can be supported by applying SNR requirements (Moreira et al., 2015; Pearson et al., 2010; Singh et al., 2016). Lothon et al. (2006) evaluate the total velocity variance from DWL observations for layer detection, which inherently includes the SNR information as the recorded signal responds to both atmospheric variations and instrument-related noise (Tucker et al., 2009). Some methods assign $CBLH$ to a local peak in RWP SNR (Liu et al., 2019a; Collaud Coen et al., 2014).

To cover the full range of $ABLH$ at a given measurement location, wind measurements from multiple data sources can be combined (e.g., Doppler sodar and RWP; Beyrich, 1997; Angevine et al., 2003). The great advantage of scanning DWL systems is that a series of wind and turbulence variables can be obtained within a rather short time interval by a single sensor (Sect. 2.2.3). For example, vertical stare measurements can be alternated with range-height indicator (RHI) scans (Tucker et al., 2009) to capture convection or plan position indicator (PPI) scans at low elevation angles (Vakkari et al., 2015) to capture shallow layers. To facilitate the composition of layer information from various atmospheric variables (mean wind fields, different turbulence indicators, SNR), fuzzy logic algorithms (Bianco and Wilczak, 2002; Bianco et al., 2008; Allabakash et al., 2017) or random forest machine learning (Krishnamurthy et al., 2021) are increasingly implemented. Recent advanced approaches (Bonin et al., 2018; Krishnamurthy et al., 2021) combine a diverse combination of atmospheric variables which enables reliable layer detection under nearly all atmospheric conditions. To enhance agreement with aerosol-derived layer heights (Sect. 3.3), Bonin et al. (2018) give less weight to the vertical velocity variance during layer height retrieval whereby moving the focus towards those indicators that portray the resulting 'mixed conditions' instead of the mixing process itself. Where the ABL

https://doi.org/10.5194/amt-2022-14
Preprint. Discussion started: 21 April 2022

responds to significant surface heterogeneities (Banks et al., 2015; Haid et al., 2020; Vakkari et al., 2015), site-specific design of DWL scanning strategies is recommended to best capture the local ABL spatial and temporal variability.

3.2.2 Capabilities and limitations

The altitude range of the atmospheric profile captured by the measurements and the accuracy of wind and turbulence data from ground-based remote sensing systems depends on instrument capabilities and measurement setup (Sect. 2.2.3). The ability to detect shallow layers generally depends on how large the blind zone of the sensor is, while observing the full depth of deeper convective conditions is dependent on SNR. Turbulence-based $MBLH$ estimation is particularly applicable in daytime convective conditions (Bianco et al., 2008; Collaud Coen et al., 2014). Decaying turbulence in the residual layer can be a source of added uncertainty (Lemone et al., 2014).

Rainfall can be a significant source of uncertainty for automatic layer detection from profiles of wind and turbulence. It is possible to diagnose from the vertical velocity profile based on the terminal fall speed of rain drops (e.g., using column averaged vertical velocity $< -1\ \mathrm{m\,s^{-1}}$, Bonin et al., 2018), but such filters will not detect precipitation conditions with lower fall speeds (such as drizzle or snow) and can miss precipitation that evaporates before reaching the surface (virga).

https://doi.org/10.5194/amt-2022-14
Preprint. Discussion started: 21 April 2022

3.3 Methods based on attenuated backscatter

Given the distribution of aerosol particles and moisture is in parts a result of mixing processes, attenuated backscatter profiles (Sect. 2.1) represent the recent history of ABL dynamics. Layer boundaries can be detected if aerosol properties differ between the atmospheric layers examined. The most pronounced layer edge is usually the $ABLH$ because aerosol concentrations and humidity tend to be significantly higher in the ABL than in the FT. But also within the ABL, mixing dynamics can lead to contrasting aerosol properties between different layers (Figure 3). During night and early morning, the lowest layer is considered the $MBLH$ ($SBLH$ under stable conditions) while the layer above defines RLH (Sect. 1.1). During unstable daytime conditions, the aerosol-based $MBLH$ forms in response to recent CBL mixing processes. Vertical and temporal changes recorded at high resolution allow for EZ characteristics to be examined. Decoupled, elevated aerosol layers above the ABL can be identified if they possess distinct aerosol characteristics. Lidars that capture depolarization information (Sect. 2.2.4) can provide additional insights that allow for boundary layer aerosols to be distinguished from lofted layers (e.g., Bravo-Aranda et al., 2017).

The physical quantity of attenuated backscatter is most commonly observed by ALC or aerosol research lidars (Sect. 2.2.4) but can also be derived from DWL (Sect. 2.2.3). As the majority of layer detection algorithms does not rely on absolute values in attenuated backscatter but rather assess relative variations of this quantity in time and height, the range-corrected signal is often used as an alternative input. SNR (or CNR) highly depends on the atmospheric aerosol load so that aerosol-based methods have also been applied to these noise profile data directly (Compton et al., 2013). While the discussion here focuses on ground-based profilers, it should be noted that aerosol-based techniques can also be used for the analysis of airborne lidar profiles (e.g., Scarino et al., 2014), satellite data (CALIOP, Zhang et al., 2016), or output from numerical simulations.

3.3.1 Methods

Aerosol-based retrievals of ABL heights detect layer boundaries based on regions of significant vertical (and at times temporal) change in attenuated backscatter. Where multiple layers are present within the ABL, the role of the respective layers needs to be examined carefully. Hence, two steps are required to determine the ABL heights from aerosol backscatter observations: (1) *detection of layer boundaries* within and at the top of the ABL, and (2) *layer attribution* to distinguish between simultaneous layers (e.g., $MBLH$ and RLH). Methods that predominantly address the task of layer detection are here considered *first-generation* aerosol-based retrievals, while those with a special focus on the more challenging aspect of layer attribution are grouped into *second-generation* aerosol-based retrievals.

To detect heights (or regions) of potential layer boundaries from attenuated backscatter profiles, a range of indicators has proven useful (see reviews by Emeis et al., 2008; Dang et al., 2019). These include negative vertical gradients and inflection points (e.g., Sicard et al., 2006; Emeis et al., 2008; Münkel, 2007; Schäfer et al., 2004; Lee et al., 2019), 2D-edge detection (e.g., Canny, 1986; Parikh and Parikh, 2002; Haeffelin et al., 2012), wavelet covariance transform (WCT; e.g., Cohn and Angevine, 2000; Morille et al., 2007; Baars et al., 2008; de Haij et al., 2006; Gan et al., 2010; Granados-Muñoz et al., 2012; Lewis et al., 2013; Caicedo et al., 2020), the cubic root gradient which takes into account the influence of gravity waves (Yang et al., 2017), and spatio-temporal variance (e.g., Menut et al., 1999; Martucci et al., 2007; Lammert and Bösenberg, 2006; Piironen and Eloranta, 1995; Hooper and Eloranta, 1986). For example, $ABLH$ is derived from CALIPSO satellite observations as the maximum in vertical and horizontal variance (Jordan et al., 2010).

Many layer detection methods show varying reliability at different stages of the diurnal ABL evolution. $ABLH$ is usually marked by the strongest negative gradient in attenuated backscatter and the mixing between moist ABL air and dry FT air across the EZ results in an area of strong spatio-temporal variance (e.g., Menut et al., 1999). But also entrainment of RL air into the CBL during morning growth can cause distinct variance signatures (e.g., Lammert and Bösenberg, 2006). While some methods (such as the wavelet approach) are less affected by noise, the simple method of vertical gradient detection can be advantageous in capturing layers at low ranges (Di Giuseppe et al., 2012).

Several approaches have been developed to accomplish the second task of layer attribution. First-generation retrieval methods apply attribution criteria either on the respective indicator (e.g., strongest negative vertical gradient) and/or simply based on height (e.g., first significant negative gradient above ground) to assign the layer of interest. Second-generation retrieval algorithms again can broadly be grouped into the following categories:

- Methods based on general layer characteristics: These methods group observations along the observed profile into categories. To differentiate between the ABL with high aerosol load and the FT with low aerosol signal, an idealised profile can be fit to the observations (e.g., Steyn et al., 1999; Eresmaa et al., 2006, 2012; Li et al., 2017; Peng et al., 2017). Further do recent artificial intelligence (AI) approaches analyse the profile across the whole layer, incl. extended Kalman filters (Lange et al., 2013; de Arruda Moreira et al., 2018; Kokkalis et al., 2020), *K-means* cluster analysis applied to either the attenuated backscatter profile (KABL; Toledo et al., 2014; Rieutord et al., 2021; Min et al., 2020) or layer candidates derived from first-generation methods (ISABL; Min et al., 2020), or a supervised *AdaBoost* algorithm (ADABL; Rieutord et al., 2021).

- Combination of identification techniques: Given that the various layer-detection techniques can be sensitive to slightly different layer boundaries, a combination of indicators can help to distinguish between layers. For example, Martucci et al. (2010a) combine the height of maximum negative gradient and height of maximum variance to detect $MBLH$ both during day and night together with lofted, decoupled aerosol layers. STRAT-2D (Morille et al., 2007; Haeffelin et al., 2012) uses the variance field to determine which wavelet-detected layer boundary is likely associated with $MBLH$ by analysing the location of the EZ. pathfinderTURB (Poltera et al., 2017) and STRATfinder (using advantages of STRAT+ and pathfinderTURB; Kotthaus et al., 2020) combine gradient and variance field diagnostics before tracing $MBLH$. COBOLT (Geiß et al., 2017) uses a combination of gradients, variance statistics and WCT, varying with solar angle to identify the $MBLH$. The profile-fit approach is combined with WCT by Sawyer and Li (2013) and with the negative gradient detection in the proprietary Vaisala BLview software (Münkel, 2016), respectively. It should be noted that the BLview algorithm provides several layer candidates so that some post-processing is required to select the appropriate $MBLH$. This has been achieved using, e.g., the provided quality flags (Geiß et al., 2017), gradient thresholds (Haman et al., 2012), manual screening (Caicedo et al., 2017), or a combination of time-tracking and height criteria (Mues et al.,

https://doi.org/10.5194/amt-2022-14
Preprint. Discussion started: 21 April 2022

2017). Applying Gradient Boosted Regression Trees, (de Arruda Moreira et al., 2022) use a first estimation of the $ABLH$ derived from the gradient method to a ceilometer signal and several meteorological variables to retrieve ABLH values comparable to those derived from a microwave radiometer, discriminating between $CBLH$ and $SBLH$.

- A priori assumptions based on ancillary observations: Where climatology statistics are available from independent measurements (e.g., radiosondes) limits can be prescribed that may vary by season. For example, in pathfinderTURB and STRATfinder absolute limits for $MBLH$ and morning transition growth rate are specified by the user. Some studies set time-specific coefficients (morning, afternoon, and night, respectively) for the WCT Gan et al. (2011); Caicedo et al. (2020). STRAT+ (based on STRAT-2D; Pal et al., 2013), uses radiosonde profiles and turbulent surface sensible heat flux measurements to derive stability information to aid interpretation of the variance field.

- A priori assumptions from model results: Simple models describing general ABL dynamics or output from NWP models representing varying synoptic conditions have been used to guide layer attribution. For example, Di Giuseppe et al. (2012) use a bulk model (Tennekes and Tennekes, 1973) based on surface sensible heat flux data to define times of morning and evening transition.

- Temporal layer tracking: Temporal consistency is a powerful criterion for layer attribution (Angelini et al., 2009) as it reduces physically unreasonable height fluctuations and growth rates. For example, the temporal-height-tracking method (THT, Martucci et al., 2010a) uses the $MBLH$ estimate at a previous time step to define the search window for the subsequent detection; a similar approach is implemented in COBOLT (Geiß, 2016) and by Wang et al. (2012) or Caicedo et al. (2020). The MIPA algorithm (Vivone et al., 2021) uses morphological image processing techniques to improve temporal consistency of the detected $MBLH$. A recent family of algorithms (pathfinder, pathfinderTURB, STRATfinder) apply a graph theory approach to trace the path of $MBLH$ through the day. In CABAM (Kotthaus and Grimmond, 2018a), points of significant negative gradients are connected to layers which are then traced through the day following growth and decay criteria in a dynamic decision tree. The extended Kalman filter uses information from past profile analysis to inform $ABLH$ detection, which generally improves temporal consistency but can also lead to errors when air with different aerosol load is advected (Kokkalis et al., 2020). Also the supervised ADABL algorithm (Rieutord et al., 2021) considers temporal consistency.

- Additional lidar profiles: Some research lidars and novel ALC (Sect. 2.2.4) provide additional profile information other than the attenuated backscatter that can be exploited to differentiate layer characteristics. The POLARIS algorithm analyses the depolarisation ratio in connection with the WCT approach (Bravo-Aranda et al., 2017). The MDS method (Liu et al., 2018) determines $ABLH$ by adding information on the particle size by calculating the degree of difference in aerosol characteristics between observations from two adjacent lidar range gates as a combination of aerosol backscatter and the color ratio (Sect. 2.1).

While most of these retrieval algorithms output one layer height (usually either $MBLH$ or $ABLH$), simultaneous identification of several layers is possible provided the layer attribution step does account for it (Kotthaus et al., 2020; Milroy et al., 2012; Caicedo et al., 2020; Toledo et al., 2017). Elevated aerosol layers can be traced in addition to ABL heights. For example, Poltera et al. (2017) detect a continuous aerosol layer above the ABL using pathfinerTURB while Pandolfi et al. (2013) track a decoupled aerosol layer above the ABL at a coastal site and Gan et al. (2010) derive RLH and elevated aerosol layers using the WCT approach.

In the absence of clouds, aerosol-derived $ABLH$ is usually located somewhere in the centre of the EZ, where vertical negative gradients and spatio-temporal variance are strongest due to the exchange of aerosols and moisture between the ABL and FT (Menut et al., 1999). Where observations at very high temporal resolution in the order of minutes are available and SNR is sufficient, temporal variations in $ABLH$ permit the estimation of EZ thickness (Cohn and Angevine, 2000) and entrainment velocities (Träumner et al., 2011). Martucci et al. (2010a) performed spectral analysis on high-resolution $ABLH$ observations to characterize entrainment processes under different atmospheric stability conditions. Alternatively, the transition zone concept, based on the difference between high attenuated backscatter values in the ABL and low values in the FT (Steyn et al., 1999) can be used to determine the EZ thickness. Statistical concepts capturing temporal, spatial and small-scale turbulence variations can differ significantly from the transition zone estimates given the latter is mostly limited to small-scale turbulence effects (Träumner et al., 2011).

3.3.2 Capabilities and limitations

Both the detection and the attribution step of aerosol-based layer retrievals highly depend on the quality of the attenuated backscatter profiles analyzed (de Haij et al., 2006; Milroy et al., 2012). An important variable describing the information content of a measurement at a certain time and range is the SNR (Sect. 2.1). Any combination of high instrument-related noise, low aerosol (and moisture) load, or very deep convection reduces the SNR which can lead to both under- and over-estimation of peak $ABLH$ (Kotthaus et al., 2020). Applying an SNR filter can improve layer detection (Poltera et al., 2017; Min et al., 2020), however, care must be taken in pristine environments (Boy et al., 2019), where atmospheric scatterers are scarce and the recorded signal may not necessarily exceed instrument and background noise significantly. While SNR-limitations mostly lead to uncertainties in the detection of layer boundaries at elevated heights above ground, the detection of shallow layers (nocturnal $MBLH$ and $SBLH$) can be affected by the incomplete optical overlap and near-range artefacts (Schween et al., 2014; Kotthaus et al., 2020; Caicedo et al., 2020). $MBLH$ and $ABLH$ retrievals based on attenuated backscatter have seen significant improvements due to recent advances in ALC measurement technology (Illingworth et al., 2019; Cimini et al., 2020) and detailed correction procedures (Hervo et al., 2016; Kotthaus et al., 2016) as both improve data quality and availability.

In addition to instrument-related uncertainties, discrepancies in layer results arise from the choice of retrieval algorithm. Haeffelin et al. (2012) compared five $MBLH$ detection techniques applied to observations from three different ALC at two contrasting measurement sites. While layer detection methods (first derivative, WCT, and two-dimensional derivative) often agree, the greatest uncertainty in final products was associated with the step of layer attribution, even when considering simple categories only. Second-generation algorithms (Sect. 3.3.1) hence put a special focus on the interpretation of the ABL sublayers. Comparing different second-generation methods, it appears that those including criteria on temporal consistency of layer estimates tend to perform slightly better (de Bruine et al., 2017; Knepp et al., 2017).

https://doi.org/10.5194/amt-2022-14
Preprint. Discussion started: 21 April 2022

Agreement between retrieval methods varies with the complexity of the ABL. Provided sufficient SNR, results from different methods and sensors tend to agree best in the afternoon during peak convective activity (Milroy et al., 2012) when the CBL extends over the whole ABL leaving essentially no sublayers to confuse the algorithms (Toledo et al., 2017). Layer attribution is challenged when several aerosol layers are present simultaneously, such as during night and early morning. If MBL and RL aerosols have similar characteristics, the $MBLH$ may not be characterised by a particularly strong gradient (Granados-Muñoz et al., 2012). Highest uncertainty generally occurs during the evening transition (Geiß et al., 2017) when new aerosol gradients start to form gradually and decaying turbulence may not be traced successfully by backscatter variance methods in case of homogeneous aerosol distributions (Poltera et al., 2017). In addition to ABL-internal sublayers, elevated aerosol layers advected over the ABL add complexity. Any aerosol-based method is challenged when temporal variations of gradients (or variances) are dominated by advection of aerosols (e.g., due to strong sea breezes or dust transport; Tang et al., 2016; Bravo-Aranda et al., 2017; de Arruda Moreira et al., 2020; Diémoz et al., 2019; Caicedo et al., 2019). Advances in measurement technology (such as depolarisation information becoming increasingly available; Sect. 2.2.4) and continued algorithm development (including AI methodologies; Rieutord et al., 2021) are expected to further improve layer attribution efforts.

The lidar signal is strongly attenuated by liquid clouds, so that the signal is often completely extinguished at about 300 m above cloud base (O'Connor et al., 2004). As a consequence, the profile of attenuated backscatter yields little information above the altitude of such thick water clouds. Where clouds form within the ABL, aerosol-derived layer heights can severely underestimate $CBLH$ (Hennemuth and Lammert, 2006). Advanced detection algorithms hence increasingly take into account the presence of boundary layer clouds (Poltera et al., 2017; Caicedo et al., 2020). Where the cloud base height variable provided by the ALC is used, it should be noted that this product can show systematic differences between internal algorithms from various manufacturers (Martucci et al., 2010b; Pattantyús-Ábrahám et al., 2017) and even between models from the same brand (Liu et al., 2015b). Most methods struggle with reliable layer detection and attribution during precipitation or the passage of synoptic fronts (de Bruine et al., 2017; Yang et al., 2017).

Some studies assign a quality flag to the derived layer heights based on the magnitude of the attenuated backscatter vertical gradient (e.g., de Haij et al., 2006; Ketterer et al., 2014). For $ABLH$, such indicators can be suitable given the strong contrasts in aerosol content between the ABL and the FT. However, the strength of the vertical gradient does not necessarily reflect the uncertainty in $MBLH$ detection at night or during morning growth as the contrast between the layer coupled to the surface and the RL is often weaker than to the FT. Careful quality control during post-processing (e.g., based on physically reasonable temporal variations in layer heights) can help focus inter-comparison or evaluation efforts (Kotthaus et al., 2020; Caicedo et al., 2020).

Aerosol-based retrievals for ABL heights are most commonly evaluated against thermodynamic retrievals (Sect. 3.1) applied to radiosonde profile data (Sect. 2.2.1). When comparing aerosol-derived layers to thermodynamic results, the conceptual differences between the two approaches should be taken into account during interpretation (Hennemuth and Lammert, 2006) regarding the physical processes that are being assessed (Sect. 1.1). Naturally, comparison statistics vary with the retrieval method applied on the radiosonde data (Haman et al., 2012). Compared to thermodynamic estimates, aerosol-derived $CBLH$ can have a negative bias (e.g., de Haij et al., 2006; Bravo-Aranda et al., 2017; de Bruine et al., 2017; Liu and Liang, 2010) as the atmospheric quantities of temperature and aerosol show different EZ characteristics (see discussion in Sect. 4.2). Best agreement between the temperature- and aerosol-based layer height detection is again found in the early afternoon, when the CBL extends over the whole ABL (de Bruine et al., 2017). Given the impact of advection on ABL complexity, agreement between the different approaches can vary with synoptic conditions or local circulations induced by surface cover heterogeneities (Pandolfi et al., 2013; Hennemuth and Lammert, 2006). Liu et al. (2018) find agreement between several aerosol-based $ABLH$ results and the bulk-Richardson method applied to daytime radiosonde profiles clearly improves with increasing atmospheric instability.

At night, thermodynamic detection of the height of the CI from radiosondes or AMDAR profiles (Sect. 2.2.1) were found to coincide well with aerosol-derived RLH (Martucci et al., 2007; Kotthaus et al., 2020; Milroy et al., 2012). The few studies showing direct $SBLH$ comparisons between aerosol-derived and thermodynamic results generally suggest a good agreement between the layer estimates, with small biases reported in either direction (Pal et al., 2013; Haman et al., 2012; Tang et al., 2016). Still, substantial systematic biases may occur, with aerosol-derived $MBLH$ remaining below $SBIH$ (Marsik et al., 1995) or results from the Heffter method (by about 250 m on average; Lotteraner and Piringer, 2016). Mismatches are explained by the contrasting physical processes that are being traced, such as when radiative cooling leads to the formation of a surface-based temperature inversion which is not necessarily associated with any contrasts in aerosol characteristics (Milroy et al., 2012).

Due to the lack of suitable reference data and the physical difference between aerosol-based and thermodynamic layer detection, a few studies applied manual or semi-automatic layer detection for the evaluation of aerosol-based retrievals (de Bruine et al., 2017; Poltera et al., 2017; Kotthaus and Grimmond, 2018a). Although manual detection can be a very valuable tool, it is labour-intensive and not necessarily objective (Poltera et al., 2017).

4 Monitoring ABL heights

Given ground-based remote sensing profilers have different capabilities (Sect. 2.2) and algorithm uncertainties depend on a variety of atmospheric characteristics the performance of the various ABL height (Sect. 1.1) retrieval methods (Sect. 3) changes throughout the diurnal evolution of the ABL (de Arruda Moreira et al., 2018). The following section summarises the most important strengths and weaknesses of the methods when monitoring the height of the boundary layer at night or during stable conditions (Sect. 4.1), morning growth (Sect. 4.2), peak CBL development (Sect. 4.3), and evening decay (Sect. 4.4). Further, capabilities are discussed that are relevant for the characterisation of the entrainment zone (Sect. 4.5) and the cloud-topped ABL (Sect. 4.6). Where observations from multiple ground-based atmospheric profilers are available simultaneously, analyses suggest a synergistic interpretation of results from different methods could lead to an enhanced description of the ABL, including the detection of (sub-)layer heights (Saeed et al., 2016) and the description of the processes shaping the ABL development (Manninen et al., 2018). The few available synergy applications are highlighted to indicate possible future pathways of ground-based remote sensing implementation.

It should be noted that studies directly inter-comparing ABL height retrievals based on different atmospheric quantities are still rare, especially those covering extended time periods. Given their impact on $ABLH$ uncertainty, measurement setup (such as MWR calibration, DWL focal setting and scan strategy, aerosol lidar optical overlap, amongst others; Sect. 2.2), data processing, and quality control (Sect. 3) should all be carefully evaluated when comparing results from various methods.

4.1 Nocturnal and/or stable boundary layer heights

At night, the $MBLH$ is rather shallow, with stable conditions being more likely. For the detection of shallow layers, the near-range capabilities of a ground-based remote sensing profiler are critical (Sect. 2.2). Layer heights can only be detected if they exceed a potential blind zone of the instrument and they are not obscured by sensor-related uncertainties. MWR are very suitable for shallow layer height detection given their sensitivity is maximal near the sensor (Sect. 2.2.2). High-power research lidars often do not provide information in the lowest few hundred meters (Sect. 2.2.4), meaning that ALC can be more suitable for the detection of shallow layers from aerosol profiles. A similar advantage is found for DWL in comparison to RWP (Sect. 2.2.3). Improved monitoring of the lowest few hundred metres of the atmosphere at high vertical resolution can be achieved by operating active remote sensing profilers at a low elevation angle (e.g., ALC; Poltera et al., 2017). Scanning DWL (Sect. 2.2.3) can alternate scans at low and high elevation angles, whereby the associated wind and turbulence retrievals have to assume spatial homogeneity of the atmosphere across the sampled volume.

Wind, turbulence, temperature, and humidity profiles provide further valuable insights to assess atmospheric stability (Sect. 3.1) and the processes leading to the formation of the various layers. In addition to $SBLH$, $SBIH$ can be determined from temperature profiles. Wind and turbulence observations are valuable to detect the nocturnal phenomenon of the LLJ (Sect. 3.2) and to help interpret its effects on mixing and advection of moisture, heat and pollutants (Hu et al., 2013; Reitebuch et al., 2000; Bennett et al., 2010). The relation of $SBIH$ to the position of the LLJ changes over time, with $SBIH$ increasing over the

https://doi.org/10.5194/amt-2022-14
Preprint. Discussion started: 21 April 2022

course of the night often to exceed the height of the LLJ maximum at some point (Mahrt et al., 1979). In general, discrepancy between temperature-based methods and those analysing vertical wind profiles can be profound (Beyrich and Leps, 2012).

Some systematic differences in nocturnal $MBLH$ are reported between results from the various methods available (Sect. 3), with discrepancies between layers detected based on the same or different atmospheric quantities, respectively, at the same order of magnitude. On average, uncertainty in $SBLH$ detection is estimated around 30-40% (Steeneveld et al., 2007). Since turbulence in the SBL is usually not uniform (Beyrich, 1997), the diagnosed layer heights can differ systematically from thermodynamic or aerosol-based methods. While Schween et al. (2014) find turbulence-based nocturnal $MBLH$ exceeds aerosol-based layer heights by about 300 m on average during stormy winters in rural Germany, average nocturnal $MBLH$ differences between turbulence and aerosol-based methods in London, UK, are mostly at the order of their day-to-day variability (Barlow et al., 2011; Kotthaus et al., 2018). More studies are needed to assess the impact of ABL dynamics and atmospheric stability on the relative agreement of the various methods for nocturnal layer height detection.

At night (and early morning), the detection and layer attribution of the $MBLH$ ($SBLH$) can be challenged by the presence of the RL. Layer detection becomes more uncertain if atmospheric characteristics are similar within the MBL and the RL above. As aerosol-based methods are particularly challenged by the presence of a RL, most second generation algorithms (Sect. 3.3) aim to specifically address this source of error. Further, aerosol characteristics (e.g., size distributions) and intermittent turbulence can cause signatures in attenuated backscatter and turbulence fields, respectively, that may appear as additional layer boundaries within the RL. For the turbulence analysis layer detection can be improved by distinguishing between surface-driven processes in the MBL and the decoupled mixing above (Sect. 4.7). Temperature-based layer heights (Sect. 3.1) derived from MWR profiles (Sect. 2.2.2) are less likely to mistake elevated layer boundaries for $MBLH$ as these profilers are more reliable in the near range and respond less to RL signatures.

The RL is a remnant of the previous day's CBL (Sect. 1.1), so that aerosols and moisture remaining in this elevated layer above the $MBLH$ present very suitable atmospheric tracers. While some turbulent exchange between the RL and the FT can be picked up (Fochesatto et al., 2001), the RLH can be tracked most reliably using thermodynamic retrievals (Sect. 3.1) of the CI applied to airborne in-situ sensors or by aerosol-based methods (Sect. 3.3) because the contrasts at the $ABLH$ are usually striking. As MWR profiles are generally less sensitive to contrasts near the RLH (Sect. 2.2.2) algorithms are usually not applied to radiometer profiles for the detection of this RLH. Uncertainty in RLH detection can be increased by various atmospheric processes, such as low aerosol load (reducing SNR for lidar systems; Sect. 2.2.4), advection of air masses with different aerosol or humidity content or shear layers (generated by e.g., orography, LLJ).

Instrument synergy has been identified as a promising means to better characterise the nocturnal boundary layer. Exploiting a combination of attenuated backscatter and turbulence variables derived from DWL profiles, Manninen et al. (2018) present a synergy approach to characterise the RL as the non-surface-connected region of the ABL where the turbulence activity is intermittent or absent. Collaud Coen et al. (2014) and de Arruda Moreira et al. (2020) highlight that synergy analysis of MWR and aerosol lidars data is particularly promising for nocturnal layer assessment given the respective strengths in observing $SBLH$ and RLH features. Saeed et al. (2016) use information on temperature inversion heights derived from MWR profile data to constrain an aerosol-based $SBLH$ retrieval.

https://doi.org/10.5194/amt-2022-14
Preprint. Discussion started: 21 April 2022

4.2 Morning growth

The time of $CBLH$ morning growth is characterised by substantial temporal variations, especially where solar energy input is significant (Sect. 5). Radiosonde ascends are rare between sunrise and solar noon (Sect. 2.2.1). Given the different stages of CBL development (Halios and Barlow, 2017), the continuous monitoring enabled by remote sensing profilers is a clear advantage for the characterization of this period compared to balloon ascends. Approaches based on high-frequency variations of wind (Sect.3.2) or aerosol (Sect. 3.3) often reveal pronounced signals near the $CBLH$ during this time of day. Turbulence-based $CBLH$ from RWP usually requires longer integration times (20-60 min) compared to DWL or ALC that both range in the order of minutes.

As for nocturnal conditions (Sect. 4.1), the presence of a RL can affect the detection of $CBLH$ during morning growth as entrainment of RL air (instead of air from the FT) can act to reduce the contrasts of measured quantities near the $CBLH$. Among aerosol-based approaches, detection methods that account for the potential presence of a RL in addition to $CBLH$ are more reliable (Sect. 3.3). Analysis of RWP data allows for the detection of $CBLH$ morning growth, once the turbulent signature from entrainment of RL air into the CBL is stronger than that at the RLH (Bianco et al., 2021).

Based on selected case studies, turbulence- and aerosol-based $CBLH$ during morning growth are often very similar provided appropriate layer attribution is performed (Cohn and Angevine, 2000; Collaud Coen et al., 2014). However, several studies also report a temporal delay of aerosol-derived $CBLH$ morning growth both relative to temperature-derived $CBLH$ (Wang et al., 2012; Kotthaus et al., 2020) and turbulence-derived $CBLH$ growth (Wiegner et al., 2006; Barlow et al., 2011; Kotthaus et al., 2018), with time lags of up to two hours. Presumably, it can require some time before aerosols emitted at the surface and transported upwards by turbulent mixing establish a clear layer boundary relative to the RL. In addition, entrainment of RL air with lower humidity and aerosol load may delay morning growth of aerosol-based $MBLH$ (Gibert et al., 2007). Some studies found turbulence-derived $CBLH$ to not only start rising earlier but also to grow faster than layer heights from aerosol-based methods (Barlow et al., 2011; Schween et al., 2014). However, this may be partly linked to the response of the respective detection algorithms to the presence of clouds (Wiegner et al., 2006), as Kotthaus et al. (2018) found similar growth rates when looking at cloud-free conditions only. No clear picture has yet emerged on a potential time lag between the growth of temperature- and turbulence-derived layer heights (de Arruda Moreira et al., 2018, 2019). Due to advances in algorithm development (Sect. 3), multi-sensor analysis has the potential to better quantify the relation of layer heights based on thermodynamic, dynamic and aerosol-based retrievals, respectively, which is expected to provide valuable new insights into morning ABL dynamics.

4.3 Daytime Convective Boundary Layer

Most methods (Sect. 3) show very good performance during daytime, especially when the $CBLH$ coincides with $ABLH$ (Sect. 1.1). Provided sufficient SNR and careful data processing, $CBLH$ from all retrieval methods can agree within a few hundred metres (Granados-Muñoz et al., 2012; Renju et al., 2017). If radiosonde ascends at noon are compared to ground-based remote sensing profile data, the CBL may not yet reach its full extent so that layer attribution (i.e. confusion of $CBLH$

and RLH) can be a general source of uncertainty. Sensors restricted by low SNR (such as sodar, RASS, early ALC models; Sect. 2.2), might not always reliably observe the fully developed CBL in the afternoon, especially where boundary layer development is deep and/or aerosol load is low (Boy et al., 2019).

Schmid and Niyogi (2012) highlight that a thick EZ, likely to occur during deep afternoon convection ($>$ 3 km), can result in a weaker delineation at the $ABLH$, increasing uncertainty in layer detection for all methods. While turbulence-based algorithms are challenged in the presence of strong shear layers above the ABL (Marsik et al., 1995), elevated aerosol layers increase the likelihood of false layer attribution for aerosol-based techniques (Granados-Muñoz et al., 2012; Tang et al., 2016). Layers holding advected aerosol with characteristics differing from local emissions (e.g., long-range transport of desert dust) may further alter the air temperature profile (Guerrero-Rascado et al., 2009), whereby potentially inducing errors in the applied thermodynamic retrieval (Granados-Muñoz et al., 2012). Synoptic circulation or orography-induced flow patterns that are influencing cloud conditions or the advection of decoupled layers have hence been found to affect comparison statistics (Granados-Muñoz et al., 2012; Pandolfi et al., 2013; Tang et al., 2016; Pearson et al., 2010; de Arruda Moreira et al., 2019).

Daytime maxima of the layer estimates from temperature-, turbulence-, and aerosol-based methods are most similar in clear-sky conditions (Barlow et al., 2011; de Arruda Moreira et al., 2018). In accordance with the delayed morning growth of aerosol layers (Sect. 4.2), studies often find $CBLH$ from aerosol-based methods to peak up to 2 h later than layer heights diagnosed from turbulence (Barlow et al., 2011; Kotthaus et al., 2018) or temperature profiles (Renju et al., 2017). No clear relation has yet been established between peak daytime $CBLH$ from aerosol-based retrieals and either turbulence or thermodynamic methods, as negative (Barlow et al., 2011; Kotthaus et al., 2018), positive (Schween et al., 2014; Granados-Muñoz et al., 2012; de Arruda Moreira et al., 2019), as well as no bias (Collaud Coen et al., 2014; Wang et al., 2012) are reported. Similarly, both positive, negative, and negligible deviations were found when comparing turbulence-derived $CBLH$ based on DWL data and temperature-based results obtained from MWR profiles (de Arruda Moreira et al., 2018, 2019). Further research is needed to assess which factors (including algorithm uncertainty, sampling strategy and atmospheric dynamics) best explain potential biases, accounting not only for cloud dynamics and the presence of elevated aerosol layers but also the presence of thermals overshooting the inversion at the ABL top which are inducing vast temporal variability (Renju et al., 2017; de Bruine et al., 2017) or atmospheric stability and moisture transport which can affect $CBLH$ growth rates (Helbig et al., 2021).

4.4 Evening decay

The daytime CBL transitions into the nocturnal boundary layer around sunset (Sect. 1.1). The decay in surface-driven buoyancy is directly monitored by the turbulence profiles obtained by sodars, DWL, or RWP (Sect. 2.2.3). Thermodynamic and turbulence-based $CBLH$ are in general agreement, showing a gradual decrease in the afternoon up to about sunset (Wang et al., 2012; Collaud Coen et al., 2014; Renju et al., 2017). Schween et al. (2014) illustrate the breakdown of turbulent exchange in the afternoon based on DWL profile data while Manninen et al. (2018) highlight elevated turbulence can occur during the evening transition as the RL decouples. Layer detection from RWP observations was found more uncertain in the presence of elevated shear layers (Ketterer et al., 2014).

In response to the vanishing buoyancy, aerosols start to settle in the afternoon whereby slowly forming new layer boundaries. As aerosol-based $MBLH$ is a record of the history of recent turbulence activity (Träumner et al., 2011), layer attribution is especially challenged during the time of evening CBL decay (Sect. 3.3.2). Where aerosol emissions at the surface are high (e.g., in cities), new shallow aerosol layers tend to become visible around sunset as the reduced vertical dilution increases low-level concentrations. If no clear aerosol gradient forms close to the surface around sunset (Sect. 4.1), the RLH may at times be misinterpreted as $MBLH$ in which case evening discrepancies between layer results from different methods can be at the order of magnitude of the $ABLH$. Reliable data in the near range, careful processing algorithms and high surface aerosol emission rates increase the likelihood of this transition time to be captured accurately (Sect. 3.3.2).

4.5 Entrainment zone

Characterising the entrainment zone (Sect. 1.1) around the $CBLH$ can greatly benefit interpretation of ABL dynamics, local climate conditions and air quality. The EZ thickness can be estimated either based on gradients of observed quantities between the CBL and FT (RL) or by exploiting temporal variations in $CBLH$ (Sect. 3). de Bruine et al. (2017) report differences between alternating thermals in the EZ of 100-500 m, fluctuating around an average, rather constant $ABLH$.

When aerosol-based $CBLH$ is derived at very high resolution (seconds-minutes), its temporal variation captures clear FT air being mixed into the ABL (Sect. 3.3). Turbulence-based $CBLH$ from DWL may require longer integration times (Sect. 3.2), which can be a disadvantage for the estimation of EZ thisckness (Träumner et al., 2011) based on $ABLH$ variability. Cohn and Angevine (2000) find EZ thickness based on fluctuations of $ABLH$ from RWP to be greater than those based on variations of aerosol-derived $ABLH$, as the former is associated with greater noise levels for the sensor used. The rather low range resolution of the MWR near the $ABLH$ (Sect. 2.2.2) can cause considerable uncertainty when studying the EZ based on remotely-sensed temperature profiles (Wang et al., 2012).

4.6 Cloud-topped boundary layer

While many studies focus on the analysis of clear-sky conditions, cloud-topped mixed layers are starting to receive increasing attention. Given the diverse capabilities and limitations of the remote sensing profilers for the observation of clouds (Sect. 3), the disagreement between layer estimates generally increases with cloud complexity (e.g., Cohn and Angevine, 2000; Collaud Coen et al., 2014; Cimini et al., 2013; Emeis et al., 2009). The strong attenuation of the lidar signal by water clouds causes a distinct signature in ALC and DWL profiles. Developed to record cloud base altitude, ALC inherently have built-in algorithms reporting this quantity. It should however be noted that cloud base height detection methods vary between manufacturers (Sect. 3.3) so that generalised algorithms may need to be applied during post-processing when consistent products are required across a diverse sensor network. High-power lidar systems are usually not operated under cloudy conditions (Sect. 2.2.2, 2.2.4). MWR and RWP can penetrate the layer of cloud droplets. RWP observations have been used to determine the cloud top but frequent false detection was linked to elevated layers of high humidity or turbulence (Collaud Coen et al., 2014).

Doppler cloud radars (DCR) can be used to characterize the vertical extent of boundary-layer clouds, such as shallow convective clouds, stratiform clouds (stratus or stratocumulus), and even fog. In the case of adiabatic fog, the fog layer (typically

50-400 m deep) is destabilized due to strong radiative cooling at the top coinciding with strong temperature inversion. Mixing then occurs between the fog top and the surface. Wærsted et al. (2017) combine measurements from MWR and DCR to retrieve the temperature profile in adiabatic fog layers, hence characterizing precisely the depth of the mixing.

Automatic ABL height retrieval algorithms are increasingly incorporating the presence of clouds into the layer detection and attribution process (Poltera et al., 2017; Caicedo et al., 2020). Both cloud cover and cloud type can be critical (Sawyer and Li, 2013), given convective clouds are associated with surface-driven turbulence and stratiform clouds initiate mixing by cloud dynamics (Hogan et al., 2009). Turbulence characteristics present useful information to differentiate between surface- and cloud-driven turbulence (Harvey et al., 2015). For shallow Cu clouds, the CBH may be used as a reasonable proxy for $CBLH$ where the convective nature of the cloud can be assessed by surface heat flux measurements (Schween et al., 2014; Wiegner et al., 2006) or derived from remote sensing data (Manninen et al., 2018). Depending on the retrieval applied to determine the CBH, potential biases may be introduced. For deeper Cu, the relation between cloud base and $CBLH$ is more ambiguous. In autumn and winter, the cloud base altitude is often related to the dissipation of Sc clouds or fog processes (Schween et al., 2014). The relation of CBH and $MBLH$ is subject to ongoing research.

4.7 Atmospheric stability and ABL classification

ABL dynamics respond to the synoptic flow (Shi et al., 2019), local-scale circulations induced by land cover contrasts (Moigne et al., 2013) or topography (Rotach and Zardi, 2007), surface forcing or elevated sources of turbulence associated with clouds or winds (e.g., LLJ). To understand the relative importance of all these drivers in defining ABL heights, automatic classification methods are increasingly developed. Probably the most common ABL classification is the delineation between cloudy and cloud-free conditions, which can be accomplished using surface radiation data, the cloud information reported by an ALC (Sect. 2.2.4) or by exploiting any remotely sensed profile signal sensitive to clouds (Sect. 2.2). To account for differences in ABL heights associated with cloud dynamics, ALC data have also been used to automatically distinguish simple cloud types (Kotthaus and Grimmond, 2018a). Pal et al. (2013) classify ABL regimes using cloud cover (cloudy vs clear-sky) and atmospheric stability (from surface observations) to distinguish between days dominated by local surface-driven buoyancy and those dominated by larger scale events. Using airborne profile measurements, Mahrt (1991) find ABL humidity exchanges are generally either associated with an *entrainment-drying* regime with a vertical divergence of the moisture flux or a *moistening* boundary layer dominated by surface evaporation fluxes.

As turbulence is not only driven by surface buoyancy but can also be generated aloft (e.g., by LLJ or cloud processes) additional details on the ABL dynamics can be obtained from higher order moments of turbulence observations. The sign of the vertical velocity skewness provides information on the source of turbulence, with positive values typical for surface-driven buoyancy in clear-sky CBL and negative values associated with cloud-topped boundary layers dominated by 'downwards convection' driven by radiative cooling at the cloud top (Hogan et al., 2009). The vertical velocity skewness further helps to determine whether clouds are coupled to the surface (e.g., shallow cumulus clouds) or decoupled from the surface (e.g., some nocturnal Sc; marine Sc).

Combining the various physical quantities that describe atmospheric turbulence (Sect. 2.1) with wind shear information enables detailed classification of the ABL, including the identification of the MBL stability regime (Banta et al., 2006), and the differentiation between (i) turbulence driven by buoyancy or shear (Tucker et al., 2009), surface or elevated turbulence sources (Tonttila et al., 2015; Manninen et al., 2018; Huang et al., 2020; Harvey et al., 2015), elevated turbulence sources associated with the flow (e.g. LLJ, Tuononen et al., 2017; Marke et al., 2018) or cloud dynamics (Harvey et al., 2013; Manninen et al., 2018).

Building on the profile-based classification approach from Harvey et al. (2013), Manninen et al. (2018) developed a pixel-based ABL classification scheme that exploits several atmospheric quantities derived from DWL observations. An example of a clear-sky case (Fig. 5) illustrates the complexity in ABL dynamics (Manninen et al., 2018) with diurnal variations clearly detectable from the profile data. Unstable atmospheric conditions drive the $CBLH$ morning growth in two stages (Fig. 5a,b), i.e. the slow increase of near surface convective conditions followed by a rapid growth phase (Halios and Barlow, 2017). The gradual decay of convective activity in the evening transition is clearly detected (Fig. 5a,b). A LLJ forms at some point after sunset (Fig. 5c,d).

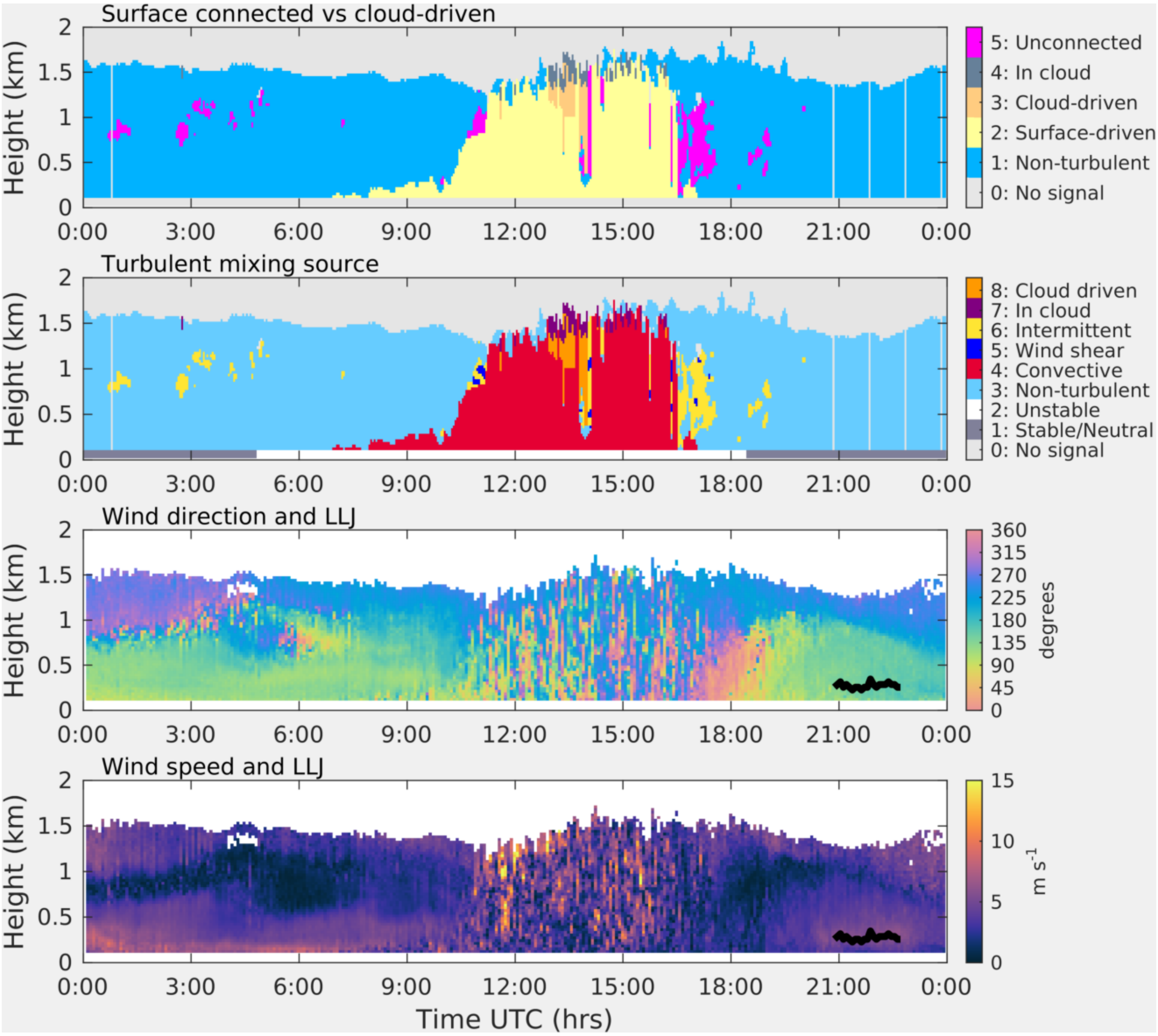

Figure 5. Time-height plots of atmospheric boundary layer classification using the Manninen et al. (2018) scheme showing (a) whether mixing is connected to the surface or cloud driven and (b) the turbulent mixing source, together with time-height plots of (c) wind direction and (d) wind speed on 28 August 2017 at Jülich, Germany. The black lines on the two lower panels show low-level jet (LLJ) altitude (Tuononen et al., 2017).

5 ABL climatology

Advances in measurement technology (Sect. 2.2), the operation of coordinated measurement networks (Sect. 2.3), and retrievals of layer heights (Sect. 3) increasingly allows for ABL climatology studies to be performed. To give an overview on the insights gained from long-term observations (here with a duration of at least one year), characteristics of ABL heights are summarised at the global scale (Sect. 5.1) and specifically over land (Sect. 5.2) and for marine environments (Sect. 5.3). Finally, it is highlighted where long-term trends in ABL heights start to emerge. While most studies considered here are using a combination of airborne in-situ or ground-based remote sensing observations, some satellite measurements and modelling studies are included to highlight the detected similarities and differences in ABL characteristics.

5.1 Atmospheric boundary layer heights at the global scale

Figure 6 provides a global picture of the midday $ABLH$ obtained from ECMWF ERA-Interim reanalysis (Figure 6a; von Engeln and Teixeira, 2013), satellite-based CALIPSO observations (Figure 6b; McGrath-Spangler and Denning, 2013), and an ensemble mean of global circulation models (Figure 6c; Davy, 2018). $ABLH$ peak values are usually bound to convective conditions driven by high surface temperatures that occur in response to strong solar irradiance, low surface albedo and low soil moisture as found e.g., over dry subtropical land regions such as the Saharan desert in summer (Messager et al., 2010; McGrath-Spangler and Denning, 2013; Guo et al., 2016; Ndao et al., 2019; Aryee et al., 2020). Over the subtropical deserts in Northern Africa and Australia, monthly average $ABLH$ >3 km a.g.l. have been reported (Ao et al., 2012) with daytime maxima exceeding 5 km. Large marine $ABLH$ values (>1.8 km) are found in the intertropical convergence zone, for example over the South Atlantic east of Brazil, the Gulf of Aden and over the western Indian Ocean. A particular phenomenon with very high $ABLH$ (up to 5 km a.g.l. corresponding to 9 km a.s.l.) occurs over the Tibetan Plateau in the winter season (Chen et al., 2013, 2016), when a deep neutral layer prevails so that the $ABLH$ approaches the upper troposphere. The lowest $ABLH$ are found in winter over polar regions when strong inversions near the ground dominate (von Engeln and Teixeira, 2013). As a general rule, lower $ABLH$ but with a large seasonality are found over high latitudes, whereas a weaker seasonality is found between 30° and 50° of latitude (Chan and Wood, 2013).

Large-scale synoptic flow and land-sea-atmosphere interactions lead to contrasting $MBLH$ characteristics between eastern and western coastlines. In the Northern hemisphere, western coastlines of continents are predominantly covered by stratocumulus clouds, whereas the eastern coasts experience a clear seasonality. Here, $MBLH$ is relatively high during winter due to cold air outbreaks and frontal systems and low during summer due to frequent fog. As a result, average $MBLH$ are lower at eastern coastlines (0.5-1.0 km) than for western coastlines (∼2 km) in the Northern hemisphere (von Engeln and Teixeira, 2013).

SBI are much more frequent during nighttime and early morning, and rarely occur between noon and sunset. In polar regions, temperature inversions over ice can be very strong in winter leading to extremely stable boundary layers (Genthon et al., 2013). The $SBLH$ can be as low as 20 m (Handorf et al., 1999), and internal gravity waves have been observed propagating along the top of the SBL (Kouznetsov, 2009). Katabatic winds arising from drainage flows even over gentle slopes are a common feature over large ice sheets and their vertical profile usually determines $SBLH$. SBI are much more frequent at high latitudes (in polar regions: 80 % and 50 % of the time at night and at midday, respectively) than in the tropical trade-wind regions ($<$50 % and $<$15% at night and midday, respectively; Seidel et al., 2010). A clear north-south gradient of $SBIH$ is established at the continental scale for both Europe and North America with greater layer heights over warmer areas (Seidel et al., 2012; Wang and Wang, 2014).

5.2 Atmospheric boundary layer over land

5.2.1 Diurnal cycle

The layer most often analysed is the CBL (Sect. 1.1) as its well-mixed characteristics generally facilitate reliable detection and attribution (Sect. 3). The diurnal amplitude of the $CBLH$ is particularly pronounced over land where the diurnal maximum is typically found between 12:00 and 17:00 local time, mostly around 15:00 local time (von Engeln and Teixeira, 2013; Guo et al., 2016; Liu and Liang, 2010; Sathyanadh et al., 2017; Gierens et al., 2018, , with a variety of methods applied). The $CBLH$ is reported to commence growing from 1-2 h (de Arruda Moreira et al., 2020, , using thermodynamic and aerosol-based retrievals) to 3-4 h (Korhonen et al., 2014, , using thermodynamic retrievals) after sunrise. The $CBLH$ growth rate usually ranges between 50- 300 m h^{-1} (Sokół et al., 2014; Pal and Haeffelin, 2015; de Arruda Moreira et al., 2020; Sathyanadh et al., 2017), with monthly mean growth rates greater than 500 m h^{-1} and hourly values as high as 900 m h^{-1} (measured over the city Leipzig, Germany; Baars et al., 2008) or 1100 m h^{-1} (over the Tibetan plateau; Chen et al., 2016). Large and small growth rates can be found in all seasons (Pal and Haeffelin, 2015; Bianco et al., 2011) as growth rates depend significantly on ABL cloud dynamics (Kotthaus and Grimmond, 2018b). The $CBLH$ growth duration varies seasonally in response to the solar input (Pal and Haeffelin, 2015). And also seasonally-dependent winds (e.g., Mues et al., 2017; Tang et al., 2016; Kokkalis et al., 2020, induced by complex terrain) or elevated aerosol layers (e.g., Kokkalis et al., 2020, through their impact on radiative forcing) can enhance or suppress CBL growth. Over dry convective regions, $CBLH$ usually begins to decay just before sunset (von Engeln and Teixeira, 2013; Bianco et al., 2011).

The CBL regime is mostly found during daytime while the SBL regime dominates at night (up to 70 % of the time) and the neutral RL accounts for remaining situations (25 % of the time) with afternoons (12:00-15:00 local time) more likely to be dominated by neutral RL (60 %) than SBL (5 %) (Liu and Liang, 2010; Collaud Coen et al., 2014; Seidel et al., 2012; Harvey et al., 2013).

The diurnal amplitude of the $MBLH$ (i.e. the layer defined independently of atmospheric stability, Sect. 1.1) is mostly driven by its afternoon peak, with generally high values over deserts and rather small variations over tropical forest and ice (von Engeln and Teixeira, 2013; Davy, 2018; Liu and Liang, 2010). But also the magnitude of nocturnal boundary layer heights play a role. The latter respond to land cover differences (e.g., urban density Hertwig et al., 2021), cloud characteristics (Mues et al., 2017; Kotthaus and Grimmond, 2018b) and wind speed (Bonin et al., 2018), whereby contributing to seasonal variations in the $MBLH$ diurnal amplitude. Stronger winds tend to enhance mechanical mixing (Mahrt et al., 2015) while greater cloud cover reduces radiative cooling, both potentially leading to increased nocturnal layer heights. Over ice, the $MBLH$ exhibits

https://doi.org/10.5194/amt-2022-14
Preprint. Discussion started: 21 April 2022

diurnal variations similar to other land cover types, but with generally lower values, a narrower distribution of altitude frequency and a lower diurnal range (Argentini et al., 2005).

5.2.2 Seasonal cycle

The $CBLH$ seasonal cycle is a consequence of the surface heat fluxes, which are again largely driven by the amount of incoming solar radiation and the ground surface temperature. Maximum $CBLH$ values are usually found during local warm and dry seasons (i.e. spring/summer or pre-monsson), whereas minimum layer heights occur during cold and cloudy seasons (i.e. winter or monsoon period). In the subtropics and tropics, the seasonal cycle is driven by the seasonality of the *intertropical convergence zone* (Chan and Wood, 2013). Examples of seasonal studies based on observations are available for diverse locations globally, incl. Europe (Matthias et al., 2004), the Netherlands (de Haij et al., 2006), USA and Europe, (Seidel et al., 2012), marine and continental sites (Luo et al., 2014), the Swiss plateau (Collaud Coen et al., 2014), China (Guo et al., 2016), Spain (de Arruda Moreira et al., 2020), India (Sathyanadh et al., 2017) and South Africa (Gierens et al., 2018). Similar to the diurnal amplitude, the largest seasonal cycles occur over desert areas in Africa, Asia and Australia, and in mountainous regions in North America and Asia (Aryee et al., 2020; McGrath-Spangler and Denning, 2013; von Engeln and Teixeira, 2013). The expected seasonal cycle in extratropical regions may be modified by local influences such as mountain winds (e.g., for Beijing, China; Tang et al., 2016) or cold marine inflow (e.g., Californian valleys, USA; Bianco et al., 2011), which are in both cases leading to seasonal maxima in spring. The greatest seasonal $CBLH$ amplitude occurs in the northern hemisphere storm tracks, where Sc-topped $CBLH$ maxima occur during the boreal autumn and winter. In the southern hemisphere sea ice polar region, the $ABLH$ maxima are found in the early austral autumn when a minimum in sea-ice coverage enables the highest sea surface temperatures (Medeiros et al., 2005).

Some studies for Europe and North America find that the nocturnal $SBIH$ or $SBLH$ (from bulk Richardson number; Sect. 3.1) reach greater heights in winter than in summer, i.e. showing a behaviour opposite to the $CBLH$ seasonal cycle (Seidel et al., 2010, 2012; Beyrich and Leps, 2012; Koffi et al., 2016). This inverse seasonal cycle was tentatively attributed to the combined effects of a more frequent occurrence of strong temperature inversions in summer driven by a lower cloud cover and to increased mean wind speeds in winter leading to enhanced mechanical mixing. Some authors question the validity of these seasonal cycles due to the larger uncertainties associated with shallow $SBLH$ detection (Sect. 4.1).

Very long observational records now allow for the examination of inter-annual variations in seasonal and diurnal variability (e.g., Pal and Haeffelin, 2015; Wang et al., 2020). Such studies demonstrate that regional to global scale phenomena such as heat waves or the El Niño Southern Oscillation (ENSO) have an imprint on ABL heights.

5.2.3 The urban boundary layer

The structure of the urban boundary layer is increasingly considered for the interpretation and modelling of air quality and greenhouse gas emissions (e.g., Klein et al., 2017; Lauvaux et al., 2016; Shi et al., 2019; Wu et al., 2019; de Arruda Moreira et al., 2020; Piringer et al., 2007). Observational evidence reveals that ventilation (i.e. a combination of horizontal advection and vertical dilution) is a particularly important driver for near-surface pollutant concentrations when buoyancy is weak (e.g., Lee et al., 2019; Stirnberg et al., 2021; Sujatha et al., 2016).

Short-term measurement campaigns (for example in Paris or London; Pal et al., 2012; Barlow et al., 2015) have shown that the urban CBL is often deeper than over the suburban and even more over the rural surroundings (see review by Barlow, 2014). The enhanced buoyancy (and reduced moisture) over the urban surface has even been linked to higher cloud base altitudes of boundary layer clouds (Theeuwes et al., 2019). The well-studied urban heat island effect also influences $MBLH$ at night, with layer heights over the city centre systematically higher (up to 200-300 m) and more heterogeneous (Pal et al., 2012). Urban areas can maintain slightly unstable stratification well into (or even throughout) the night, suggesting nocturnal low-level jets are initiated over rural areas instead (Barlow et al., 2015).

Long-term climatological observations of the urban boundary layer have been performed in several cities, including Athens, Greece (Kokkalis et al., 2020), Beijing, China (Tang et al., 2016; Chu et al., 2019), Granada, Spain (Granados-Muñoz et al., 2012; de Arruda Moreira et al., 2020), Hong Kong, China (Huang et al., 2020), Houston, Texas, USA Haman et al. (2012), Leipzig, Germany (Baars et al., 2008), London, UK (Kotthaus and Grimmond, 2018b), Paris, France (Pal and Haeffelin, 2015), Shanghai, China (Peng et al., 2017), Vancouver, Canada (van der Kamp and McKendry, 2010), Vienna, Austria (Lotteraner and Piringer, 2016), Yuen Long, China (Yang et al., 2013), and Warsaw, Poland (Wang et al., 2020). However, only a few studies include a rural reference site. Lotteraner and Piringer (2016) analyse one year of $MBLH$ observations in Vienna at a central urban and a rural site and found an increment of $CBLH$ over the city with a mean midday difference <100 m. This difference was explained not only by enhanced vertical mixing over the city, but also by local topographic features that further support a more rapid urban morning growth rate. Dense observational networks are starting to emerge in urban settings, responding to to the need of a more detailed understanding of the urban boundary layer in a wide variety geographical settings and across the diverse and heterogeneous characteristics of the urban surface and anthropogenic activities.

5.2.4 The boundary layer over complex topography

Although the $MoBL$ is affected by severe spatial and temporal complexity, some general characteristics and mechanisms have been quantified. As for the ABL development over other land regions, the heights of the various $MoBL$ sublayers and the resulting exchanges with the FT are highest (lowest) during local summer (winter) time. This has been observed for CBL over the valley floor (Herrera-Mejía and Hoyos, 2019), the aerosol layer (AL) (Poltera et al., 2017), plain-to-mountain venting (Hulin et al., 2019), as well as the altitude of the valley winds (Schmid et al., 2020). High-altitude sites are hence often sampling FT air during winter (Andrews et al., 2011). Still, the ABL influence at a given mountain measurement site needs to be assessed carefully because the station altitude is not necessarily the main criterion (Collaud Coen et al., 2018). In a valley with dense urbanization, pollution episodes are most severe in cold conditions when the $CBLH$ remains lower than the ridge altitude (Herrera-Mejía and Hoyos, 2019).

The occurrence of up-down valley winds (adabatic and katabatic winds) is directly bound to the times of sunrise and sunset (Hooda et al., 2018) and are originate at the valley floor (Schmid et al., 2020). Slopes exposed to morning sunshine cause earlier slope wind development, an erosion of the nocturnal thermal inversion and the set-in of a cross-valley circulation (Adler et al., 2021). $CBLH$ maxima in the valley floor are higher and occur earlier than those on the slope of the valley (Herrera-Mejía and Hoyos, 2019). The $MoBL$ tends to follow the terrain in the morning and to flatten to a level of 0.5-2.0 km over range altitude during the afternoon (De Wekker and Kossmann, 2015; Pal et al., 2012; Nyeki et al., 2002). As long-term ABL measurements remain scarce over complex topography, many characteristics of the $MoBL$ are still poorly understood. More ABL profile observations representing the diversity in mountainous topographies, soil properties and mesoscale influences are required to reach a more global comprehension of the MoBL complexity.

5.3 Marine environments

5.3.1 Atmospheric boundary layer over the ocean

The marine ABL exhibits similar dynamics as the boundary layer over land (Sect. 5.2), however, the lower variability in sea surface temperature, marine air temperature, and surface sensible heat fluxes cause structural differences in layer heights. While the daytime maxima in $MBLH$ are smaller compared to over land (Figure 6b; McGrath-Spangler and Denning, 2013)), the daily average marine $MBLH$ is deeper overvall (Figure 6a,c; von Engeln and Teixeira, 2013; Davy, 2018)) due to its reduced diurnal amplitude (Medeiros et al., 2005; Liu and Liang, 2010). Some studies find ocean $MBLH$ peak values around solar noon (Liu and Liang, 2010), but the marine $MBLH$ diurnal cycle is often rather indiscernible, which can be explained by a persistent capping inversion (Medeiros et al., 2005; von Engeln and Teixeira, 2013; Chan and Wood, 2013; Luo et al., 2014; Sathyanadh et al., 2017). Over land, significant amounts of heat and mass are exchanged between the ABL and FT over the course of the day (Stull, 1988). Over the ocean again, the overall lower exchanges are mostly accomplished by cloud dynamics of the predominant Sc- or Cu- topped ABL (Medeiros et al., 2005; Martin et al., 2000). CBL conditions are more frequent over the oceans with unstable stratification even persisting at night. The neutral RL regime is more rare over the ocean during daytime, with its frequency reduced by 20 %–33 % compared to the average land boundary layer (Liu and Liang, 2010).

The greatest seasonal amplitude of marine $ABLH$ occurs over the Arctic (Chan and Wood, 2013). A seasonal asymmetry is observed about the equator with maxima during winter in the Northern hemisphere and in autumn (dry season) in the South, respectively. Seasonal variability again is more pronounced over the Northern hemisphere driven by the larger land area (Chan and Wood, 2013). Significant seasonal amplitudes in oceanic $ABLH$ do occur over the Mediterranean Sea (von Engeln and Teixeira, 2013) or the Gulf Stream (Seidel et al., 2012). A longitudinal dependence of marine $ABLH$ has been detected by satellite and model analyses over the Pacific ocean with higher values at -85° (1.5 km) than at -70° (1 km) (Ho et al., 2015, figure 11).

5.3.2 Coasts, islands and lakes: a mix between marine and land signatures

The ABL climatology for coastal regions reflects the combination of sea-influence and local meteorological phenomena (e.g., induced by particular topography and/or land cover). Similarly, large lakes have been associated with marine boundary layer characteristics (Liu and Liang, 2010; Moigne et al., 2013; Potes et al., 2017), with effects becoming more pronounced with increasing lake area. Coastal $ABLH$ show less annual variability than inland, likely due to the moderating influence of the sea (Seidel et al., 2012; Sathyanadh et al., 2017). Regional dynamics such as local breeze circulations responding to thermal contrasts between the lake or ocean and the adjacent land have systematic implications for the boundary layer heights. Circulations can lead to rapid decreases in $ABLH$ at the transition between the land and sea breeze regime. Through such dynamics, shallower average $ABLH$ often occur in summer rather than in autumn or even winter, as found for e.g., Miami, Brookhaven and New York, USA (Niyogi, 2015; Melecio-Vázquez et al., 2015), Denmark (Peña et al., 2013), Athens, Greece, and Lecce in Italy (Matthias et al., 2004), or Shanghai, China (Peng et al., 2017)). At other coastal locations (e.g., Vancouver, Canada), the average $ABLH$ is highest in summer, with peak daily maxima in spring, when added buoyancy provided by latent heat release associated with boundary-layer cloud formation enhances growth (van der Kamp and McKendry, 2010). Woolway et al. (2017) demonstrate that latitude is the most important factor determining ABL stability for larger lakes (area greater than 10 km^2), as unstable CBL become increasingly frequent at lower latitudes. In addition to land-sea contrasts, coastal topography can play an important role. For example, Bianco et al. (2011) associate the observed minimum average $ABLH$ (41-108 m a.s.l.) during summer at four sites in California's Central Valley, USA, with topographically forced cold-air advection and local land-use characteristics.

The $ABLH$ diurnal cycle characteristics for oceanic islands presents a superimposition of the continental and marine ABL processes (Liu and Liang, 2010), with the ABL over volcanic islands combining the complex terrain effects (such as mountain venting processes) and maritime phenomena.

5.4 Cloudy versus clear sky conditions

$CBLH$ growth rates and maxima are strongly affected by clouds as the latter modulate the incoming solar radiation and hence the energy available for buoyancy production. However, to date the majority of $ABLH$ climatology studies focus on clear-sky conditions to avoid uncertainties in layer retrievals associated with clouds (Sect. 4.6). Where clouds are considered during $ABLH$ analysis, studies mostly focus on cloud cover as local information on cloud type is still scarce. Seasons with greater cloud coverage usually exhibit greater variability in measured $ABLH$ (Pal and Haeffelin, 2015). Some studies (e.g., Payerne, Switzerland; Collaud Coen et al., 2014, Jülich, Germany; Schween et al., 2014) find no clear differences in CBL phenomenology, whereas others report pronounced effects of cloudy skies (such as $CBLH$ on average greater by 100-500 m on cloud-free days Guo et al., 2016). The nocturnal $SBLH$ and $SBIH$ climatology observed over the Swiss plateau (Collaud Coen et al., 2014) presents clear differences between clear-sky and cloudy conditions, as the layer heights are confined to ∼500–700 m for cloud base heights between 500-2400 m but can expand up to 1000 m otherwise.

Cloud-cover alone may be insufficient to assess the impact of clouds on boundary layer dynamics (Sect. 4.6; Pal and Haeffelin, 2015). Especially differentiating between boundary layer clouds and those decoupled from the ABL (Nowak et al., 2021) greatly aids interpretation. For both Paris, France (Pal and Haeffelin, 2015) and London, UK (Kotthaus and Grimmond, 2018b), aerosol-derived $MBLH$ (Sect. 3.3.1) was found to vary with cloud type. Daytime maxima are lowest for stratiform clouds and highest for convective clouds, with cloud-free $MBLH$ in-between. Peak $CBLH$ development was detected on days when broken convective clouds formed at the ABL top after a clear-sky night.

5.5 Trends in atmospheric boundary layer heights

Trend analysis requires a homogeneous measurement time series of at least 10 years. As such time series from ground-based remote sensing observations are only starting to become available, published trend analyses mostly rely on radio-sounding time series (Zhang et al., 2013; Guo et al., 2019; Li et al., 2020; Zhang and Seidel, 2011; Diaz et al., 2019; Zhou et al., 2021) or on the data assimilation system ERA-interim reanalysis (Darand and Zandkarimi, 2019; Ndao et al., 2019). So far, trend analyses focus on daytime conditions given the higher detection uncertainty (Sect. 4.1) combined with smaller magnitudes of nocturnal layer heights make it more challenging to assess statistically significant long-term trends.

Positive, statistically significant trends in daily $ABLH$ have been detected over Europe (1973-2010; Zhang et al., 2013)), China (1979-2003; Guo et al., 2019)), Iran (1979-2016; Darand and Zandkarimi, 2019)), the Sahara Desert and Arabian Peninsula (1979–2019 Zhou et al., 2021)) as well as in central USA, Europe, Africa, East and Southeast Asia and East Australia (1973-2018 Li et al., 2020)). In contrast, negative, statistically significant trends have been found over coastal US, India and West Australia (1973-2018; Li et al.,2020, 1979–2019; Zhou et al.,2021), and China (2004-2016; Guo et al., 2019). The $ABLH$ trends over China are spatially heterogeneous. At the global scale, an average increase in $ABLH$ of ∼100 m per decade has been reported (1973-2018; Li et al., 2020)), with maxima of ∼150 m per decade but also lower values of 31 m per decade over Iran (1979-2016) or 76 m per decade over Europe (1973-2010). Trends mostly peak in spring and at times in summer seasons.

Several studies address the $ABLH$ trend over Arctic regions. For example, Zhang and Seidel (2011) find both positive (Alaska) and negative (Canada and Europe) statistically significant changes in $SBIH$ (1990-2009) and hence conclude no clear trend dominates the whole Arctic region. Diaz et al. (2019) locate a series of statistically significant trends (1981-2010) for the marine boundary layer over the Atlantic Ocean, including an increase in the height of the marine boundary layer, a thinning of the temperature inversion layer and a weakening of the atmospheric stability.

Long-term trends in clear-sky $ABLH$ have been found to be correlated to a range of indicators that can help reveal further insights on the physical processes involved. Positive (negative) correlations with surface air temperature (relative humidity) are detected most widely (Zhang et al., 2013; Guo et al., 2019; Li et al., 2020; Darand and Zandkarimi, 2019; Zhou et al., 2021). Increasing $ABLH$ is further in line with an increasing diurnal amplitude of air temperature (India and Central Asia Liu and Liang, 2010; Li et al., 2020), while negative trends in $ABLH$ have been associated with reductions in 10 m wind speeds (74 WMO stations around the world Li et al., 2020), reductions in soil moisture and lower tropospheric stability (China Guo et al., 2019) as well as with a decreasing vertical temperature gradient between 950-700 hPa (74 WMO stations around the world Li et al., 2020).

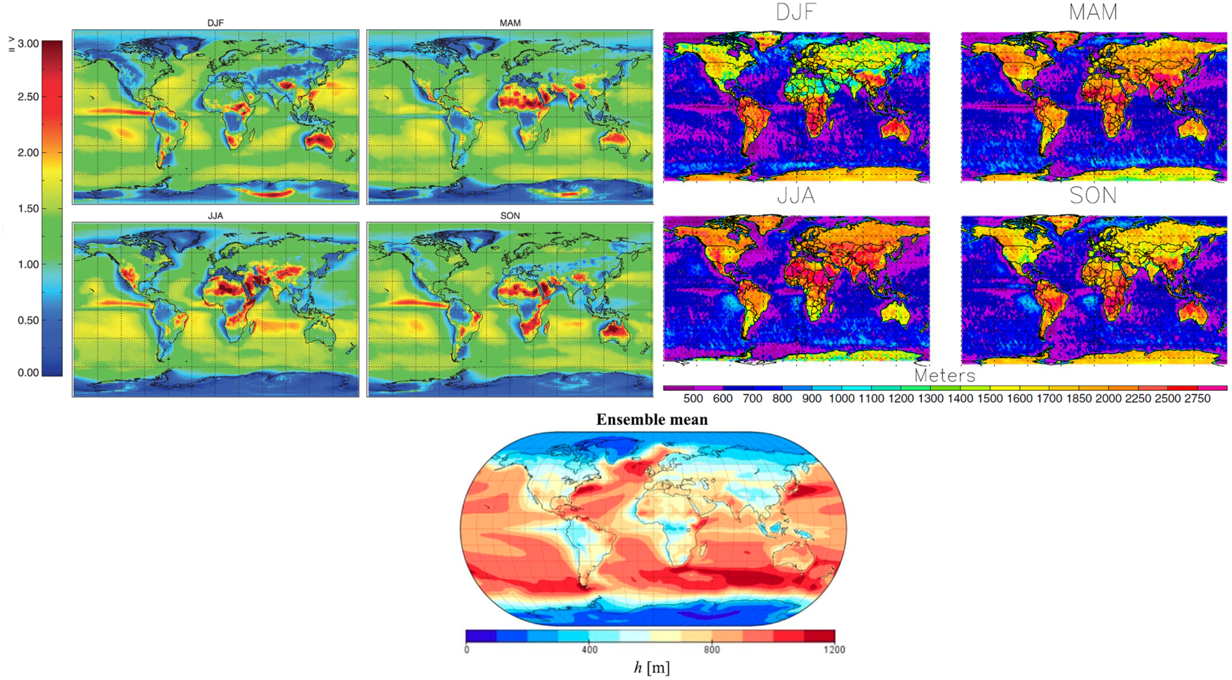

Figure 6. a) daily mean $ABLH$ estimated by the humidity gradient from 20 years of ECMWF ERA-Interim reanalysis data (von Engeln and Teixeira, 2013), b) mean midday $ABLH$ measured by the Lidar backscattering gradient from 6 years of CALIPSO data in the absence of optically thick clouds (McGrath-Spangler and Denning, 2013) and c) daily mean $ABLH$ determined by the Ri_b method as ensemble climatology from 18 contemporary general circulation models in the simulations of the late-twenties-century climate (Davy, 2018).

https://doi.org/10.5194/amt-2022-14
Preprint. Discussion started: 21 April 2022

6 Conclusions

Despite the importance for a range of applications, quantitative knowledge on the temporal and spatial variations in atmospheric boundary layer (ABL) height is still scarce. The overarching objective of this review is to emphasize how ground-based remote sensing methods are best exploited in order to gain a detailed understanding of ABL layers, their heights and dynamics. Due to advances in algorithm development, multi-sensor analysis has the potential to better quantify the relationship between layer heights based on thermodynamic, dynamic and aerosol-based retrievals, and is therefore expected to provide valuable new insights into ABL dynamics. Advances in measurement technology, the operation of coordinated measurement networks, and developments of automatic layer height retrievals increasingly allows for ABL climatology studies to be performed. To demonstrate the vast potential of increased ABL monitoring efforts, long-term observational studies are reviewed summarising our current understanding of ABL height variations at the global scale and specifically over land or for marine environments. Interestingly, even long-term trends start to emerge.

As dense measurement networks are emerging across Europe and other parts of the world with high spatial coverage, harmonisation of operations, data processing and layer height retrievals are key. This review summarises capabilities and limitations of various measurement technologies available to capture a wide range of atmospheric profile variables within the ABL as well as the numerous methods to derive the height of the ABL and its most prominent sublayers, namely the mixing boundary layer height (MBLH) and the height of the residual layer (RLH). The MBLH represents the stable (SBLH) or convective boundary layer height (CBLH), respectively, depending on atmospheric stability conditions. In addition to layer height retrievals, methods are discussed which characterise the ABL according to cloud dynamics, atmospheric stability, or aerosol transport regimes based on atmospheric profile observations.

An overview is provided on the capabilities and limitations of the large number of layer height retrieval methods, including thermodynamic methods, wind and turbulence retrievals and those based on aerosol information. Retrievals based on temperature, turbulence or wind can take into account the atmospheric stratification of the probed layer and are hence able to specifically address either SBLH or CBLH. The height of the surface-based temperature inversion (SBIH) can further be determined from temperature profile data while a low-level jet can be diagnosed from wind observations. Aerosol-based methods again analyse the result of recent mixing processes without being able to determine whether the tracers were transported as a result of thermal buoyancy or shear-driven turbulence and are hence able to track MLBH or RLH. The latter can also be assessed based on the height of the capping inversion (CI) in a temperature profile.

For the detection of shallow layers, the near-range capabilities of a ground-based remote sensing profiler are critical. MWR are very suitable given their sensitivity is maximal near the sensor, ALC have better near-range capabilities than high-power research lidars and scanning DWL can reduce the blind zone by adding shallow-angle scan strategies. On average, uncertainty in SBLH detection is estimated around 30-40 %. Since turbulence in the SBL is usually not uniform, the diagnosed layer heights can differ systematically between thermodynamic, turbulence, or aerosol-based methods. Most methods are challenged when multiple layers are present as the task of layer attribution is considered more uncertain than the simple task of layer detection. Hence at night and early morning, aerosol-based methods are at risk to confuse MBLH and RLH, especially if the

https://doi.org/10.5194/amt-2022-14
Preprint. Discussion started: 21 April 2022

composition is similar within the two layers. But also turbulence-base layer detection algorithms can be challenged by the presence of intermittent turbulence in the RL. Thermodynamic layer detection from MWR profile data is less suitable for the detection of RLH (given lower sensitivity) so that the RL poses less of the problem for the detection of MBLH at night and early morning. The RLH can be tracked most reliably using thermodynamic retrievals of the CI applied to airborne in-situ sensors or by aerosol-based methods.

Given the different stages of CBL development during morning growth, the continuous monitoring enabled by remote sensing profilers is a clear advantage for the characterization of this period compared to balloon ascends. Approaches based on high-frequency variations of wind or aerosol are often particularly good at tracking CBLH during morning growth. Turbulence-based results from RWP usually requires longer integration times compared to DWL or ALC that range in the order of minutes. Turbulence- and aerosol-based CBLH during morning growth can be very similar provided appropriate layer attribution is performed. However, several studies report a temporal delay of aerosol-derived CBLH morning growth both relative to temperature-derived CBLH and turbulence-derived growth, with time lags of up to two hours. No clear picture has yet emerged on a potential time lag between the growth of temperature- and turbulence-derived layer heights.

Most methods show very good performance during daytime, especially when the CBL is fully developed over the entire ABL. Provided sufficient SNR and careful data processing, CBLH from all retrieval methods can agree within a few hundred metres. A large entrainment zone (EZ) can result in a weaker delineation at the CBLH, increasing uncertainty in layer detection for all methods. As convective clouds can significantly challenge layer detection, daytime maxima of the layer estimates from temperature-, turbulence-, and aerosol-based methods are most similar in cloud-free conditions. However, also strong shear layers or elevated aerosol layers above the ABL can challenge turbulence-based and aerosol-based algorithms, respectively.

The evening transition of the daytime CBL into the nocturnal boundary layer around sunset is directly monitored by turbulence profiles. While turbulence-based layer retrievals and thermodynamic methods are in general agreement at this time of day, aerosol-based MBLH results are particularly uncertain during this time of evening decay as it tries to track the history of recent turbulence activity. Reliable data in the near range, careful processing algorithms and high surface aerosol emission rates increase the likelihood of this transition time to be captured accurately by aerosol profiling methods.

A list of aspects is identified that require increased attention by future studies.

- The detection and interpretation of nocturnal layer heights is still prone to significant uncertainty. Further investigation is required into the impact of ABL dynamics and atmospheric stability on the relative agreement between methods. At night, instrument synergy between microwave radiometer (MWR) temperature profiling and aerosol observations from automatic lidars and ceilometers (ALC) is particularly promising given their respective strengths in observing the SBLH and RLH.

- Most striking differences in detected layer heights are found for the CBLH during morning growth when there may be a time lag between retrievals that use thermodynamic profiles, turbulence profiles or aerosol profiles, respectively. Again, detailed method synergy of high resolution observations (both in time and vertical dimension) is a promising means to gain novel insights.

- Although CBLH growth rates and maxima are strongly affected by clouds, the majority of ABLH climatology studies to date focus on clear-sky conditions. Cloud cover or even cloud type are considered very rarely. Recent developments in automatic detection algorithms that now consider cloud dynamics are expected enable more comprehensive assessments in the future. Especially differentiating between boundary layer clouds and those decoupled from the ABL greatly aids interpretation.

- Incorporating ABL classification schemes that not only provide layer heights but also assess the source (surface-driven, cloud-driven) and nature (buoyancy, shear) of turbulent exchange into the analysis is expected to provide novel insights into the relation between MLH and cloud dynamics.

- To achieve a better process understanding of ABL dynamics in heterogeneous environments (such as the urban boundary layer or the boundary layer in complex terrain), very dense spatial measurement networks are required representing the diversity in topographic settings, surface cover characteristics, and climatological conditions.

- In any case, careful processing and detailed quality control are vital to produce high-quality profile observations. This is particularly critical for measurement uncertainties that propagate to the accuracy of ABL height retrievals.

- Choosing the appropriate technology for a given network not only needs to consider the physical information content of the atmospheric quantity observed (temperature, humidity, wind, turbulence, aerosol, or gas) but also whether the sensitivity, resolution, and capabilities of a given sensor are appropriate to monitor the layer(s) of interest. Such instrument characteristics not only differ between sensor types but also between models from different manufacturers and can depend even on firmware, hardware, instrument settings, instrument age, or sampling strategies.

It can be concluded that ground-based ABL profile remote sensing is a powerful means to gain high-resolution observations of the atmospheric boundary layer – to date, the most under-sampled part of the atmosphere. The diversity in measurement technology and algorithm variety bears a challenge for the quantification of retrieval uncertainty but should also be considered an advantage for powerful process studies and synergy exploitation of the increasingly rich operational measurement networks.

Code availability. Not applicable

Data availability. Not applicable

Code and data availability. Not applicable.

Author contributions. SK prepared the manuscript with the following co-author contributions: JABA [Sections 1, 2], MCC [Sections 1, 2, 3, 5], JLGR [Section 1, 2, 4], MJC [Section 1, 2, 4], DC [Sections 2, 3], EJOC [Section 2, 3, 4], MHe [Section 2], MHa [Section 3]. The manuscript is based on an earlier version that was led by JABA. MJP and JABA created Figure 2 and Figure 3. All authors contributed to the manuscript outline. MHa and LAA performed a final revision of the manuscript. AI and DR contributed with funding support through their roles as chairs of the COST Action TOPROF. MHa and DC contributed with funding support through their roles as chairs of the COST Action PROBE.

Competing interests. The authors declare no conflict of interest.

Acknowledgements. This article is based upon work from COST Action CA18235 PROBE, supported by COST (European Cooperation in Science and Technology, www.cost.eu). Support from COST Action ES1303 TOPROF is also acknowledged. SK is funded by DIM-Qi2 (Réseau de recherche Qualité de l'air en Ile-de-France) and Agence National de la Recherche under contract #ANR-20-CE22-0013 (H2C). LAA, JABA, JLGR thank the Spanish Ministry of Economy and Competitiveness (MINECO) for support through project ELPIS (PID2020-120015RB-I00), INTEGRATYON^3 (PID2020.117825GB.C21), the Regional Government of Andalusia through project AEROPRE (P18-RT-3820) and ADAPNE (P20-00136), and the University of Granada, Programa Operativo FEDER Andalucia 2014-2020 through project DEM3TRIOS (A-RNM-430-UGR20) and the Earth System Excellence Units Program. JABA received funding from the Marie Sklodowska-Curie Action Cofund 2016 EU project – Athenea3i under grant agreement no. 754446. MJC is co-funded by national Portuguese funds through FCT - Fundação para a Ciência e Tecnologia, I.P., in the framework of the ICT project with the references UIDB/04683/2020 and UIDP/04683/2020, as well as through TOMAQAPA (PTDC/CTAMET/29678/2017) project.

References

Abril-Gago, J., Guerrero-Rascado, J. L., Costa, M. J., Bravo-Aranda, J. A., Sicard, M., Bermejo-Pantaleón, D., Bortoli, D., Granados-Muñoz, M. J., Rodríguez-Gómez, A., Muñoz-Porcar, C., Comerón, A., Ortiz-Amezcua, P., Salgueiro, V., Jiménez-Martín, M. M., and Alados-Arboledas, L.: Statistical validation of Aeolus L2A particle backscatter coefficient retrievals over ACTRIS/EARLINET stations in the Iberian Peninsula, Atmos. Chem. Phys., pp. 1–51, https://doi.org/10.5194/ACP-2021-388, 2021.

Adler, B., Gohm, A., Kalthoff, N., Babić, N., Corsmeier, U., Lehner, M., Rotach, M. W., Haid, M., Markmann, P., Gast, E., Tsaknakis, G., and Georgoussis, G.: CROSSINN: A Field Experiment to Study the Three-Dimensional Flow Structure in the Inn Valley, Austria, Bull. Amer. Meteor. Soc., 102, E38 – E60, https://doi.org/10.1175/BAMS-D-19-0283.1, 2021.

Allabakash, S., Yasodha, P., Bianco, L., Venkatramana Reddy, S., Srinivasulu, P., and Lim, S.: Improved boundary layer height measurement using a fuzzy logic method: diurnal and seasonal variabilities of the convective boundary layer over a tropical station, J. Geophys. Res. Atmos., 122, 9211–9232, https://doi.org/10.1002/2017JD027615, 2017.

AMS, A. M. S.: American Meteorological Society Glossary of Meteorology, http://glossary.ametsoc.org/, 2017.

Andrews, E., Ogren, J., Bonasoni, P., Marinoni, A., Cuevas, E., Rodríguez, S., Sun, J., Jaffe, D., Fischer, E., Baltensperger, U., Weingartner, E., Coen, M. C., Sharma, S., Macdonald, A., Leaitch, W., Lin, N.-H., Laj, P., Arsov, T., Kalapov, I., Jefferson, A., and Sheridan, P.: Climatology of aerosol radiative properties in the free troposphere, Atmos. Res., 102, 365–393, https://doi.org/https://doi.org/10.1016/j.atmosres.2011.08.017, 2011.

Angelini, F., Barnaba, F., Landi, T. C., Caporaso, L., and Gobbi, G. P.: Study of atmospheric aerosols and mixing layer by LIDAR, Radiation protection dosimetry, 137, 275–279, https://doi.org/10.1093/rpd/ncp219, 2009.

Angevine, W., Senff, C., and Westwater, E.: Boundary layers/Observational Techniques-Remote, in: Encyclopedia of Atmospheric Sciences, edited by Holton, J. R., pp. 271–279, Academic Press, Oxford, https://doi.org/10.1016/B0-12-227090-8/00089-0, 2003.

Angevine, W. M., White, A. B., and Avery, S. K.: Boundary-layer depth and entrainment zone characterization with a boundary-layer profiler, Boundary-Layer Meteorol., 68, 375–385, https://doi.org/10.1007/BF00706797, 1994.

Ansmann, A., Wandinger, U., Riebesell, M., Weitkamp, C., and Michaelis, W.: Independent measurement of extinction and backscatter profiles in cirrus clouds by using a combined Raman elastic-backscatter lidar, Appl. Opt., 31, 7113–7131, 1992.

Ao, C. O., Waliser, D. E., Chan, S. K., Li, J.-L., Tian, B., Xie, F., and Mannucci, A. J.: Planetary boundary layer heights from GPS radio occultation refractivity and humidity profiles, J. Geophys. Res. Atmos., 117, https://doi.org/10.1029/2012JD017598, d16117, 2012.

Argentini, S., Viola, A., Sempreviva, A., and Petenko, I.: Summer boundary-layer height at the plateau site of Dome C, Antarctica, Boundary-Layer Meteorol., 115, 409–422, 2005.

Aryee, J. N. A., Amekudzi, L. K., Preko, K., Atiah, W. A., and Danuor, S. K.: Estimation of planetary boundary layer height from radiosonde profiles over West Africa during the AMMA field campaign : Intercomparison of different methods, Scientific African, 7, https://doi.org/10.1016/j.sciaf.2019.e00228, 2020.

Baars, H., Ansmann, A., Engelmann, R., and Althausen, D.: Continuous monitoring of the boundary-layer top with lidar, Atmos. Chem. Phys., 8, 7281–7296, https://doi.org/10.5194/acp-8-7281-2008, 2008.

Baars, H., Kanitz, T., Engelmann, R., Althausen, D., Heese, B., Komppula, M., Preißler, J., Tesche, M., Ansmann, A., Wandinger, U., Lim, J.-H., Ahn, J. Y., Stachlewska, I. S., Amiridis, V., Marinou, E., Seifert, P., Hofer, J., Skupin, A., Schneider, F., Bohlmann, S., Foth, A., Bley, S., Pfüller, A., Giannakaki, E., Lihavainen, H., Viisanen, Y., Hooda, R. K., Pereira, S. N., Bortoli, D., Wagner, F., Mattis, I., Janicka, L., Markowicz, K. M., Achtert, P., Artaxo, P., Pauliquevis, T., Souza, R. A. F., Sharma, V. P., van Zyl, P. G., Beukes, J. P., Sun, J., Rohwer,

E. G., Deng, R., Mamouri, R.-E., and Zamorano, F.: An overview of the first decade of Polly$^{\mathrm{NET}}$: an emerging network of automated Raman-polarization lidars for continuous aerosol profiling, Atmos. Chem. Phys., 16, 5111–5137, https://doi.org/10.5194/acp-16-5111-2016, 2016.

Ballish, B. A., Kumar, V. K., Ballish, B. A., and Kumar, V. K.: Systematic Differences in Aircraft and Radiosonde Temperatures, Bull. Amer. Meteor. Soc., 89, 1689–1708, https://doi.org/10.1175/2008BAMS2332.1, 2008.

Balsley, B. B., Frehlich, R. G., Jensen, M. L., and Meillier, Y.: High-resolution in situ profiling through the stable boundary layer: Examination of the SBL top in terms of minimum shear, maximum stratification, and turbulence decrease, J. Atmos. Sci., 63, 1291–1307, https://doi.org/10.1175/JAS3671.1, 2006.

Banakh, V. A. and Smalikho, I. N.: Estimation of the turbulence energy dissipation rate from pulsed Doppler lidar data, Atmos. Oceanic Opt., 10, 957–965, 1997.

Banakh, V. A. and Smalikho, I. N.: Lidar observations of atmospheric internal waves in the boundary layer of the atmosphere on the coast of Lake Baikal, Atmos. Meas. Tech., 9, 5239–5248, https://doi.org/10.5194/amt-9-5239-2016, 2016.

Banakh, V. A., Smalikho, I. N., Pichugina, E. L., and Brewer, W. A.: Representativeness of measurements of the dissipation rate of turbulence energy by scanning Doppler lidar, Atmos. Oceanic Opt., 23, 48–54, https://doi.org/10.1134/S1024856010010100, 2010.

Banks, R. F., Tiana-Alsina, J., Rocadenbosch, F., and Baldasano, J. M.: Performance Evaluation of the Boundary-Layer Height from Lidar and the Weather Research and Forecasting Model at an Urban Coastal Site in the North-East Iberian Peninsula, Boundary-Layer Meteorol., 157, 265–292, https://doi.org/10.1007/s10546-015-0056-2, 2015.

Banta, R. M., Senff, C. J., White, A. B., Trainer, M., McNider, R. T., Valente, R. J., Mayor, S. D., Alvarez, R. J., Hardesty, R. M., Parrish, D., and Fehsenfeld, F. C.: Daytime buildup and nighttime transport of urban ozone in the boundary layer during a stagnation episode, J. Geophys. Res. Atmos., 103, 22 519–22 544, https://doi.org/10.1029/98JD01020, 1998.

Banta, R. M., Pichugina, Y. L., and Brewer, W. A.: Turbulent velocity-variance profiles in the stable boundary layer generated by a nocturnal low-level jet, J. Atmos. Sci., 63, 2700–2719, https://doi.org/10.1175/JAS3776.1, 2006.

Banta, R. M., Pichugina, Y. L., Kelley, N. D., Hardesty, R. M., and Brewer, W. A.: Wind Energy Meteorology: Insight into Wind Properties in the Turbine-Rotor Layer of the Atmosphere from High-Resolution Doppler Lidar, Bull. Amer. Meteor. Soc., 94, https://doi.org/10.1175/BAMS-D-11-00057.1, 2013.

Barlow, J., F., Dunbar, T. M., Nemitz, E. G., Wood, C. R., Gallagher, M., Davies, F., O'Connor, E., and Harrison, R. M.: Boundary layer dynamics over London, UK, as observed using Doppler lidar during REPARTEE-II, Atmos. Chem. Phys., 11, 2111—-2125, https://doi.org/10.5194/acp-11-2111-2011, 2011.

Barlow, J., Best, M., Bohnenstengel, S. I., Clark, P., Grimmond, S., Lean, H., Christen, A., Emeis, S., Haeffelin, M., Harman, I. N., Lemonsu, A., Martilli, A., Pardyjak, E., Rotach, M. W., Ballard, S., Boutle, I., Brown, A., Cai, X., Carpentieri, M., Coceal, O., Crawford, B., Di Sabatino, S., Dou, J., Drew, D. R., Edwards, J. M., Fallmann, J., Fortuniak, K., Gornall, J., Gronemeier, T., Halios, C. H., Hertwig, D., Hirano, K., Holtslag, A. A. M., Luo, Z., Mills, G., Nakayoshi, M., Pain, K., Schlünzen, K. H., Smith, S., Soulhac, L., Steeneveld, G.-J., Sun, T., Theeuwes, N. E., Thomson, D., Voogt, J. A., Ward, H. C., Xie, Z.-T., Zhong, J., Barlow, J., Best, M., Bohnenstengel, S. I., Clark, P., Grimmond, S., Lean, H., Christen, A., Emeis, S., Haeffelin, M., Harman, I. N., Lemonsu, A., Martilli, A., Pardyjak, E., Rotach, M. W., Ballard, S., Boutle, I., Brown, A., Cai, X., Carpentieri, M., Coceal, O., Crawford, B., Sabatino, S. D., Dou, J., Drew, D. R., Edwards, J. M., Fallmann, J., Fortuniak, K., Gornall, J., Gronemeier, T., Halios, C. H., Hertwig, D., Hirano, K., Holtslag, A. A. M., Luo, Z., Mills, G., Nakayoshi, M., Pain, K., Schlünzen, K. H., Smith, S., Soulhac, L., Steeneveld, G.-J., Sun, T., Theeuwes, N. E., Thomson, D., Voogt, J. A., Ward, H. C., Xie, Z.-T., and Zhong, J.: Developing a Research Strategy to Better Understand, Observe, and Simulate Urban Atmospheric

Processes at Kilometer to Subkilometer Scales, Bull. Amer. Meteor. Soc., 98, ES261–ES264, https://doi.org/10.1175/BAMS-D-17-0106.1, 2017.

Barlow, J. F.: Progress in observing and modelling the urban boundary layer, Urban Climate, 10, 216–240, https://doi.org/10.1016/j.uclim.2014.03.011, 2014.

Barlow, J. F., Halios, C. H., Lane, S. E., and Wood, C. R.: Observations of urban boundary layer structure during a strong urban heat island event, Environmental Fluid Mechanics, 15, 373–398, https://doi.org/10.1007/s10652-014-9335-6, 2015.

Basha, G. and Ratnam, M. V.: Identification of atmospheric boundary layer height over a tropical station using high-resolution radiosonde refractivity profiles: Comparison with GPS radio occultation measurements, J. Geophys. Res. Atmos., 114, https://doi.org/10.1029/2008JD011692, 2009.

Behrendt, A., Wulfmeyer, V., Bauer, H.-S., Schaberl, T., Di Girolamo, P., Summa, D., Kiemle, C., Ehret, G., Whiteman, D. N., Demoz, B. B., Browell, E. V., Ismail, S., Ferrare, R., Kooi, S., and Wang, J.: Intercomparison of Water Vapor Data Measured with Lidar during IHOP_2002. Part I: Airborne to Ground-Based Lidar Systems and Comparisons with Chilled-Mirror Hygrometer Radiosondes, J. Atmos. Oceanic Technol., 24, 3–21, https://doi.org/10.1175/JTECH1924.1, 2007.

Behrendt, A., Wulfmeyer, V., Hammann, E., Muppa, S., and Pal, S.: Profiles of second-to fourth-order moments of turbulent temperature fluctuations in the convective boundary layer: first measurements with rotational Raman lidar, Atmos. Chem. Phys., 15, 5485–5500, https://doi.org/10.5194/acp-15-5485-2015, 2015.

Behrendt, A., Wulfmeyer, V., Senff, C., Kumar Muppa, S., Späth, F., Lange, D., Kalthoff, N., and Wieser, A.: Observation of sensible and latent heat flux profiles with lidar, Atmos. Meas. Tech., 13, 3221–3233, https://doi.org/10.5194/AMT-13-3221-2020, 2020.

Bennett, L. J., Weckwerth, T. M., Blyth, A. M., Geerts, B., Miao, Q., and Richardson, Y. P.: Observations of the evolution of the nocturnal and convective boundary layers and the structure of open-celled convection on 14 June 2002, Mon. Wea. Rev., 138, 2589–2607, https://doi.org/10.1175/2010MWR3200.1, 2010.

Berg, L. K., Newsom, R. K., and Turner, D. D.: Year-Long Vertical Velocity Statistics Derived from Doppler Lidar Data for the Continental Convective Boundary Layer, J. Appl. Meteor. Climatol., 56, 2441–2454, https://doi.org/10.1175/JAMC-D-16-0359.1, 2017.

Berkes, F., Neis, P., Schultz, M. G., Bundke, U., Rohs, S., Smit, H. G., Wahner, A., Konopka, P., Boulanger, D., Nédélec, P., Thouret, V., and Petzold, A.: In situ temperature measurements in the upper troposphere and lowermost stratosphere from 2 decades of IAGOS long-term routine observation, Atmos. Chem. Phys., 17, 12 495–12 508, https://doi.org/10.5194/acp-17-12495-2017, 2017.

Beyrich, F.: Mixing height estimation from sodar data — A critical discussion, Atmos. Environ., 31, 3941–3953, https://doi.org/10.1016/S1352-2310(97)00231-8, 1997.

Beyrich, F. and Leps, J. P.: An operational mixing height data set from routine radiosoundings at Lindenberg: Methodology, Meteor. Z., https://doi.org/10.1127/0941-2948/2012/0333, 2012.

Bian, J., Chen, H., Vömel, H., Duan, Y., Xuan, Y., and Lü, D.: Intercomparison of humidity and temperature sensors: GTS1, Vaisala RS80, and CFH, Advances in Atmospheric Sciences, 28, 139–146, https://doi.org/10.1007/s00376-010-9170-8, 2011.

Bianco, L. and Wilczak, J. M.: Convective Boundary Layer Depth: Improved Measurement by Doppler Radar Wind Profiler Using Fuzzy Logic Methods, J. Atmos. Oceanic Technol., 19, 1745–1758, https://doi.org/10.1175/1520-0426(2002)019<1745:CBLDIM>2.0.CO;2, 2002.

Bianco, L., Wilczak, J. M., and White, A. B.: Convective Boundary Layer Depth Estimation from Wind Profilers: Statistical Comparison between an Automated Algorithm and Expert Estimations, J. Atmos. Oceanic Technol., 25, 1397–1413, https://doi.org/10.1175/2008JTECHA981.1, 2008.

Bianco, L., Djalalova, I. V., King, C. W., and Wilczak, J. M.: Diurnal Evolution and Annual Variability of Boundary-Layer Height and Its Correlation to Other Meteorological Variables in California's Central Valley, Boundary-Layer Meteorol., 140, 491–511, https://doi.org/10.1007/s10546-011-9622-4, 2011.

Bianco, L., Friedrich, K., Wilczak, J. M., Hazen, D., Wolfe, D., Delgado, R., Oncley, S. P., and Lundquist, J. K.: Assessing the accuracy of microwave radiometers and radio acoustic sounding systems for wind energy applications, Atmos. Meas. Tech., 10, 1707–1721, https://doi.org/10.5194/amt-10-1707-2017, 2017.

Bianco, L., Muradyan, P., Djalalova, I., Wilczak, J. M., Olson, J. B., Kenyon, J. S., Kotamarthi, R., Lantz, K., Long, C., and Turner, D.: Comparison of Observations and Predictions of Daytime Planetary-Boundary-Layer Heights and Surface Meteorological Variables in the Columbia River Gorge and Basin During the Second Wind Forecast Improvement Project, Boundary-Layer Meteorol., https://doi.org/10.1007/s10546-021-00645-x, 2021.

Blumberg, W., Turner, D., Löhnert, U., and Castleberry, S.: Ground-based temperature and humidity profiling using spectral infrared and microwave observations. Part II: Actual retrieval performance in clear-sky and cloudy conditions, J. Appl. Meteor. Climatol., 54, 2305–2319, https://doi.org/10.1175/JAMC-D-15-0005.1, 2015.

Bodeker, G. E., Bojinski, S., Cimini, D., Dirksen, R. J., Haeffelin, M., Hannigan, J. W., Hurst, D. F., Leblanc, T., Madonna, F., Maturilli, M., Mikalsen, A. C., Philipona, R., Reale, T., Seidel, D. J., Tan, D. G. H., Thorne, P. W., Vömel, H., and Wang, J.: Reference Upper-Air Observations for Climate: From Concept to Reality, Bull. Amer. Meteor. Soc., 97, 123–135, https://doi.org/10.1175/BAMS-D-14-00072.1, 2016.

Bodini, N., Lundquist, J. K., and Newsom, R. K.: Estimation of turbulence dissipation rate and its variability from sonic anemometer and wind Doppler lidar during the XPIA field campaign, Atmos. Meas. Tech., 11, 4291–4308, https://doi.org/10.5194/amt-11-4291-2018, 2018.

Bonin, T. A., Newman, J. F., Klein, P. M., Chilson, P. B., and Wharton, S.: Improvement of vertical velocity statistics measured by a Doppler lidar through comparison with sonic anemometer observations, Atmos. Meas. Tech., 9, 5833–5852, https://doi.org/10.5194/amt-9-5833-2016, 2016.

Bonin, T. A., Choukulkar, A., Brewer, W. A., Sandberg, S. P., Weickmann, A. M., Pichugina, Y. L., Banta, R. M., Oncley, S. P., and Wolfe, D. E.: Evaluation of turbulence measurement techniques from a single Doppler lidar, Atmos. Meas. Tech., 10, 3021–3039, https://doi.org/10.5194/amt-10-3021-2017, 2017.

Bonin, T. A., Carroll, B. J., Hardesty, R. M., Brewer, W. A., Hajny, K., Salmon, O. E., and Shepson, P. B.: Doppler Lidar Observations of the Mixing Height in Indianapolis Using an Automated Composite Fuzzy Logic Approach, J. Atmos. Oceanic Technol., 35, 473–490, https://doi.org/10.1175/JTECH-D-17-0159.1, 2018.

Bosveld, F. C., Baas, P., Beljaars, A. C., Holtslag, A. A., de Arellano, J. V. G., and van de Wiel, B. J.: Fifty Years of Atmospheric Boundary-Layer Research at Cabauw Serving Weather, Air Quality and Climate, Boundary-Layer Meteorol., 177, 583–612, https://doi.org/10.1007/s10546-020-00541-w, 2020.

Boy, M., Thomson, E. S., Navarro, J. C., Arnalds, O., Batchvarova, E., Bäck, J., Berninger, F., Bilde, M., Dagsson-Waldhauserova, P., Castarède, D., Dalirian, M., De Leeuw, G., Dragosics, M., Duplissy, E. M., Duplissy, J., Ekman, A. M., Fang, K., Gallet, J. C., Glasius, M., Gryning, S. E., Grythe, H., Hansson, H. C., Hansson, M., Isaksson, E., Iversen, T., Jonsdottir, I., Kasurinen, V., Kirkevåg, A., Korhola, A., Krejci, R., Egill Kristjansson, J., Lappalainen, H. K., Lauri, A., Leppäranta, M., Lihavainen, H., Makkonen, R., Massling, A., Meinander, O., Douglas Nilsson, E., Olafsson, H., Pettersson, J. B., Prisle, N. L., Riipinen, I., Roldin, P., Ruppel, M., Salter, M., Sand, M., Seland, O., Seppä, H., Skov, H., Soares, J., Stohl, A., Ström, J., Svensson, J., Swietlicki, E., Tabakova, K., Thorsteinsson, T., Virkkula, A., Weyhenmeyer, G. A., Wu, Y., Zieger, P., and Kulmala, M.: Interactions between the atmosphere, cryosphere, and ecosystems at northern high latitudes, https://doi.org/10.5194/acp-19-2015-2019, 2019.

Bradley, R. S., Keimig, F. T., and Diaz, H. F.: Recent changes in the North American Arctic boundary layer in winter, J. Geophys. Res. Atmos., 98, 8851–8858, https://doi.org/10.1029/93JD00311, 1993.

Bradley, S.: Atmospheric Acoustic Remote Sensing, Boca Raton: CRC Press., 2007.

Bravo-Aranda, J. A., Titos, G., Granados-Muñoz, M. J., Guerrero-Rascado, J. L., Navas-Guzmán, F., Valenzuela, A., Lyamani, H., Olmo, F. J., Andrey, J., and Alados-Arboledas, L.: Study of mineral dust entrainment in the planetary boundary layer by lidar depolarisation technique, Tellus B: Chemical and Physical Meteorology, 67, 26 180, https://doi.org/10.3402/tellusb.v67.26180, 2015.

Bravo-Aranda, J. A., de Arruda Moreira, G., Navas-Guzmán, F., Granados-Muñoz, M. J., Guerrero-Rascado, J. L., Pozo-Vázquez, D., Arbizu-Barrena, C., Olmo Reyes, F. J., Mallet, M., and Alados Arboledas, L.: A new methodology for PBL height estimations based on lidar depolarization measurements: analysis and comparison against MWR and WRF model-based results, Atmos. Chem. Phys., 17, 6839–6851, https://doi.org/10.5194/acp-17-6839-2017, 2017.

Cadeddu, M. P., Liljegren, J. C., and Turner, D. D.: The Atmospheric radiation measurement (ARM) program network of microwave radiometers: instrumentation, data, and retrievals, Atmos. Meas. Tech., 6, 2359–2372, https://doi.org/10.5194/amt-6-2359-2013, 2013.

Caicedo, V., Rappenglück, B., Lefer, B., Morris, G., Toledo, D., and Delgado, R.: Comparison of aerosol lidar retrieval methods for boundary layer height detection using ceilometer aerosol backscatter data, Atmos. Meas. Tech., 10, 1609–1622, https://doi.org/10.5194/amt-10-1609-2017, 2017.

Caicedo, V., Rappenglueck, B., Cuchiara, G., Flynn, J., Ferrare, R., Scarino, A. J., Berkoff, T., Senff, C., Langford, A., and Lefer, B.: Bay Breeze and Sea Breeze Circulation Impacts on the Planetary Boundary Layer and Air Quality From an Observed and Modeled DISCOVER-AQ Texas Case Study, J. Geophys. Res. Atmos., 124, 7359–7378, https://doi.org/10.1029/2019JD030523, 2019.

Caicedo, V., Delgado, R., Sakai, R., Knepp, T., Williams, D., Cavender, K., Lefer, B., and Szykman, J.: An Automated Common Algorithm for Planetary Boundary Layer Retrievals Using Aerosol Lidars in Support of the U.S. EPA Photochemical Assessment Monitoring Stations Program, J. Atmos. Oceanic Technol., 37, 1847–1864, https://doi.org/10.1175/JTECH-D-20-0050.1, 2020.

Canny, J.: A Computational Approach to Edge Detection, IEEE Transactions on Pattern Analysis and Machine Intelligence, PAMI-8, 679–698, https://doi.org/10.1109/TPAMI.1986.4767851, 1986.

Caumont, O., Cimini, D., Löhnert, U., Alados-Arboledas, L., Bleisch, R., Buffa, F., Ferrario, M. E., Haefele, A., Huet, T., Madonna, F., and Pace, G.: Assimilation of humidity and temperature observations retrieved from ground-based microwave radiometers into a convective-scale NWP model, Quart. J. Roy. Meteor. Soc., 142, 2692–2704, https://doi.org/10.1002/qj.2860, 2016.

Chan, K. M. and Wood, R.: The seasonal cycle of planetary boundary layer depth determined using COSMIC radio occultation data, J. Geophys. Res., 118, 422–434, https://doi.org/10.1002/2013JD020147, 2013.

Chen, X., Añel, J. A., Su, Z., de la Torre, L., Kelder, H., van Peet, J., and Ma, Y.: The Deep Atmospheric Boundary Layer and Its Significance to the Stratosphere and Troposphere Exchange over the Tibetan Plateau, PLoS ONE, https://doi.org/10.1371/journal.pone.0056909, 2013.

Chen, X., Skerlak, B., Rotach, M. W., Añel, J. A., Su, Z., Ma, Y., and Maoshan, L.: Reasons for the Extremely High-Ranging Planetary Boundary Layer over the Western Tibetan Plateau in Winter, J. Atmos. Sci., 73, 2021–2038, https://doi.org/10.1175/JAS-D-15-0148.1, 2016.

Chu, Y., Li, J., Li, C., Tan, W., Su, T., and Li, J.: Seasonal and diurnal variability of planetary boundary layer height in Beijing: Intercomparison between MPL and WRF results, Atmos. Res., 227, 1–13, https://doi.org/10.1016/j.atmosres.2019.04.017, 2019.

Cimini, D., Hewison, T. J., Martin, L., Güldner, J., Gaffard, C., and Marzano, F. S.: Temperature and humidity profile retrievals from ground-based microwave radiometers during TUC, Meteor. Z., 15, 45–56, https://doi.org/10.1127/0941-2948/2006/0099, 2006.

Cimini, D., Campos, E., Ware, R., Albers, S., Giuliani, G., Oreamuno, J., Joe, P., Koch, S. E., Cober, S., and Westwater, E.: Thermodynamic Atmospheric Profiling During the 2010 Winter Olympics Using Ground-Based Microwave Radiometry, IEEE Trans. Geosci. Remote Sens., 49, 4959–4969, https://doi.org/10.1109/TGRS.2011.2154337, 2011.

Cimini, D., De Angelis, F., Dupont, J.-C., Pal, S., and Haeffelin, M.: Mixing layer height retrievals by multichannel microwave radiometer observations, Atmos. Meas. Tech., 6, 2941–2951, https://doi.org/10.5194/amt-6-2941-2013, 2013.

Cimini, D., Nelson, M., Güldner, J., and Ware, R.: Forecast indices from a ground-based microwave radiometer for operational meteorology, Atmos. Meas. Tech., 8, 315–333, https://doi.org/10.5194/amt-8-315-2015, 2015.

Cimini, D., Haeffelin, M., Kotthaus, S., Löhnert, U., Martinet, P., O'Connor, E., Walden, C., Collaud Coen, M., and Preissler, J.: Towards the profiling of the atmospheric boundary layer at European scale — introducing the COST Action PROBE, Bulletin of Atmospheric Science and Technology, pp. 23–42, https://doi.org/10.1007/s42865-020-00003-8, 2020.

CIMO-TECO, W., ed.: GCOS Upper Air Network (GUAN) Radiosonde Observations Past, Present and Future, O3, https://www.wmo.int/pages/prog/www/IMOP/documents/O3_3_Oakley_ExtendedAbstract.pdf, 2018.

Cohen, A. E., Cavallo, S. M., Coniglio, M. C., and Brooks, H. E.: A Review of Planetary Boundary Layer Parameterization Schemes and Their Sensitivity in Simulating Southeastern U.S. Cold Season Severe Weather Environments, Wea. Forecasting, 30, 591–612, https://doi.org/10.1175/WAF-D-14-00105.1, 2015.

Cohn, S. A.: Radar measurements of turbulent eddy dissipation rate in the troposphere: A comparison of techniques, J. Atmos. Oceanic Technol., 12, 85–95, https://doi.org/10.1175/1520-0426(1995)012<0085:RMOTED>2.0.CO;2, 1995.

Cohn, S. A. and Angevine, W. M.: Boundary layer height and entrainment zone thickness measured by lidars and wind-profiling radars, J. Appl. Meteor., 39, 1233–1247, https://doi.org/10.1175/1520-0450(2000)039<1233:BLHAEZ>2.0.CO;2, 2000.

Collaud Coen, M., Praz, C., Haefele, A., Ruffieux, D., Kaufmann, P., and Calpini, B.: Determination and climatology of the planetary boundary layer height above the Swiss plateau by in situ and remote sensing measurements as well as by the COSMO-2 model, Atmos. Chem. Phys., 14, 13 205–13 221, https://doi.org/10.5194/acp-14-13205-2014, 2014.

Collaud Coen, M., Andrews, E., Aliaga, D., Andrade, M., Angelov, H., Bukowiecki, N., Ealo, M., Fialho, P., Flentje, H., Hallar, A. G., Hooda, R., Kalapov, I., Krejci, R., Lin, N.-H., Marinoni, A., Ming, J., Nguyen, N. A., Pandolfi, M., Pont, V., Ries, L., Rodríguez, S., Schauer, G., Sellegri, K., Sharma, S., Sun, J., Tunved, P., Velasquez, P., and Ruffieux, D.: Identification of topographic features influencing aerosol observations at high altitude stations, Atmos. Chem. Phys., 18, 12 289–12 313, https://doi.org/10.5194/acp-18-12289-2018, 2018.

Compton, J. C., Delgado, R., Berkoff, T. A., Hoff, R. M., Compton, J. C., Delgado, R., Berkoff, T. A., and Hoff, R. M.: Determination of Planetary Boundary Layer Height on Short Spatial and Temporal Scales: A Demonstration of the Covariance Wavelet Transform in Ground-Based Wind Profiler and Lidar Measurements, J. Atmos. Oceanic Technol., 30, 1566–1575, https://doi.org/10.1175/JTECH-D-12-00116.1, 2013.

Dang, R., Yang, Y., Hu, X.-M., Wang, Z., and Zhang, S.: A Review of Techniques for Diagnosing the Atmospheric Boundary Layer Height (ABLH) Using Aerosol Lidar Data, Remote. Sens., 11, 1590, https://doi.org/10.3390/rs11131590, 2019.

Darand, M. and Zandkarimi, F.: Identification of atmospheric boundary layer height and trends over Iran using high-resolution ECMWF reanalysis dataset, Theoretical and Applied Climatology, 137, 1457–1465, https://doi.org/10.1007/s00704-018-2691-2, 2019.

Davy, R.: The Climatology of the Atmospheric Boundary Layer in Contemporary Global Climate Models, J. Climate, 31, 9151–9173, https://doi.org/10.1175/JCLI-D-17-0498.1, 2018.

de Arruda Moreira, G., Guerrero-Rascado, J., Bravo-Aranda, J., Benavent-Oltra, J., Ortiz-Amezcua, P., Róman, R., Bedoya-Velásquez, A., Landulfo, E., and Alados-Arboledas, L.: Study of the planetary boundary layer by microwave radiometer, elastic lidar and Doppler lidar estimations in Southern Iberian Peninsula, Atmos. Res., 213, 185–195, https://doi.org/10.1016/j.atmosres.2018.06.007, 2018.

de Arruda Moreira, G., Guerrero-Rascado, J. L., Benavent-Oltra, J. A., Ortiz-Amezcua, P., Román, R., E. Bedoya-Velásquez, A., Bravo-Aranda, J. A., Olmo Reyes, F. J., Landulfo, E., and Alados-Arboledas, L.: Analyzing the turbulent planetary boundary layer by remote sensing systems: the Doppler wind lidar, aerosol elastic lidar and microwave radiometer, Atmos. Chem. Phys., 19, 1263–1280, https://doi.org/10.5194/acp-19-1263-2019, 2019.

de Arruda Moreira, G., Guerrero-Rascado, J. L., Bravo-Aranda, J. A., Foyo-Moreno, I., Cazorla, A., Alados, I., Lyamani, H., Landulfo, E., and Alados-Arboledas, L.: Study of the planetary boundary layer height in an urban environment using a combination of microwave radiometer and ceilometer, Atmos. Res., p. 104932, https://doi.org/10.1016/j.atmosres.2020.104932, 2020.

de Arruda Moreira, G., Sánchez-Hernández, G., Guerrero-Rascado, J. L., Cazorla, A., and Alados-Arboledas, L.: Estimating the urban atmospheric boundary layer height from remote sensing applying machine learning techniques, Atmos. Res., p. 105962, 2022.

de Bruine, M., Apituley, A., Donovan, D., Klein Baltink, H., and de Haij, M.: Pathfinder: Applying graph theory to consistent tracking of daytime mixed layer height with backscatter lidar, Atmos. Meas. Tech., pp. 1893–1909, https://doi.org/10.5194/amt-10-1893-2017, 2017.

de Haij, M., Wauben, W., and Klein Baltink, H.: Determination of mixing layer height from ceilometer backscatter profiles, Remote. Sens., pp. 63 620R–63 620R–12, 2006.

De Wekker, S. F. J. and Kossmann, M.: Convective Boundary Layer Heights Over Mountainous Terrain—A Review of Concepts, Frontiers in Earth Science, 3, 77, https://doi.org/10.3389/feart.2015.00077, 2015.

Di Girolamo, P., De Rosa, B., Flamant, C., Summa, D., Bousquet, O., Chazette, P., Totems, J., and Cacciani, M.: Water vapor mixing ratio and temperature inter-comparison results in the framework of the Hydrological Cycle in the Mediterranean Experiment—Special Observation Period 1, Bulletin of Atmospheric Science and Technology, 1, 113–153, https://doi.org/10.1007/s42865-020-00008-3, 2020.

Di Giuseppe, F., Riccio, A., Caporaso, L., Bonafé, G., Gobbi, G. P., and Angelini, F.: Automatic detection of atmospheric boundary layer height using ceilometer backscatter data assisted by a boundary layer model, Quart. J. Roy. Meteor. Soc., 138, 649–663, https://doi.org/10.1002/qj.964, 2012.

Diaz, J. P., Exposito, F. J., Pérez, J. C., and Gonzalez, A.: Long-Term Trends in Marine Boundary Layer Properties over the Atlantic Ocean, J. Climate, 32, 2991–3004, https://doi.org/10.1175/JCLI-D-18-0219.1, 2019.

Diémoz, H., Paolo Gobbi, G., Magri, T., Pession, G., Pittavino, S., Tombolato, I. K., Campanelli, M., and Barnaba, F.: Transport of Po Valley aerosol pollution to the northwestern Alps-Part 2: Long-term impact on air quality, Atmos. Chem. Phys., 19, 10 129–10 160, https://doi.org/10.5194/acp-19-10129-2019, 2019.

Dirksen, R. J., Sommer, M., Immler, F. J., Hurst, D. F., Kivi, R., and Vömel, H.: Reference quality upper-air measurements: GRUAN data processing for the Vaisala RS92 radiosonde, Atmos. Meas. Tech., 7, 4463–4490, https://doi.org/10.5194/amt-7-4463-2014, 2014.

Djalalova, I. V., Turner, D. D., Bianco, L., Wilczak, J. M., Duncan, J., Adler, B., and Gottas, D.: Improving thermodynamic profile retrievals from microwave radiometers by including Radio Acoustic Sounding System (RASS) observations, Atmos. Meas. Tech. Disc., 2021, 1–50, https://doi.org/10.5194/amt-2021-9, 2021.

Duncan Jr., J. B., Bianco, L., Adler, B., Bell, T., Djalalova, I. V., Riihimaki, L., Sedlar, J., Smith, E. N., Turner, D. D., Wagner, T. J., and Wilczak, J. M.: Evaluating daytime planetary boundary-layer height estimations resolved by both active and passive remote sensing instruments during the CHEESEHEAD19 field campaign, Atmos. Meas. Tech. Disc., 2021, 1–40, https://doi.org/10.5194/amt-2021-363, 2021.

Eberhard, W. L., Cupp, R. E., and Healy, K. R.: Doppler Lidar Measurement of Profiles of Turbulence and Momentum Flux, J. Atmos. Oceanic Technol., 6, 809–819, https://doi.org/https://doi.org/10.1175/1520-0426(1989)006<0809:DLMOPO>2.0.CO;2, 1989.

Ecklund, W. L., Carter, D. A., and Balsley, B. B.: A UHF wind profiler for the boundary layer: Brief description and initial results, J. Atmos. Oceanic Technol., 5, 432–441, https://doi.org/10.1175/1520-0426(1988)005<0432:AUWPFT>2.0.CO;2, 1988.

Elie Quentin Bessardon, G., Fosu-Amankwah, K., Petersson, A., and Jane Brooks, B.: Evaluation of Windsond S1H2 performance in Kumasi during the 2016 DACCIWA field campaign, Atmos. Meas. Tech., 12, 1311–1324, https://doi.org/10.5194/AMT-12-1311-2019, 2019.

Emeis, S.: Surface-based remote sensing of the atmospheric boundary layer, vol. 40, Springer Science & Business Media, 2010.

Emeis, S., Schäfer, K., and Münkel, C.: Surface-based remote sensing of the mixing-layer height - A review, Meteor. Z., 17, 621–630, https://doi.org/10.1127/0941-2948/2008/0312, 2008.

Emeis, S., Schäfer, K., and Münkel, C.: Observation of the structure of the urban boundary layer with different ceilometers and validation by RASS data, Meteor. Z., 18, 149–154, https://doi.org/10.1127/0941-2948/2009/0365, 2009.

Engelbart, D. A. M. and Bange, J.: Determination of boundary-layer parameters using wind profiler/RASS and sodar/RASS in the frame of the LITFASS project, Theoretical and Applied Climatology, 73, 53–65, https://doi.org/10.1007/s00704-002-0693-5, 2002.

Eresmaa, N., Karppinen, A., Joffre, S., Räsänen, J., and Talvitie, H.: Mixing height determination by ceilometer, Atmos. Chem. Phys., 6, 1485–1493, https://doi.org/10.5194/acp-6-1485-2006, 2006.

Eresmaa, N., Härkönen, J., Joffre, S. M., Schultz, D. M., Karppinen, A., and Kukkonen, J.: A three-step method for estimating the mixing height using ceilometer data from the Helsinki testbed, J. Appl. Meteor. Climatol., 51, 2172–2187, https://doi.org/10.1175/JAMC-D-12-058.1, 2012.

Feltz, W. F. and Mecikalski, J. R.: Monitoring high-temporal-resolution convective stability indices using the ground-based Atmospheric Emitted Radiance Interferometer (AERI) during the 3 May 1999 Oklahoma–Kansas tornado outbreak, Wea. Forecasting, 17, 445–455, https://doi.org/10.1175/1520-0434(2002)017<0445:MHTRCS>2.0.CO;2, 2002.

Feltz, W. F., Smith, W. L., Howell, H. B., Knuteson, R. O., Woolf, H., and Revercomb, H. E.: Near-Continuous Profiling of Temperature, Moisture, and Atmospheric Stability Using the Atmospheric Emitted Radiance Interferometer (AERI), J. Appl. Meteor., 42, 584 – 597, https://doi.org/10.1175/1520-0450(2003)042<0584:NPOTMA>2.0.CO;2, 2003.

Finnigan, J.: Boundary layers | Complex Terrain, in: Encyclopedia of Atmospheric Sciences, edited by Holton, J. R., pp. 234 – 244, Academic Press, Oxford, https://doi.org/10.1016/B0-12-227090-8/00084-1, 2003.

Finnigan, J. J., Einaudi, F., and Fua, D.: The interaction between an internal gravity wave and turbulence in the stably-stratified nocturnal boundary layer., J. Atmos. Sci., 41, 2409–2436, https://doi.org/10.1175/1520-0469(1984)041<2409:TIBAIG>2.0.CO;2, 1984.

Flamant, P., Cuesta, J., Denneulin, M.-L., Dabas, A., and Huber, D.: ADM-Aeolus retrieval algorithms for aerosol and cloud products, Tellus A: Dynamic Meteorology and Oceanography, 60 A, 273–288, https://doi.org/10.1111/J.1600-0870.2007.00287.X, 2016.

Fochesatto, G. J., Drobinski, P., Flamant, C., Guedalia, D., Sarrat, C., Flamant, P. H., and Pelon, J.: Evidence of dynamical coupling between the residual layer and the developing convective boundary layer, Boundary-Layer Meteorol., 99, 451–464, https://doi.org/10.1023/A:1018935129006, 2001.

Frehlich, R., Meillier, Y., Jensen, M. L., Balsley, B., and Sharman, R.: Measurements of Boundary Layer Profiles in an Urban Environment, J. Appl. Meteor. Climatol., 45, 821–837, https://doi.org/10.1175/JAM2368.1, 2006.

Frehlich, R., Meillier, Y., and Jensen, M. L.: Measurements of Boundary Layer Profiles with In Situ Sensors and Doppler Lidar, J. Atmos. Oceanic Technol., 25, 1328–1340, https://doi.org/10.1175/2007JTECHA963.1, 2008.

Freudenthaler, V., Linné, H., Chaikovski, A., Rabus, D., and Groß, S.: EARLINET lidar quality assurance tools, Atmos. Meas. Tech. Disc., 2018, 1–35, https://doi.org/10.5194/amt-2017-395, 2018.

Fromm, M., Lindsey, D. T., Servranckx, R., Yue, G., Trickl, T., Sica, R., Doucet, P., and Godin-Beekmann, S.: The Untold Story of Pyrocumulonimbus, Bull. Amer. Meteor. Soc., 91, 1193–1210, https://doi.org/10.1175/2010BAMS3004.1, 2010.

Gan, C. M., Wu, Y., Gross, B., and Moshary, F.: Statistical comparison between Hysplit sounding and lidar observation of planetary boundary layer characteristics over New York City, in: Laser Radar Technology and Applications XV, edited by Turner, M. D. and Kamerman, G. W., vol. 7684, p. 76841K, International Society for Optics and Photonics, https://doi.org/10.1117/12.849705, 2010.

Gan, C.-M., Wu, Y., Madhavan, B., Gross, B., and Moshary, F.: Application of active optical sensors to probe the vertical structure of the urban boundary layer and assess anomalies in air quality model PM2.5 forecasts, Atmos. Environ., 45, 6613 – 6621, https://doi.org/10.1016/j.atmosenv.2011.09.013, 2011.

Garratt, J.: Review: the atmospheric boundary layer, Earth-Science Reviews, 37, 89–134, https://doi.org/10.1016/0012-8252(94)90026-4, 1994.

Geiß, A.: Automated calibration of ceilometer data and its applicability for quantitative aerosol monitoring, Ph.D. thesis, LMU München, https://edoc.ub.uni-muenchen.de/19930/1/Geiss{_}Alexander.pdf, 2016.

Geiß, A., Wiegner, M., Bonn, B., Schäfer, K., Forkel, R., von Schneidemesser, E., Münkel, C., Chan, K. L., and Nothard, R.: Mixing layer height as an indicator for urban air quality?, Atmos. Meas. Tech., 10, 2969–2988, https://doi.org/10.5194/amt-10-2969-2017, 2017.

Genthon, C., Six, D., Gallée, H., Grigioni, P., and Pellegrini, A.: Two years of atmospheric boundary layer observations on a 45-m tower at Dome C on the Antarctic plateau, J. Geophys. Res. Atmos., 118, 3218–3232, https://doi.org/10.1002/jgrd.50128, 2013.

Gibert, F., Cuesta, J., Yano, J.-I., Arnault, N., and Flamant, P. H.: On the Correlation between Convective Plume Updrafts and Downdrafts, Lidar Reflectivity and Depolarization Ratio, Boundary-Layer Meteorol., 125, 553–573, https://doi.org/10.1007/s10546-007-9205-6, 2007.

Gibert, F., Xuéref-Rémy, I., Joly, L., Schmidt, M., Cuesta, J., Davis, K. J., Ramonet, M., Flamant, P. H., Parvitte, B., and Zéninari, V.: A Case Study of CO2, CO and Particles Content Evolution in the Suburban Atmospheric Boundary Layer Using a 2-μm Doppler DIAL, a 1-μm Backscatter Lidar and an Array of In-situ Sensors, Boundary-Layer Meteorol., 128, 381–401, https://doi.org/10.1007/s10546-008-9296-8, 2008.

Gierens, R. T., Henriksson, S., Josipovic, M., Vakkari, V., van Zyl, P. G., Beukes, J. P., Wood, C. R., and O'Connor, E. J.: Observing continental boundary-layer structure and evolution over the South African savannah using a ceilometer, Theoretical and Applied Climatology, pp. 1–14, https://doi.org/10.1007/s00704-018-2484-7, 2018.

Görsdorf, U. and Lehmann, V.: Enhanced Accuracy of RASS-Measured Temperatures Due to an Improved Range Correction, J. Atmos. Oceanic Technol., 17, 406–416, https://doi.org/10.1175/1520-0426(2000)017<0406:EAORMT>2.0.CO;2, 2000.

Gottschall, J., Courtney, M. S., Wagner, R., Jørgensen, H. E., and Antoniou, I.: Lidar profilers in the context of wind energy - a verification procedure for traceable measurements, Wind Energy, 15, 147–159, https://doi.org/10.1002/we.518, 2012.

Granados-Muñoz, M., Navas-Guzmán, F., Bravo-Aranda, J., Guerrero-Rascado, J., Lyamani, H., Fernández-Gálvez, J., and Alados-Arboledas, L.: Automatic determination of the planetary boundary layer height using Lidar: One-year analysis over southeastern Spain, J. Geophys. Res. Atmos., 117, https://doi.org/10.1029/2012JD017524, 2012.

Griffiths, A., Parkes, S., Chambers, S., McCabe, M., and Williams, A.: Improved mixing height monitoring through a combination of lidar and radon measurements, Atmos. Meas. Tech., 6, 207–218, https://doi.org/10.5194/amt-6-207-2013, 2013.

Grund, C. J., Banta, R. M., George, J. L., Howell, J. N., Post, M. J., Richter, R. A., and Weickmann, A. M.: High-Resolution Doppler Lidar for Boundary Layer and Cloud Research, J. Atmos. Oceanic Technol., 18, 376–393, https://doi.org/10.1175/1520-0426(2001)018<0376:HRDLFB>2.0.CO;2, 2001.

Gryning, S.-E. and Batchvarova, E.: Parametrization of the depth of the entrainment zone above the daytime mixed layer, Quart. J. Roy. Meteor. Soc., 120, 47–58, https://doi.org/10.1002/qj.49712051505, 1994.

Guerrero-Rascado, J. L., Olmo, F. J., Avilés-Rodríguez, I., Navas-Guzmán, F., Pérez-Ramírez, D., Lyamani, H., and Arboledas, L. A.: Extreme saharan dust event over the southern Iberian peninsula in September 2007: Active and passive remote sensing from surface and satellite, Atmos. Chem. Phys., 9, 8453–8469, https://doi.org/10.5194/ACP-9-8453-2009, 2009.

Guimarães, Ye, Batista, Barbosa, Ribeiro, Medeiros, Souza, and Martin: Vertical Profiles of Ozone Concentration Collected by an Unmanned Aerial Vehicle and the Mixing of the Nighttime Boundary Layer over an Amazonian Urban Area, Atmosphere, 10, 599, https://doi.org/10.3390/atmos10100599, 2019.

Güldner, J.: A model-based approach to adjust microwave observations for operational applications: results of a campaign at Munich Airport in winter 2011/2012, Atmos. Meas. Tech., 6, 2879–2891, https://doi.org/10.5194/amt-6-2879-2013, 2013.

Guo, J., Miao, Y., Zhang, Y., Liu, H., Li, Z., Zhang, W., He, J., Lou, M., Yan, Y., Bian, L., and Zhai, P.: The climatology of planetary boundary layer height in China derived from radiosonde and reanalysis data, Atmos. Chem. Phys., 16, 13 309–13 319, https://doi.org/10.5194/acp-16-13309-2016, 2016.

Guo, J., Li, Y., Cohen, J. B., Li, J., Chen, D., Xu, H., Liu, L., Yin, J., Hu, K., and Zhai, P.: Shift in the temporal trend of boundary layer height in China using long-term (1979–2016) radiosonde data, Geophys. Res. Lett., 46, 6080–6089, https://doi.org/10.1029/2019GL082666, 2019.

Haeffelin, M., Angelini, F., Morille, Y., Martucci, G., Frey, S., Gobbi, G., Lolli, S., O'dowd, C., Sauvage, L., Xueref-Rémy, I., et al.: Evaluation of mixing-height retrievals from automatic profiling lidars and ceilometers in view of future integrated networks in Europe, Boundary-Layer Meteorol., 143, 49–75, https://doi.org/10.1007/s10546-011-9643-z, 2012.

Haid, M., Gohm, A., Umek, L., Ward, H. C., Muschinski, T., Lehner, L., and Rotach, M. W.: Foehn–cold pool interactions in the Inn Valley during PIANO IOP2, Quart. J. Roy. Meteor. Soc., 146, 1232–1263, https://doi.org/10.1002/qj.3735, 2020.

Halios, C. H. and Barlow, J. F.: Observations of the Morning Development of the Urban Boundary Layer Over London, UK, Taken During the ACTUAL Project, Boundary-Layer Meteorol., pp. 1–28, https://doi.org/10.1007/s10546-017-0300-z, 2017.

Haman, C. L., Lefer, B., Morris, G. A., Haman, C. L., Lefer, B., and Morris, G. A.: Seasonal Variability in the Diurnal Evolution of the Boundary Layer in a Near-Coastal Urban Environment, J. Atmos. Oceanic Technol., 29, 697–710, https://doi.org/10.1175/JTECH-D-11-00114.1, 2012.

Han, S., Bian, H., Tie, X., Xie, Y., Sun, M., and Liu, A.: Impact of nocturnal planetary boundary layer on urban air pollutants: Measurements from a 250-m tower over Tianjin, China, Journal of Hazardous Materials, 162, 264–269, https://doi.org/10.1016/J.JHAZMAT.2008.05.056, 2009.

Handorf, D., Foken, T., and Kottmeier, C.: The stable atmospheric boundary layer over an Antarctic ice Sheet, Boundary-Layer Meteorol., 91, 165–189, https://doi.org/10.1023/A:1001889423449, 1999.

Harvey, N. J., Hogan, R. J., and Dacre, H. F.: A method to diagnose boundary-layer type using Doppler lidar, Quart. J. Roy. Meteor. Soc., 139, 1681–1693, https://doi.org/10.1002/qj.2068, 2013.

Harvey, N. J., Hogan, R. J., and Dacre, H. F.: Evaluation of boundary-layer type in a weather forecast model utilizing long-term Doppler lidar observations, Quart. J. Roy. Meteor. Soc., 141, 1345–1353, https://doi.org/10.1002/qj.2444, 2015.

Heese, B., Flentje, H., Althausen, D., Ansmann, A., and Frey, S.: Ceilometer lidar comparison: backscatter coefficient retrieval and signal-to-noise ratio determination, Atmos. Meas. Tech., 3, 1763–1770, https://doi.org/10.5194/amt-3-1763-2010, 2010.

Helbig, M., Gerken, T., Beamesderfer, E. R., Baldocchi, D. D., Banerjee, T., Biraud, S. C., Brown, W. O., Brunsell, N. A., Burakowski, E. A., Burns, S. P., Butterworth, B. J., Chan, W. S., Davis, K. J., Desai, A. R., Fuentes, J. D., Hollinger, D. Y., Kljun, N., Mauder, M., Novick, K. A., Perkins, J. M., Rahn, D. A., Rey-Sanchez, C., Santanello, J. A., Scott, R. L., Seyednasrollah, B., Stoy, P. C., Sullivan, R. C., de Arellano, J. V.-G., Wharton, S., Yi, C., and Richardson, A. D.: Integrating continuous atmospheric boundary layer and tower-based flux measurements to advance understanding of land-atmosphere interactions, Agricultural and Forest Meteorology, 307, 108 509, https://doi.org/10.1016/J.AGRFORMET.2021.108509, 2021.

Helmis, C., Sgouros, G., Tombrou, M., Schäfer, K., Münkel, C., Bossioli, E., and Dandou, A.: A comparative study and evaluation of mixing-height estimation based on sodar-RASS, ceilometer data and numerical model simulations, Boundary-Layer Meteorol., pp. 1–20, https://doi.org/10.1007/s10546-012-9743-4, 2012.

Hennemuth, B. and Lammert, A.: Determination of the atmospheric boundary layer height from radiosonde and lidar backscatter, Boundary-Layer Meteorol., https://doi.org/10.1007/s10546-005-9035-3, 2006.

Herrera-Mejía, L. and Hoyos, C. D.: Characterization of the atmospheric boundary layer in a narrow tropical valley using remote-sensing and radiosonde observations and the WRF model: the Aburrá Valley case-study, Quart. J. Roy. Meteor. Soc., 145, 2641–2665, https://doi.org/https://doi.org/10.1002/qj.3583, 2019.

Hertwig, D., Grimmond, S., Kotthaus, S., Vanderwel, C., Gough, H., Haeffelin, M., and Robins, A.: Variability of physical meteorology in urban areas at different scales: Implications for air quality, Faraday Discussions, 226, 149–172, https://doi.org/10.1039/d0fd00098a, 2021.

Hervo, M., Poltera, Y., and Haefele, A.: An empirical method to correct for temperature dependent variations in the overlap function of CHM15k ceilometers, Atmos. Meas. Tech., 9, 2947–2959, https://doi.org/10.5194/amt-9-2947-2016, 2016.

Hirsikko, A., O'Connor, E. J., Komppula, M., Korhonen, K., Pfüller, A., Giannakaki, E., Wood, C. R., Bauer-Pfundstein, M., Poikonen, A., Karppinen, T., Lonka, H., Kurri, M., Heinonen, J., Moisseev, D., Asmi, E., Aaltonen, V., Nordbo, A., Rodriguez, E., Lihavainen, H., Laaksonen, A., Lehtinen, K. E. J., Laurila, T., Petäjä, T., Kulmala, M., and Viisanen, Y.: Observing wind, aerosol particles, cloud and precipitation: Finland's new ground-based remote-sensing network, Atmos. Meas. Tech., 7, 1351–1375, https://doi.org/10.5194/amt-7-1351-2014, 2014.

Ho, S.-p., Peng, L., Anthes, R. A., Kuo, Y.-H., and Lin, H.-C.: Marine Boundary Layer Heights and Their Longitudinal, Diurnal, and Interseasonal Variability in the Southeastern Pacific Using COSMIC, CALIOP, and Radiosonde Data, J. Climate, 28, 2856–2872, https://doi.org/10.1175/JCLI-D-14-00238.1, 2015.

Hogan, R. J., Grant, A. L., Illingworth, A. J., Pearson, G. N., and O'Connor, E. J.: Vertical velocity variance and skewness in clear and cloud-topped boundary layers as revealed by Doppler lidar, Quart. J. Roy. Meteor. Soc., 135, 635–643, https://doi.org/10.1002/qj.413, 2009.

Holtslag, A. and Nieuwstadt, F.: Scaling the atmospheric boundary layer, Boundary-Layer Meteorol., 36, 201–209, https://doi.org/10.1007/BF00117468, 1986.

Holzworth, G. C.: Estimates of mean maximum mixing depths in the contiguous United States, Mon. Wea. Rev., 92, 235–242, https://doi.org/10.1175/1520-0493(1964)092<0235:EOMMMD>2.3.CO;2, 1964.

Hooda, R. K., Kivekäs, N., O'Connor, E. J., Collaud Coen, M., Pietikäinen, J.-P., Vakkari, V., Backman, J., Henriksson, S. V., Asmi, E., Komppula, M., Korhonen, H., Hyvärinen, A.-P., and Lihavainen, H.: Driving Factors of Aerosol Properties Over the

Foothills of Central Himalayas Based on 8.5 Years Continuous Measurements, J. Geophys. Res. Atmos., 123, 13,421–13,442, https://doi.org/https://doi.org/10.1029/2018JD029744, 2018.

Hooper, W. P. and Eloranta, E. W.: Lidar measurements of wind in the planetary boundary layer: the method, accuracy and results from joint measurements with radiosonde and kytoon, J. Climate Appl. Meteor., 25, 990–1001, https://doi.org/10.1175/1520-0450(1986)025<0990:LMOWIT>2.0.CO;2, 1986.

Hopkin, E., Illingworth, A. J., Charlton-Perez, C., Westbrook, C. D., and Ballard, S.: A robust automated technique for operational calibration of ceilometers using the integrated backscatter from totally attenuated liquid clouds, Atmos. Meas. Tech., 12, 4131–4147, https://doi.org/10.5194/amt-12-4131-2019, 2019.

Hu, X. M., Klein, P. M., Xue, M., Lundquist, J. K., Zhang, F., and Qi, Y.: Impact of low-level jets on the nocturnal urban heat island intensity in Oklahoma city, J. Appl. Meteor. Climatol., 52, 1779–1802, https://doi.org/10.1175/JAMC-D-12-0256.1, 2013.

Huang, M., Gao, Z., Miao, S., Chen, F., LeMone, M. A., Li, J., Hu, F., and Wang, L.: Estimate of Boundary-Layer Depth Over Beijing, China, Using Doppler Lidar Data During SURF-2015, Boundary-Layer Meteorol., 162, 503–52, https://doi.org/10.1007/s10546-016-0205-2, 2017.

Huang, T., Yim, S. H. L., Yang, Y., Lee, O. S. M., Lam, D. H. Y., Cheng, J. C. H., and Guo, J.: Observation of turbulent mixing characteristics in the typical daytime cloud-topped boundary layer over Hong Kong in 2019, Remote. Sens., 12, 1533, https://doi.org/10.3390/RS12091533, 2020.

Hulin, M., Gheusi, F., Lothon, M., Pont, V., Lohou, F., Ramonet, M., Delmotte, M., Derrien, S., Athier, G., Meyerfeld, Y., Bezombes, Y., Augustin, P., and Ravetta, F.: Observations of Thermally Driven Circulations in the Pyrenees: Comparison of Detection Methods and Impact on Atmospheric Composition Measured at a Mountaintop, J. Appl. Meteor. Climatol., 58, 717–740, https://doi.org/10.1175/JAMC-D-17-0268.1, 2019.

Illingworth, A. J., Cimini, D., Gaffard, C., Haeffelin, M., Lehmann, V., Löhnert, U., O'Connor, E. J., and Ruffieux, D.: Exploiting existing ground-based remote sensing networks to improve high-resolution weather forecasts, Bull. Amer. Meteor. Soc., 96, 2107–2125, https://doi.org/10.1175/BAMS-D-13-00283.1, 2015.

Illingworth, A. J., Cimini, D., Haefele, A., Haeffelin, M., Hervo, M., Kotthaus, S., Löhnert, U., Martinet, P., Mattis, I., O'Connor, E., et al.: How Can Existing Ground-Based Profiling Instruments Improve European Weather Forecasts?, Bull. Amer. Meteor. Soc., 100, 605–619, https://doi.org/10.1175/BAMS-D-17-0231.1, 2019.

Johansson, C. and Bergström, H.: An auxiliary tool to determine the height of the boundary layer, Boundary-Layer Meteorol., 115, 423–432, https://doi.org/10.1007/s10546-004-1424-5, 2005.

Jordan, N. S., Hoff, R. M., and Bacmeister, J. T.: Validation of Goddard Earth Observing System-version 5 MERRA planetary boundary layer heights using CALIPSO, J. Geophys. Res. Atmos., 115, https://doi.org/10.1029/2009JD013777, 2010.

Kavaya, M. J. and Suni, P. J. M.: Continuous wave coherent laser radar: calculation of measurement location and volume, Appl. Opt., 30, 2634–2642, 1991.

Keller, C. A., Huwald, H., Vollmer, M. K., Wenger, A., Hill, M., Parlange, M. B., and Reimann, S.: Fiber optic distributed temperature sensing for the determination of the nocturnal atmospheric boundary layer height, Atmos. Meas. Tech., 4, 143–149, https://doi.org/10.5194/amt-4-143-2011, 2011.

Ketterer, C., Zieger, P., Bukowiecki, N., Collaud Coen, M., Maier, O., Ruffieux, D., and Weingartner, E.: Investigation of the Planetary Boundary Layer in the Swiss Alps Using Remote Sensing and In Situ Measurements, Boundary-Layer Meteorol., 151, 317–334, https://doi.org/10.1007/s10546-013-9897-8, 2014.

Klein, A., Ancellet, G., Ravetta, F., Thomas, J. L., and Pazmino, A.: Characterizing the seasonal cycle and vertical structure of ozone in Paris, France using four years of ground based LIDAR measurements in the lowermost troposphere, Atmos. Environ., 167, 603–615, https://doi.org/10.1016/J.ATMOSENV.2017.08.016, 2017.

Knepp, T. N., Szykman, J. J., Long, R., Duvall, R. M., Krug, J., Beaver, M., Cavender, K., Kronmiller, K., Wheeler, M., Delgado, R., et al.: Assessment of mixed-layer height estimation from single-wavelength ceilometer profiles, Atmos. Meas. Tech., 10, 3963, https://doi.org/10.5194/amt-2017-127, 2017.

Knuteson, R., Revercomb, H., Best, F., Ciganovich, N., Dedecker, R., Dirkx, T., Ellington, S., Feltz, W., Garcia, R., Howell, H., et al.: Atmospheric emitted radiance interferometer. Part I: Instrument design, J. Atmos. Oceanic Technol., 21, 1763–1776, https://doi.org/10.1175/JTECH-1662.1, 2004a.

Knuteson, R., Revercomb, H., Best, F., Ciganovich, N., Dedecker, R., Dirkx, T., Ellington, S., Feltz, W., Garcia, R., Howell, H., et al.: Atmospheric emitted radiance interferometer. Part II: Instrument performance, J. Atmos. Oceanic Technol., 21, 1777–1789, https://doi.org/10.1175/JTECH-1663.1, 2004b.

Koffi, E. N., Bergamaschi, P., Karstens, U., Krol, M., Segers, A., Schmidt, M., Levin, I., and Vermeulen, A. T.: Evaluation of the boundary layer dynamics of the TM5 model over Europe, Geosci. Model Dev., pp. 3137–3160, https://doi.org/10.5194/gmd-9-3137-2016, 2016.

Kokkalis, P., Alexiou, D., Papayannis, A., Rocadenbosch, F., Soupiona, O., Raptis, P. I., Mylonaki, M., Tzanis, C. G., and Christodoulakis, J.: Application and Testing of the Extended-Kalman-Filtering Technique for Determining the Planetary Boundary-Layer Height over Athens, Greece, Boundary-Layer Meteorol., 176, 125–147, https://doi.org/10.1007/s10546-020-00514-z, 2020.

Korhonen, K., Giannakaki, E., Mielonen, T., Pfüller, A., Laakso, L., Vakkari, V., Baars, H., Engelmann, R., Beukes, J. P., Van Zyl, P. G., Ramandh, A., Ntsangwane, L., Josipovic, M., Tiitta, P., Fourie, G., Ngwana, I., Chiloane, K., and Komppula, M.: Atmospheric boundary layer top height in South Africa: measurements with lidar and radiosonde compared to three atmospheric models, Atmos. Chem. Phys., 14, 4263–4278, https://doi.org/10.5194/acp-14-4263-2014, 2014.

Kotthaus, S. and Grimmond, C. S. B.: Atmospheric boundary-layer characteristics from ceilometer measurements. Part 1: A new method to track mixed layer height and classify clouds, Quart. J. Roy. Meteor. Soc., 144, 1525–1538, https://doi.org/10.1002/qj.3299, 2018a.

Kotthaus, S. and Grimmond, C. S. B.: Atmospheric boundary-layer characteristics from ceilometer measurements. Part 2: Application to London's urban boundary layer, Quart. J. Roy. Meteor. Soc., 144, 1511–1524, https://doi.org/10.1002/qj.3298, 2018b.

Kotthaus, S., O'Connor, E., Münkel, C., Charlton-Perez, C., Haeffelin, M., Gabey, A. M., and Grimmond, C. S. B.: Recommendations for processing atmospheric attenuated backscatter profiles from Vaisala CL31 ceilometers, Atmos. Meas. Tech., 9, 3769–3791, https://doi.org/10.5194/amt-9-3769-2016, 2016.

Kotthaus, S., Halios, C. H., Barlow, J. F., and Grimmond, C.: Volume for pollution dispersion: London's atmospheric boundary layer during ClearfLo observed with two ground-based lidar types, Atmos. Environ., https://doi.org/10.1016/J.ATMOSENV.2018.06.042, 2018.

Kotthaus, S., Haeffelin, M., Drouin, M.-A., Dupont, J.-C., Grimmond, S., Haefele, A., Hervo, M., Poltera, Y., and Wiegner, M.: Tailored Algorithms for the Detection of the Atmospheric Boundary Layer Height from Common Automatic Lidars and Ceilometers (ALC), Remote. Sens., https://doi.org/10.3390/rs12193259, 2020.

Kouznetsov, R. D.: The summertime ABL structure over an antarctic oasis with a vertical Doppler sodar, Meteor. Z., 18, 163–167, https://doi.org/10.1127/0941-2948/2009/0369, 2009.

Kramar, V. F., Baykova, E., Kallistratova, M., Kouznetsov, R., and Kulichkov, S.: Ground-Based Remote Sensing of the ABL Structure in Moscow and Its Use to Estimate Pollutant Surface Emission Rates, J. Appl. Meteor. Climatol., 53, 1272–1281, https://doi.org/10.1175/JAMC-D-13-010.1, 2014.

Krishnamurthy, R., Newsom, R. K., Berg, L. K., Xiao, H., Ma, P. L., and Turner, D. D.: On the estimation of boundary layer heights: A machine learning approach, Atmos. Meas. Tech., 14, 4403–4424, https://doi.org/10.5194/AMT-14-4403-2021, 2021.

L., H. J.: Transport Layer Depth Calculations, in: 2nd Joint Conference on Applications of Air Pollution Modelling, New Orleans, LA, USA, pp. 787–791, American Meteorological Society, 45 Beacon St., Boston, MA, USA, 1980.

Lammert, A. and Bösenberg, J.: Determination of the convective boundary-layer height with laser remote sensing, Boundary-Layer Meteorol., 119, 159–170, https://doi.org/10.1007/s10546-005-9020-x, 2006.

Lange, D., Tiana-Alsina, J., Saeed, U., Tomas, S., and Rocadenbosch, F.: Atmospheric boundary layer height monitoring using a Kalman filter and backscatter lidar returns, IEEE Trans. Geosci. Remote Sens., 52, 4717–4728, https://doi.org/10.1109/TGRS.2013.2284110, 2013.

Lareau, N. P. and Clements, C. B.: Environmental controls on pyrocumulus and pyrocumulonimbus initiation and development, Atmos. Chem. Phys., 16, 4005–4022, https://doi.org/10.5194/acp-16-4005-2016, 2016.

Lauvaux, T., Miles, N. L., Deng, A., Richardson, S. J., Cambaliza, M. O., Davis, K. J., Gaudet, B., Gurney, K. R., Huang, J., O'Keefe, D., Song, Y., Karion, A., Oda, T., Patarasuk, R., Razlivanov, I., Sarmiento, D., Shepson, P., Sweeney, C., Turnbull, J., and Wu, K.: High-resolution atmospheric inversion of urban CO_2 emissions during the dormant season of the Indianapolis Flux Experiment (INFLUX), J. Geophys. Res. Atmos., 121, 5213–5236, https://doi.org/10.1002/2015JD024473, 2016.

Lee, J., Hong, J. W., Lee, K., Hong, J., Velasco, E., Lim, Y. J., Lee, J. B., Nam, K., and Park, J.: Ceilometer Monitoring of Boundary-Layer Height and Its Application in Evaluating the Dilution Effect on Air Pollution, Boundary-Layer Meteorol., 172, 435–455, https://doi.org/10.1007/s10546-019-00452-5, 2019.

Lehmann, V. and Teschke, G.: Advanced intermittent clutter filtering for radar wind profiler: signal separation through a Gabor frame expansion and its statistics, Annales Geophysicae, 26, 759–783, https://doi.org/10.5194/angeo-26-759-2008, 2008.

Lehner, M. and Rotach, M. W.: Current Challenges in Understanding and Predicting Transport and Exchange in the Atmosphere over Mountainous Terrain, Atmosphere, 9, 276, https://doi.org/10.3390/ATMOS9070276, 2018.

Lehning, M., Richner, H., and Kok, G. L.: Transport of air pollutants from the boundary layer to the free tropospere over complex terrain, Physics and Chemistry of the Earth, 23, 667 – 672, https://doi.org/10.1016/S0079-1946(98)00108-6, 1998.

LeMone, M. A., Tewari, M., Chen, F., and Dudhia, J.: Objectively determined fair-weather CBL depths in the ARW-WRF model and their comparison to CASES-97 observations, Mon. Wea. Rev., 141, 30–54, https://doi.org/10.1175/MWR-D-12-00106.1, 2013.

Lemone, M. A., Tewari, M., Chen, F., and Dudhia, J.: Objectively determined fair-weather NBL features in ARW-WRF and their comparison to CASES-97 observations, Mon. Wea. Rev., 142, 2709–2732, https://doi.org/10.1175/MWR-D-13-00358.1, 2014.

Lenschow, D. H., Wulfmeyer, V., and Senff, C.: Measuring Second- through Fourth-Order Moments in Noisy Data, J. Atmos. Oceanic Technol., 17, 1330–1347, https://doi.org/https://doi.org/10.1175/1520-0426(2000)017<1330:MSTFOM>2.0.CO;2, 2000.

Lewis, J. R., Welton, E. J., Molod, A. M., and Joseph, E.: Improved boundary layer depth retrievals from MPLNET, J. Geophys. Res. Atmos., 118, 9870–9879, https://doi.org/10.1002/jgrd.50570, 2013.

Li, H., Yang, Y., Hu, X.-m., Huang, Z., and Wang, G.: Evaluation of retrieval methods of daytime convective boundary layer height based on Lidar data, J. Geophys. Res., https://doi.org/10.1002/2016JD025620, 2017.

Li, J., Chu, Y., Li, X., and Dong, Y.: Long-term trends of global maximum atmospheric mixed layer heights derived from radiosonde measurements, Environmental Research Letters, https://doi.org/10.1088/1748-9326/ab7952, 2020.

Liljegren, J. C., Boukabara, S. A., Cady-Pereira, K., and Clough, S. A.: The effect of the half-width of the 22-GHz water vapor line on retrievals of temperature and water vapor profiles with a 12-channel microwave radiometer, IEEE Trans. Geosci. Remote Sens., 43, 1102–1108, https://doi.org/10.1109/TGRS.2004.839593, 2005.

Liu, B., Ma, Y., Gong, W., Zhang, M., and Yang, J.: Determination of boundary layer top on the basis of the characteristics of atmospheric particles, Atmos. Environ., 178, 140–147, https://doi.org/10.1016/J.ATMOSENV.2018.01.054, 2018.

Liu, B., Ma, Y., Guo, J., Gong, W., Zhang, Y., Mao, F., Li, J., Guo, X., and Shi, Y.: Boundary layer heights as derived from ground-based radar wind profiler in Beijing, IEEE Trans. Geosci. Remote Sens., 57, 8095–8104, https://doi.org/10.1109/TGRS.2019.2918301, 2019a.

Liu, B., Guo, J., Gong, W., Shi, L., Zhang, Y., and Ma, Y.: Characteristics and performance of vertical winds as observed by the radar wind profiler network of China, Atmos. Meas. Tech. Disc., https://doi.org/10.5194/amt-2020-75, 2020.

Liu, J., Huang, J., Chen, B., Zhou, T., Yan, H., Jin, H., Huang, Z., and Zhang, B.: Comparisons of PBL heights derived from CALIPSO and ECMWF reanalysis data over China, Journal of Quantitative Spectroscopy and Radiative Transfer, 153, 102 – 112, https://doi.org/10.1016/j.jqsrt.2014.10.011, 2015a.

Liu, L., Sun, X.-j., Liu, X.-c., Gao, T.-c., and Zhao, S.-j.: Comparison of Cloud Base Height Derived from a Ground-Based Infrared Cloud Measurement and Two Ceilometers, Advances in Meteorology, 2015, 1–8, https://doi.org/10.1155/2015/853861, 2015b.

Liu, S. and Liang, X. Z.: Observed diurnal cycle climatology of planetary boundary layer height, J. Climate, 23, 5790–5809, https://doi.org/10.1175/2010JCLI3552.1, 2010.

Liu, Z., Barlow, J. F., Chan, P.-W., Fung, J., Li, Y., Ren, C., Mak, H., and Ng, E.: A Review of Progress and Applications of Pulsed Doppler Wind LiDARs, Remote. Sens., 11, 2522, https://doi.org/10.3390/rs11212522, 2019b.

Löhnert, U. and Maier, O.: Operational profiling of temperature using ground-based microwave radiometry at Payerne: prospects and challenges, Atmos. Meas. Tech., 5, 1121–1134, https://doi.org/10.5194/amt-5-1121-2012, 2012.

Lolli, S., Delaval, A., Loth, C., Garnier, A., and Flamant, P. H.: 0.355-micrometer direct detection wind lidar under testing during a field campaign in consideration of ESA's ADM-Aeolus mission, Atmos. Meas. Tech., 6, 3349–3358, https://doi.org/10.5194/amt-6-3349-2013, 2013.

Lothon, M., Lenschow, D. H., and Mayor, S. D.: Coherence and Scale of Vertical Velocity in the Convective Boundary Layer from a Doppler Lidar, Boundary-Layer Meteorol., 121, 521–536, https://doi.org/10.1007/s10546-006-9077-1, 2006.

Lotteraner, C. and Piringer, M.: Mixing-Height Time Series from Operational Ceilometer Aerosol-Layer Heights, Boundary-Layer Meteorol., 161, 265–287, https://doi.org/10.1007/s10546-016-0169-2, 2016.

Luo, T., Yuan, R., and Wang, Z.: Lidar-based remote sensing of atmospheric boundary layer height over land and ocean, Atmos. Meas. Tech., 7, 173–182, https://doi.org/10.5194/amt-7-173-2014, 2014.

Löhnert, U., Turner, D. D., and Crewell, S.: Ground-Based Temperature and Humidity Profiling Using Spectral Infrared and Microwave Observations. Part I: Simulated Retrieval Performance in Clear-Sky Conditions, J. Appl. Meteor. Climatol., 48, 1017–1032, https://doi.org/10.1175/2008JAMC2060.1, 2009.

Mahrt, L.: Boundary-layer moisture regimes, Quart. J. Roy. Meteor. Soc., 117, 151–176, https://doi.org/10.1002/QJ.49711749708, 1991.

Mahrt, L., Heald, R. C., Lenschow, D. H., Stankov, B. B., and Troen, I. B.: An observational study of the structure of the nocturnal boundary layer, Boundary-Layer Meteorol., 17, 247–264, https://doi.org/10.1007/BF00117983, 1979.

Mahrt, L., Sun, J., and Stauffer, D.: Dependence of Turbulent Velocities on Wind Speed and Stratification, Boundary-Layer Meteorol., 155, 55–71, https://doi.org/10.1007/s10546-014-9992-5, 2015.

Manninen, A., Marke, T., Tuononen, M., and O'Connor, E.: Atmospheric boundary layer classification with Doppler lidar, J. Geophys. Res. Atmos., 123, 8172–8189, https://doi.org/10.1029/2017JD028169, 2018.

Manninen, A. J., O'Connor, E. J., Vakkari, V., and Petäjä, T.: A generalised background correction algorithm for a Halo Doppler lidar and its application to data from Finland, Atmos. Meas. Tech., 9, 817–827, https://doi.org/10.5194/amt-9-817-2016, 2016.

Marke, T., Crewell, S., Schemann, V., Schween, J. H., and Tuononen, M.: Long-Term Observations and High-Resolution Modeling of Midlatitude Nocturnal Boundary Layer Processes Connected to Low-Level Jets, J. Appl. Meteor. Climatol., 57, 1155 – 1170, https://doi.org/10.1175/JAMC-D-17-0341.1, 2018.

Markowicz, K. M., Flatau, P. J., Kardas, A. E., Remiszewska, J., Stelmaszczyk, K., Woeste, L., Markowicz, K. M., Flatau, P. J., Kardas, A. E., Remiszewska, J., Stelmaszczyk, K., and Woeste, L.: Ceilometer Retrieval of the Boundary Layer Vertical Aerosol Extinction Structure, J. Atmos. Oceanic Technol., 25, 928–944, https://doi.org/10.1175/2007JTECHA1016.1, 2008.

Marsik, F. J., Fischer, K. W., McDonald, T. D., Samson, P. J., Marsik, F. J., Fischer, K. W., McDonald, T. D., and Samson, P. J.: Comparison of Methods for Estimating Mixing Height Used during the 1992 Atlanta Field Intensive, J. Appl. Meteor., 34, 1802–1814, https://doi.org/10.1175/1520-0450(1995)034<1802:COMFEM>2.0.CO;2, 1995.

Martin, G. M., Bush, M. R., Brown, A. R., Lock, A. P., and Smith, R. N. B.: A New Boundary Layer Mixing Scheme. Part II: Tests in Climate and Mesoscale Models, Mon. Wea. Rev., 128, 3200–3217, https://doi.org/10.1175/1520-0493(2000)128<3200:ANBLMS>2.0.CO;2, 2000.

Martinet, P., Cimini, D., Burnet, F., Ménétrier, B., Michel, Y., and Unger, V.: Improvement of numerical weather prediction model analysis during fog conditions through the assimilation of ground-based microwave radiometer observations: a 1D-Var study, Atmos. Meas. Tech., 13, 6593–6611, https://doi.org/10.5194/amt-13-6593-2020, 2020.

Martucci, G., Matthey, R., Mitev, V., and Richner, H.: Comparison between backscatter lidar and radiosonde measurements of the diurnal and nocturnal stratification in the lower troposphere, J. Atmos. Oceanic Technol., 24, 1231–1244, https://doi.org/10.1175/JTECH2036.1, 2007.

Martucci, G., Matthey, R., Mitev, V., and Richner, H.: Frequency of Boundary-Layer-Top Fluctuations in Convective and Stable Conditions Using Laser Remote Sensing, Boundary-Layer Meteorol., 135, 313–331, https://doi.org/10.1007/s10546-010-9474-3, 2010a.

Martucci, G., Milroy, C., and O'Dowd, C. D.: Detection of Cloud-Base Height Using Jenoptik CHM15K and Vaisala CL31 Ceilometers, J. Atmos. Oceanic Technol., 27, 305–318, https://doi.org/10.1175/2009JTECHA1326.1, 2010b.

Mather, J. H. and Voyles, J. W.: The ARM Climate Research Facility: A Review of Structure and Capabilities, Bull. Amer. Meteor. Soc., 94, 377–392, https://doi.org/10.1175/BAMS-D-11-00218.1, 2013.

Matthias, V., Balis, D., Bösenberg, J., Eixmann, R., Iarlori, M., Komguem, L., Mattis, I., Papayannis, A., Pappalardo, G., Perrone, M., et al.: Vertical aerosol distribution over Europe: Statistical analysis of Raman lidar data from 10 European Aerosol Research Lidar Network (EARLINET) stations, J. Geophys. Res. Atmos., 109, https://doi.org/10.1029/2004JD004638, 2004.

McGrath-Spangler, E. L. and Denning, A. S.: Global seasonal variations of midday planetary boundary layer depth from CALIPSO space-borne LIDAR, J. Geophys. Res. Atmos., 118, 1226–1233, https://doi.org/10.1002/jgrd.50198, 2013.

Medeiros, B., Hall, A., and Stevens, B.: What controls the mean depth of the PBL?, J. Climate, 18, 3157–3172, https://doi.org/10.1175/JCLI3417.1, 2005.

Melecio-Vázquez, D., González-Cruz, J., Arend, M., Han, Z., Gutierrez, E., Dempsey, M., and Booth, J.: New York metro-area boundary layer catalogue: Boundary layer height and stability conditions from long-term observations, in: Ninth Int. Conf. on Urban Climate/12th Symp. on the Urban Environment, edited by IAUX and Soc., A. M., pp. 9–2, http://www.meteo.fr/icuc9/presentations/NOMTM/NOMTM9-2.pdf, 2015.

Menut, L., Flamant, C., Pelon, J., and Flamant, P. H.: Urban boundary-layer height determination from lidar measurements over the Paris area, Appl. Opt., 38, 945, https://doi.org/10.1364/AO.38.000945, 1999.

Messager, C., Parker, D. J., Reitebuch, O., Agusti-Panareda, A., Taylor, C. M., and Cuesta, J.: Structure and dynamics of the Saharan atmospheric boundary layer during the West African monsoon onset: Observations and analyses from the research flights of 14 and 17 July 2006, Quart. J. Roy. Meteor. Soc., 136, 107–124, https://doi.org/10.1002/qj.469, 2010.

Millán, L., Lebsock, M., Fishbein, E., Kalmus, P., and Teixeira, J.: Quantifying Marine Boundary Layer Water Vapor beneath Low Clouds with Near-Infrared and Microwave Imagery, J. Appl. Meteor. Climatol., 55, 213–225, https://doi.org/10.1175/JAMC-D-15-0143.1, 2016.

Milroy, C., Martucci, G., Lolli, S., Loaec, S., Sauvage, L., Xueref-Remy, I., Lavrič, J. V., Ciais, P., Feist, D. G., Biavati, G., and O'Dowd, C. D.: An assessment of pseudo-operational ground-based light detection and ranging sensors to determine the boundary-layer structure in the coastal atmosphere, Adv. Meteorol., 2012, 1–19, https://doi.org/10.1155/2012/929080, 2012.

Min, J. S., Park, M. S., Chae, J. H., and Kang, M.: Integrated System for Atmospheric Boundary Layer Height Estimation (ISABLE) using a ceilometer and microwave radiometer, Atmos. Meas. Tech., 13, 6965–6987, https://doi.org/10.5194/AMT-13-6965-2020, 2020.

Moigne, P. L., Legain, D., Lagarde, F., Potes, M., Tzanos, D., Moulin, E., Barrié, J., Salgado, R., Messiaen, G., Fiandrino, A., et al.: Evaluation of the lake model FLake over a coastal lagoon during the THAUMEX field campaign, Tellus A: Dynamic Meteorology and Oceanography, 65, 20 951, https://doi.org/10.3402/tellusa.v65i0.20951, 2013.

Moreira, G. d. A., Marques, M., Nakaema, W., de CA Moreira, A., and Landulfo, E.: Detecting the planetary boundary layer height from low-level jet with Doppler lidar measurements, in: Lidar Technologies, Techniques, and Measurements for Atmospheric Remote Sensing XI, vol. 9645, p. 96450F, International Society for Optics and Photonics, https://doi.org/10.1117/12.2195278, 2015.

Morille, Y., Haeffelin, M., Drobinski, P., and Pelon, J.: STRAT: An automated algorithm to retrieve the vertical structure of the atmosphere from single-channel lidar data, J. Atmos. Oceanic Technol., 24, 761–775, https://doi.org/10.1175/JTECH2008.1, 2007.

Mues, A., Rupakheti, M., Münkel, C., Lauer, A., Bozem, H., Hoor, P., Butler, T., and Lawrence, M. G.: Investigation of the mixing layer height derived from ceilometer measurements in the Kathmandu Valley and implications for local air quality, Atmos. Chem. Phys., 17, 8157–8176, https://doi.org/10.5194/acp-17-8157-2017, 2017.

Münkel, C.: Mixing height determination with lidar ceilometers–results from Helsinki Testbed, Meteor. Z., 16, 451–459, https://doi.org/10.1127/0941-2948/2007/0221, 2007.

Münkel, C.: Combining gradient and profile fit method for an advanced ceilometer-based boundary layer height detection algorithm, in: 18th International Symposium for the Advancement of Boundary-Layer Remote Sensing, edited by ISARS2016, p. 8 June, 2016.

Ndao, S., Rinelle, D. N., Badiane, D., Lenouo, A., and Sall, S. M.: Study of Boundary Layer Height over West Africa, Journal of Geoscience and Environment Protection, pp. 179–194, https://doi.org/10.4236/gep.2019.711013, 2019.

Neisser, J., Adam, W., Beyrich, F., Leiterer, U., and Steinhagen, H.: Atmospheric boundary layer monitoring at the Meteorological Observatory Lindenberg as a part of the "Lindenberg Column": Facilities and selected results, Meteor. Z., 11, 241–253, https://doi.org/10.1127/0941-2948/2002/0011-0241, 2002.

Nielsen-Gammon, J. W., Powell, C. L., Mahoney, M. J., Angevine, W. M., Senff, C., White, A., Berkowitz, C., Doran, C., and Knupp, K.: Multisensor estimation of mixing heights over a coastal city, J. Appl. Meteor. Climatol., 47, 27–43, https://doi.org/10.1175/2007JAMC1503.1, 2008.

Nieuwstadt, F. and Duynkerke, P.: Turbulence in the atmospheric boundary layer, Atmos. Res., 40, 111–142, https://doi.org/10.1016/0169-8095(95)00034-8, 1996.

Niyogi, D.: Urban impacts on regional rainfall climatology, in: 9th International Conference on Urban Climate jointly with 12th Symposium on the Urban Environment, edited by IAUC and Soc., A. M., pp. UCP9–7, http://www.meteo.fr/icuc9/presentations/UCP/UCP9-7.pdf, 2015.

Nowak, J. L., Siebert, H., Szodry, K.-E., and Malinowski, S. P.: Coupled and decoupled stratocumulus-topped boundary layers: turbulence properties, Atmos. Chem. Phys., 21, 10 965–10 991, https://doi.org/10.5194/ACP-21-10965-2021, 2021.

Nyeki, S., Eleftheriadis, K., Baltensperger, U., Colbeck, I., Fiebig, M., Fix, A., Kiemle, C., Lazaridis, M., and Petzold, A.: Airborne Lidar and in-situ Aerosol Observations of an Elevated Layer, Leeward of the European Alps and Apennines, Geophys. Res. Lett., 29, 3–6, https://doi.org/10.1029/2002GL014897, 2002.

O'Connor, E. J., Illingworth, A. J., and Hogan, R. J.: A Technique for Autocalibration of Cloud Lidar, J. Atmos. Oceanic Technol., 21, 777–786, 2004.

O'Connor, E. J., Illingworth, A. J., Brooks, I. M., Westbrook, C. D., Hogan, R. J., Davies, F., and Brooks, B. J.: A Method for Estimating the Turbulent Kinetic Energy Dissipation Rate from a Vertically Pointing Doppler Lidar, and Independent Evaluation from Balloon-Borne In Situ Measurements, J. Atmos. Oceanic Technol., 27, 1652–1664, https://doi.org/10.1175/2010JTECHA1455.1, 2010.

Pal, S. and Haeffelin, M.: Forcing mechanisms governing diurnal, seasonal, and interannual variability in the boundary layer depths: Five years of continuous lidar observations over a suburban site near Paris, J. Geophys. Res. Atmos., 120, 11,936–11,956, https://doi.org/10.1002/2015JD023268, 2015.

Pal, S., Xueref-Remy, I., Ammoura, L., Chazette, P., Gibert, F., Royer, P., Dieudonné, E., Dupont, J. C., Haeffelin, M., Lac, C., Lopez, M., Morille, Y., and Ravetta, F.: Spatio-temporal variability of the atmospheric boundary layer depth over the Paris agglomeration: An assessment of the impact of the urban heat island intensity, Atmos. Environ., 63, 261–275, https://doi.org/10.1016/j.atmosenv.2012.09.046, 2012.

Pal, S., Haeffelin, M., and Batchvarova, E.: Exploring a geophysical process-based attribution technique for the determination of the atmospheric boundary layer depth using aerosol lidar and near-surface meteorological measurements, J. Geophys. Res. Atmos., 118, 9277–9295, https://doi.org/10.1002/jgrd.50710, 2013.

Palmén, E. H. and Newton, C. W.: Atmospheric circulation systems: their structure and physical interpretation, vol. 13, Academic press, 1969.

Pandolfi, M., Martucci, G., Querol, X., Alastuey, A., Wilsenack, F., Frey, S., O'Dowd, C. D., and Dall'Osto, M.: Continuous atmospheric boundary layer observations in the coastal urban area of Barcelona during SAPUSS, Atmos. Chem. Phys., 13, 4983–4996, https://doi.org/10.5194/acp-13-4983-2013, 2013.

Parikh, N. and Parikh, J.: Systematic tracking of boundary layer aerosols with laser radar, Optics & Laser Technology, 34, 177–185, https://doi.org/10.1016/S0030-3992(01)00107-4, 2002.

Park, M.-S., Park, S.-H., Chae, J.-H., Choi, M.-H., Song, Y., Kang, M., and Roh, J.-W.: High-resolution urban observation network for user-specific meteorological information service in the Seoul Metropolitan Area, South Korea, Atmos. Meas. Tech., 10, 1575–1594, https://doi.org/10.5194/amt-10-1575-2017, 2017.

Päschke, E., Leinweber, R., and Lehmann, V.: An assessment of the performance of a 1.5 μm Doppler lidar for operational vertical wind profiling based on a 1-year trial, Atmos. Meas. Tech., 8, 2251–2266, https://doi.org/doi:10.5194/amt-8-2251-2015, 2015.

Pattantyús-Ábrahám, M., Mattis, I., Begbie, R., Bravo-Aranda, J., Brettle, M., Cermak, J., Drouin, M.-A., Geiß, A., Görsdorf, U., Haefele, A., Haeffelin, M., Maxime, H., Komínková, K., Leinweber, R., Münkel, C., Pönitz, K., Vande Hey, J., Wagner, F., and Wiegner, M.: The dataset of the CeiLinEx 2015 Ceilometer-Inter-comparison Experiment, Version v001, https://doi.org/10.5676/DWD/CEILINEX2015, 2017.

Pearson, G., Davies, F., and Collier, C.: Remote sensing of the tropical rain forest boundary layer using pulsed Doppler lidar, Atmos. Chem. Phys., 10, 5891–5901, https://doi.org/10.5194/acp-10-5891-2010, 2010.

Peña, A., Gryning, S., and Hasager, C. B.: Measurements and modelling of the wind speed profile in the marine atmospheric boundary layer, Boundary-Layer Meteorol., 129, 479–495, 2008.

Peña, A., Gryning, S., and Hahmann, A. N.: Observations of the atmospheric boundary layer height under marine upstream flow conditions at a coastal site, J. Geophys. Res., 118, 1924–1940, https://doi.org/10.1002/jgrd.50175, 2013.

Peña, A., Floors, R., Sathe, A., Gryning, S. E., Wagner, R., Courtney, M. S., Larsén, X. G., Hahmann, A. N., and Hasager, C. B.: Ten Years of Boundary-Layer and Wind-Power Meteorology at Høvsøre, Denmark, Boundary-Layer Meteorol., 158, 1–26, https://doi.org/10.1007/S10546-015-0079-8/FIGURES/9, 2016.

Peng, J., Grimmond, C., Fu, X., Chang, Y., Zhang, G., Guo, J., Tang, C., GAO, J., Xu, X., Tan, J., Peng, J., Grimmond, C., Fu, X., Chang, Y., Zhang, G., Guo, J., Tang, C., GAO, J., Xu, X., and Tan, J.: Ceilometer based analysis of Shanghai's boundary layer height (under rain and fog free conditions), J. Atmos. Oceanic Technol., https://doi.org/10.1175/JTECH-D-16-0132.1, 2017.

Pentikäinen, P., O'Connor, E. J., Manninen, A. J., and Ortiz-Amezcua, P.: Methodology for deriving the telescope focus function and its uncertainty for a heterodyne pulsed Doppler lidar, Atmos. Meas. Tech., 13, 2849–2863, https://doi.org/10.5194/amt-13-2849-2020, 2020.

Petetin, H., Jeoffrion, M., Sauvage, B., Athier, G., Blot, R., Boulanger, D., Clark, H., Cousin, J. M., Gheusi, F., Nedelec, P., Steinbacher, M., and Thouret, V.: Representativeness of the IAGOS airborne measurements in the lower troposphere, Elementa, 6, https://doi.org/10.1525/elementa.280, 2018.

Pichugina, Y. L. and Banta, R. M.: Stable boundary layer depth from high-resolution measurements of the mean wind profile, J. Appl. Meteor. Climatol., 49, 20–35, https://doi.org/10.1175/2009JAMC2168.1, 2010.

Pichugina, Y. L., Tucker, S. C., Banta, R. M., Brewer, W. A., Kelley, N. D., Jonkman, B. J., and Newsom, R. K.: Horizontal-velocity and variance measurements in the stable boundary layer using Doppler lidar: Sensitivity to averaging procedures, J. Atmos. Oceanic Technol., 25, 1307–1327, https://journals.ametsoc.org/view/journals/atot/25/8/2008jtecha988_1.xml, 2008.

Pichugina, Y. L., Banta, R. M., Brewer, W. A., Sandberg, S. P., and Hardesty, R. M.: Doppler Lidar–Based Wind-Profile Measurement System for Offshore Wind-Energy and Other Marine Boundary Layer Applications, J. Appl. Meteor. Climatol., 51, https://doi.org/10.1175/JAMC-D-11-040.1, 2012.

Piironen, A. K. and Eloranta, E. W.: Convective boundary layer mean depths and cloud geometrical properties obtained from volume imaging lidar data, J. Geophys. Res. Atmos., 100, 25 569–25 576, 1995.

Piringer, M., Joffre, S., Baklanov, A., Christen, A., Deserti, M., De Ridder, K., Emeis, S., Mestayer, P., Tombrou, M., Middleton, D., et al.: The surface energy balance and the mixing height in urban areas—activities and recommendations of COST-Action 715, Boundary-Layer Meteorol., 124, 3–24, https://doi.org/10.1007/s10546-007-9170-0, 2007.

Piters, A. J. M., Boersma, K. F., Kroon, M., Hains, J. C., Van Roozendael, M., Wittrock, F., Abuhassan, N., Adams, C., Akrami, M., Allaart, M. A. F., Apituley, A., Beirle, S., Bergwerff, J. B., Berkhout, A. J. C., Brunner, D., Cede, A., Chong, J., Clémer, K., Fayt, C., Frieß, U., Gast, L. F. L., Gil-Ojeda, M., Goutail, F., Graves, R., Griesfeller, A., Großmann, K., Hemerijckx, G., Hendrick, F., Henzing, B., Herman, J., Hermans, C., Hoexum, M., van der Hoff, G. R., Irie, H., Johnston, P. V., Kanaya, Y., Kim, Y. J., Klein Baltink, H., Kreher, K., de Leeuw, G., Leigh, R., Merlaud, A., Moerman, M. M., Monks, P. S., Mount, G. H., Navarro-Comas, M., Oetjen, H., Pazmino, A., Perez-Camacho, M., Peters, E., du Piesanie, A., Pinardi, G., Puentedura, O., Richter, A., Roscoe, H. K., Schönhardt, A., Schwarzenbach, B., Shaiganfar, R., Sluis, W., Spinei, E., Stolk, A. P., Strong, K., Swart, D. P. J., Takashima, H., Vlemmix, T., Vrekoussis, M., Wagner, T., Whyte, C., Wilson, K. M., Yela, M., Yilmaz, S., Zieger, P., and Zhou, Y.: The Cabauw Intercomparison campaign for Nitrogen Dioxide measuring Instruments (CINDI): design, execution, and early results, Atmos. Meas. Tech., 5, 457–485, https://doi.org/10.5194/amt-5-457-2012, 2012.

Poltera, Y., Martucci, G., Collaud Coen, M., Hervo, M., Emmenegger, L., Henne, S., Brunner, D., and Haefele, A.: PathfinderTURB: an automatic boundary layer algorithm. Development, validation and application to study the impact on in-situ measurements at the Jungfraujoch, Atmos. Chem. Phys., pp. 1–34, https://doi.org/10.5194/acp-17-10051-2017, 2017.

Pospichal, B., Küchler, N., Löhnert, U., and Güldner, J.: J-CAL (Joint microwave calibration) - Recommendations for operation and calibration of Microwave Radiometers (MWR) within a network, http://www.toprof.imaa.cnr.it/images/toprof/pubs/TOPROF_MWR_recommendations_20160315.pdf, 2016.

Potes, M., Salgado, R., Costa, M. J., Morais, M., Bortoli, D., Kostadinov, I., and Mammarella, I.: Lake–atmosphere interactions at Alqueva reservoir: a case study in the summer of 2014, Tellus A: Dynamic Meteorology and Oceanography, 69, 1272 787, https://doi.org/10.1080/16000870.2016.1272787, 2017.

Rahn, D. A. and Mitchell, C. J.: Diurnal Climatology of the Boundary Layer in Southern California Using AMDAR Temperature and Wind Profiles, J. Appl. Meteor. Climatol., 55, 1123–1137, https://doi.org/10.1175/JAMC-D-15-0234.1, 2016.

Ramon, J., Lledó, L., Pérez-Zanón, N., Soret, A., and Doblas-Reyes, F. J.: The Tall Tower Dataset: a unique initiative to boost wind energy research, Earth System Science Data, 12, 429–439, https://doi.org/10.5194/essd-12-429-2020, 2020.

Reitebuch, O., Strassburger, A., Emeis, S., and Kuttler, W.: Nocturnal secondary ozone concentration maxima analysed by sodar observations and surface measurements, Atmos. Environ., 34, 4315–4329, https://doi.org/10.1016/S1352-2310(00)00185-0, 2000.

Renju, R., Raju, C. S., Mishra, M. K., Mathew, N., Rajeev, K., and Moorthy, K. K.: Atmospheric Boundary Layer Characterization Using Multiyear Ground-Based Microwave Radiometric Observations Over a Tropical Coastal Station, IEEE Trans. Geosci. Remote Sens., 55, 6877–6882, https://doi.org/10.1109/TGRS.2017.2735626, 2017.

Rieutord, T., Aubert, S., and Machado, T.: Deriving boundary layer height from aerosol lidar using machine learning: KABL and ADABL algorithms, Atmos. Meas. Tech., 14, 4335–4353, https://doi.org/10.5194/amt-14-4335-2021, 2021.

Robinson, I., Jack, J. W., Rae, C. F., and Moncrieff, J. B.: A robust optical parametric oscillator and receiver telescope for differential absorption lidar of greenhouse gases, Proc. SPIE, 9645, 9645 – 9645 – 7, https://doi.org/10.1117/12.2197251, 2015.

Rodgers, C.: Inverse methods for atmospheric sounding: theory and practice, Series on atmospheric, oceanic and planetary physics, v.2, World Scientific, Singapore, [River Edge, N.J.], 2000.

Rose, T., Crewell, S., Löhnert, U., and Simmer, C.: A network suitable microwave radiometer for operational monitoring of the cloudy atmosphere, Atmos. Res., 75, 183 – 200, https://doi.org/https://doi.org/10.1016/j.atmosres.2004.12.005, cLIWA-NET: Observation and Modelling of Liquid Water Clouds, 2005.

Rotach, M. W. and Zardi, D.: On the boundary-layer structure over highly complex terrain: Key findings from MAP, Quart. J. Roy. Meteor. Soc., 133, 937–948, https://doi.org/10.1002/QJ.71, 2007.

Ruffieux, D.: Evaluation of WMO-CBS Wind Profiler Survey, https://www.wmo.int/pages/prog/www/OSY/Meetings/ICT-IOS8/documents/ICT-IOS8-INF-4-Wind-profiler-survey.pdf, 2014.

Rye, B. J. and Hardesty, R. M.: Discrete spectral peak estimation in incoherent backscatter heterodyne lidar. I: Spectral accumulation and the Cramer-Rao lower bound, IEEE Trans. Geosci. Remote Sens., 31, 16–27, https://doi.org/10.1109/36.210440, 1993.

Rüfenacht, R., Haefele, A., Pospichal, B., Cimini, D., Bircher-Adrot, S., Turp, M., and Sugier, J.: EUMETNET opens to microwave radiometers for operational thermodynamical profiling in Europe, Bulletin of Atmospheric Science and Technology, 2, 231–261, https://doi.org/10.1007/s42865-021-00033-w, 2021.

Saeed, U., Rocadenbosch, F., and Crewell, S.: Adaptive estimation of the stable boundary layer height using combined lidar and microwave radiometer observations, IEEE Trans. Geosci. Remote Sens., 54, 6895–6906, https://doi.org/10.1109/TGRS.2016.2586298, 2016.

Sathe, A. and Mann, J.: A review of turbulence measurements using ground-based wind lidars, Atmos. Meas. Tech., 6, 3147–3167, https://doi.org/10.5194/amt-6-3147-2013, 2013.

Sathe, A., Mann, J., Vasiljevic, N., and Lea, G.: A six-beam method to measure turbulence statistics using ground-based wind lidars, Atmos. Meas. Tech., 8, 729–740, https://doi.org/10.5194/amt-8-729-2015, 2015.

Sathyanadh, A., Prabhakaran, T., Patil, C., and Karipot, A.: Planetary boundary layer height over the Indian subcontinent : Variability and controls with respect to monsoon, Atmos. Res., 195, 44–61, https://doi.org/10.1016/j.atmosres.2017.05.010, 2017.

Sawyer, V. and Li, Z.: Detection, variations and intercomparison of the planetary boundary layer depth from radiosonde, lidar and infrared spectrometer, Atmos. Environ., 79, 518–528, https://doi.org/10.1016/j.atmosenv.2013.07.019, 2013.

Scarino, A. J., Obland, M. D., Fast, J. D., Burton, S. P., Ferrare, R. A., Hostetler, C. A., Berg, L. K., Lefer, B., Haman, C., Hair, J. W., Rogers, R. R., Butler, C., Cook, A. L., Harper, D. B., and Northwest, Pacific and Sciences, Atmospheric and Consultants, Trinity and Rouge, Baton: Comparison of mixed layer heights from airborne high spectral resolution lidar, ground-based measurements, and the WRF-Chem model during CalNex and CARES, Atmos. Chem. Phys., pp. 5547–5560, https://doi.org/10.5194/acp-14-5547-2014, 2014.

Schäfer, K., Emeis, S. M., Rauch, A., Münkel, C., and Vogt, S.: Determination of the mixing layer height from ceilometer backscatter profiles, in: Remote Sensing of Clouds and the Atmosphere XI, edited by Comeron, A., Carleer, M. R., Picard, R. H., and Sifakis, N. I., pp. 248–259, International Society for Optics and Photonics, https://doi.org/10.1117/12.565592, 2004.

Schmid, F., Schmidli, J., Hervo, M., and Haefele, A.: Diurnal Valley Winds in a Deep Alpine Valley: Observations, Atmosphere, 11, https://doi.org/10.3390/atmos11010054, 2020.

Schmid, P. and Niyogi, D.: A Method for Estimating Planetary Boundary Layer Heights and Its Application over the ARM Southern Great Plains Site, J. Atmos. Oceanic Technol., 29, 316–322, https://doi.org/10.1175/JTECH-D-11-00118.1, 2012.

Schween, J. H., Hirsikko, A., Löhnert, U., Crewell, S., and Iek, T.: Mixing-layer height retrieval with ceilometer and Doppler lidar: from case studies to long-term assessment, Atmos. Meas. Tech., pp. 3685–3704, https://doi.org/10.5194/amt-7-3685-2014, 2014.

Seibert, P., Beyrich, F., Gryning, S.-E., Joffre, S., Rasmussen, A., and Tercier, P.: Review and intercomparison of operational methods for the determination of the mixing height, Atmos. Environ., 34, 1001 – 1027, https://doi.org/10.1016/S1352-2310(99)00349-0, 2000.

Seidel, D. J., Ao, C. O., and Li, K.: Estimating climatological planetary boundary layer heights from radiosonde observations: Comparison of methods and uncertainty analysis, J. Geophys. Res. Atmos., 115, n/a–n/a, https://doi.org/10.1029/2009JD013680, d16113, 2010.

Seidel, D. J., Zhang, Y., Beljaars, A., Golaz, J.-C., Jacobson, A. R., and Medeiros, B.: Climatology of the planetary boundary layer over the continental United States and Europe, J. Geophys. Res., 117, D17 106, https://doi.org/10.1029/2012JD018143, 2012.

Serafin, S., Adler, B., Cuxart, J., De Wekker, S. F., Gohm, A., Grisogono, B., Kalthoff, N., Kirshbaum, D. J., Rotach, M. W., Schmidli, J., Stiperski, I., Večenaj, Ž., and Zardi, D.: Exchange Processes in the Atmospheric Boundary Layer Over Mountainous Terrain, Atmosphere, 9, 102, https://doi.org/10.3390/ATMOS9030102, 2018.

Shi, Z., Vu, T., Kotthaus, S., Harrison, R. M., Grimmond, S., Yue, S., Zhu, T., Lee, J., Han, Y., Demuzere, M., Dunmore, R. E., Ren, L., Liu, D., Wang, Y., Wild, O., Allan, J., Acton, W. J., Barlow, J., Barratt, B., Beddows, D., Bloss, W. J., Calzolai, G., Carruthers, D., Carslaw, D. C., Chan, Q., Chatzidiakou, L., Chen, Y., Crilley, L., Coe, H., Dai, T., Doherty, R., Duan, F., Fu, P., Ge, B., Ge, M., Guan, D., Hamilton, J. F., He, K., Heal, M., Heard, D., Hewitt, C. N., Hollaway, M., Hu, M., Ji, D., Jiang, X., Jones, R., Kalberer, M., Kelly, F. J., Kramer, L., Langford, B., Lin, C., Lewis, A. C., Li, J., Li, W., Liu, H., Liu, J., Loh, M., Lu, K., Lucarelli, F., Mann, G., McFiggans, G., Miller, M. R., Mills, G., Monk, P., Nemitz, E., O'Connor, F., Ouyang, B., Palmer, P. I., Percival, C., Popoola, O., Reeves, C., Rickard, A. R., Shao, L., Shi, G., Spracklen, D., Stevenson, D., Sun, Y., Sun, Z., Tao, S., Tong, S., Wang, Q., Wang, W., Wang, X., Wang, X., Wang, Z., Wei, L., Whalley, L., Wu, X., Wu, Z., Xie, P., Yang, F., Zhang, Q., Zhang, Y., Zhang, Y., and Zheng, M.: Introduction to the special issue

"In-depth study of air pollution sources and processes within Beijing and its surrounding region (APHH-Beijing)", Atmos. Chem. Phys., 19, 7519–7546, https://doi.org/10.5194/acp-19-7519-2019, 2019.

Shimizu, A., Nishizawa, T., Jin, Y., Kim, S.-W., Wang, Z., Batdorj, D., and Sugimoto, N.: Evolution of a lidar network for tropospheric aerosol detection in East Asia, Optical Engineering, 56, 1 – 12, https://doi.org/10.1117/1.OE.56.3.031219, 2016.

Sicard, M., Pérez, C., Rocadenbosch, F., Baldasano, J., and García-Vizcaino, D.: Mixed-layer depth determination in the Barcelona coastal area from regular lidar measurements: methods, results and limitations, Boundary-Layer Meteorol., 119, 135–157, https://doi.org/10.1007/s10546-005-9005-9, 2006.

Simeonov, V., Larcheveque, G., Quaglia, P., Van Den Bergh, H., and Calpini, B.: Influence of the photomultiplier tube spatial uniformity on lidar signals, Appl. Opt., 38, 5186–5190, https://doi.org/10.1364/AO.38.005186, 1999.

Sinclair, V. A., Ritvanen, J., Urbancic, G., Statnaia, I., Batrak, Y., Moisseev, D., and Kurppa, M.: Boundary-layer height and surface stability at SMEAR II, Hyytiälä, Finland in ERA5 and observations, Atmos. Meas. Tech. Disc., https://doi.org/10.5194/amt-2021-295, 2021.

Singal, S. P.: Acoustic Remote Sensing Applications, Springer Berlin Heidelberg, 1997.

Singh, N., Solanki, R., Ojha, N., Janssen, R. H. H., and Pozzer, A.: Boundary layer evolution over the central Himalayas from radio wind profiler and model simulations, Atmos. Chem. Phys., pp. 10 559–10 572, https://doi.org/10.5194/acp-16-10559-2016, 2016.

Smalikho, I. N. and Banakh, V. A.: Measurements of wind turbulence parameters by a conically scanning coherent Doppler lidar in the atmospheric boundary layer, Atmos. Meas. Tech., 10, 4191–4208, https://doi.org/10.5194/amt-10-4191-2017, 2017.

Smith, E. N., Greene, B. R., Bell, T. M., Blumberg, W. G., Wakefield, R., Reif, D., Niu, Q., Wang, Q., and Turner, D. D.: Evaluation and Applications of Multi-Instrument Boundary-Layer Thermodynamic Retrievals, Boundary-Layer Meteorol., 181, 95–123, https://doi.org/10.1007/S10546-021-00640-2, 2021.

Sokół, P., Stachlewska, I., Ungureanu, I., and Stefan, S.: Evaluation of the boundary layer morning transition using the CL-31 ceilometer signals, Acta Geophysica, 62, 367–380, https://doi.org/10.2478/s11600-013-0158-5, 2014.

Solheim, F., Godwin, J. R., Westwater, E. R., Han, Y., Keihm, S. J., Marsh, K., and Ware, R.: Radiometric profiling of temperature, water vapor and cloud liquid water using various inversion methods, Radio Science, 33, 393–404, https://doi.org/10.1029/97RS03656, 1998.

Spirig, C., Guenther, A., Greenberg, J. P., Calanca, P., and Tarvainen, V.: Tethered balloon measurements of biogenic volatile organic compounds at a Boreal forest site, Atmos. Chem. Phys., 4, 215–229, https://doi.org/10.5194/acp-4-215-2004, 2004.

Stachlewska, I. S., Piądłowski, M., Migacz, S., Szkop, A., Zielińska, A. J., and Swaczyna, P. L.: Ceilometer observations of the boundary layer over Warsaw, Poland, Acta Geophysica, 60, 1386–1412, https://doi.org/10.2478/s11600-012-0054-4, 2012.

Steeneveld, G. J., van de Wiel, B. J., and Holtslag, A. A.: Diagnostic equations for the stable boundary layer height: Evaluation and dimensional analysis, J. Appl. Meteor. Climatol., 46, 212–225, https://doi.org/10.1175/JAM2454.1, 2007.

Steyn, D. G., Baldi, M., and Hoff, R. M.: The Detection of Mixed Layer Depth and Entrainment Zone Thickness from Lidar Backscatter Profiles, J. Atmos. Oceanic Technol., 16, 953–959, https://doi.org/10.1175/1520-0426(1999)016<0953:TDOMLD>2.0.CO;2, 1999.

Stirnberg, R., Cermak, J., Kotthaus, S., Haeffelin, M., Andersen, H., Fuchs, J., Kim, M., Petit, J. E., and Favez, O.: Meteorology-driven variability of air pollution (PM1) revealed with explainable machine learning, Atmos. Chem. Phys., 21, 3919–3948, https://doi.org/10.5194/acp-21-3919-2021, 2021.

Stohl, a., Forster, C., Frank, A., Seibert, P., and Wotawa, G.: Technical note: The Lagrangian particle dispersion model FLEXPART version 6.2, Atmos. Chem. Phys. Disc., 5, 4739–4799, https://doi.org/10.5194/acpd-5-4739-2005, 2005.

Straume, A., Rennie, M., Isaksen, L., de Kloe, J., Marseille, G.-J., Stoffelen, A., Flament, T., Stieglitz, H., Dabas, A., Huber, D., Reitebuch, O., Lemmerz, C., Lux, O., Marksteiner, U., Weiler, F., Witschas, B., Meringer, M., Schmidt, K., Nikolaus, I., Geiss, A., Flamant, P., Kanitz, T., Wernham, D., von Bismarck, J., Bley, S., Fehr, T., Floberghagen, R., and Parinello, T.: ESA's Space-Based Doppler Wind Lidar Mission Aeolus – First Wind and Aerosol Product Assessment Results, EPJ Web of Conferences, 237, 01 007, https://doi.org/10.1051/EPJCONF/202023701007, 2020.

Stull, R.: An Introduction to Boundary Layer Meteorology, Atmospheric and Oceanographic Sciences Library, Springer Netherlands, 1988.

Sujatha, P., Mahalakshmi, D. V., Ramiz, A., Rao, P. V. N., and Naidu, C. V.: Ventilation coefficient and boundary layer height impact on urban air quality, Cogent Environmental Science, 2, https://doi.org/10.1080/23311843.2015.1125284, 2016.

Sørensen, J., Rasmussen, A., and Svensmark, H.: Forecast of atmospheric boundary-layer height utilised for ETEX real-time dispersion modelling, Physics and Chemistry of the Earth, 21, 435–439, https://doi.org/10.1016/S0079-1946(97)81138-X, ocean and Atmosphere, 1996.

Tang, G., Zhang, J., Zhu, X., Song, T., Münkel, C., Hu, B., Schäfer, K., Liu, Z., Zhang, J., Wang, L., Xin, J., Suppan, P., and Wang, Y.: Mixing layer height and its implications for air pollution over Beijing, China, Atmos. Chem. Phys., 16, 2459–2475, https://doi.org/10.5194/acp-16-2459-2016, 2016.

Tangborn, A., Demoz, B., Carroll, B. J., Santanello, J., and Anderson, J. L.: Assimilation of lidar planetary boundary layer height observations, Atmos. Meas. Tech., 14, 1099–1110, https://doi.org/10.5194/amt-14-1099-2021, 2021.

Tennekes, H. and Tennekes, H.: A Model for the Dynamics of the Inversion Above a Convective Boundary Layer, J. Atmos. Sci., 30, 558–567, https://doi.org/10.1175/1520-0469(1973)030<0558:AMFTDO>2.0.CO;2, 1973.

Teschke, G. and Lehmann, V.: Mean wind vector estimation using the velocity–azimuth display (VAD) method: an explicit algebraic solution, Atmos. Meas. Tech., 10, 3265–3271, https://doi.org/10.5194/amt-10-3265-2017, 2017.

Theeuwes, N. E., Barlow, J. F., Teuling, A. J., Grimmond, C. S. B., and Kotthaus, S.: Persistent cloud cover over mega-cities linked to surface heat release, npj Climate and Atmospheric Science, 2, 1–15, https://doi.org/10.1038/s41612-019-0072-x, 2019.

Thobois, L., Freedman, J., Royer, P., Brotzge, J., and Joseph, E.: Validation and deployment of the first Lidar based weather observation network in New York State: The NYS MesoNet Project, EPJ Web Conf., 176, 09 010, https://doi.org/10.1051/epjconf/201817609010, 2018.

Thorne, P. W., Madonna, F., Schulz, J., Oakley, T., Ingleby, B., Rosoldi, M., Tramutola, E., Arola, A., Buschmann, M., Mikalsen, A. C., Davy, R., Voces, C., Kreher, K., De Maziere, M., and Pappalardo, G.: Making better sense of the mosaic of environmental measurement networks: a system-of-systems approach and quantitative assessment, Geoscientific Instrumentation, Methods and Data Systems, 6, 453–472, https://doi.org/10.5194/gi-6-453-2017, 2017.

Toledo, D., Córdoba-Jabonero, C., and Gil-Ojeda, M.: Cluster Analysis: A New Approach Applied to Lidar Measurements for Atmospheric Boundary Layer Height Estimation, J. Atmos. Oceanic Technol., 31, 422–436, https://doi.org/10.1175/JTECH-D-12-00253.1, 2014.

Toledo, D., Córdoba-Jabonero, C., Adame, J. A., De La Morena, B., and Gil-Ojeda, M.: Estimation of the atmospheric boundary layer height during different atmospheric conditions: a comparison on reliability of several methods applied to lidar measurements, International Journal of Remote Sensing, 38, 3203–3218, https://doi.org/10.1080/01431161.2017.1292068, 2017.

Tonttila, J., O'Connor, E. J., Hellsten, A., Hirsikko, A., O'Dowd, C., Järvinen, H., and Räisänen, P.: Turbulent structure and scaling of the inertial subrange in a stratocumulus-topped boundary layer observed by a Doppler lidar, Atmos. Chem. Phys., 15, 5873–5885, https://doi.org/10.5194/acp-15-5873-2015, 2015.

Träumner, K., Kottmeier, C., Corsmeier, U., and Wieser, A.: Convective Boundary-Layer Entrainment: Short Review and Progress using Doppler Lidar, Boundary-Layer Meteorol., 141, 369–391, https://doi.org/10.1007/s10546-011-9657-6, 2011.

Tsaknakis, G., Papayannis, A., Kokkalis, P., Amiridis, V., Kambezidis, H. D., Mamouri, R. E., Georgoussis, G., and Avdikos, G.: Intercomparison of lidar and ceilometer retrievals for aerosol and Planetary Boundary Layer profiling over Athens, Greece, Atmos. Meas. Tech., 4, 1261–1273, https://doi.org/10.5194/amt-4-1261-2011, 2011.

Tucker, S. C., Senff, C. J., Weickmann, A. M., Brewer, W. A., Banta, R. M., Sandberg, S. P., Law, D. C., and Hardesty, R. M.: Doppler lidar estimation of mixing height using turbulence, shear, and aerosol profiles, J. Atmos. Oceanic Technol., 26, 673–688, https://doi.org/10.1175/2008JTECHA1157.1, 2009.

Tuononen, M., O'Connor, E. J., Sinclair, V. A., and Vakkari, V.: Low-level jets over Utö, Finland, based on Doppler lidar observations, J. Appl. Meteor. Climatol., 56, 2577–2594, https://doi.org/doi:10.1175/JAMC-D-16-0411.1, 2017.

Turner, D. and Löhnert, U.: Information content and uncertainties in thermodynamic profiles and liquid cloud properties retrieved from the ground-based Atmospheric Emitted Radiance Interferometer (AERI), J. Appl. Meteor. Climatol., 53, 752–771, https://doi.org/10.1175/JAMC-D-13-0126.1, 2014.

Turner, D. D. and Blumberg, W. G.: Improvements to the AERIoe thermodynamic profile retrieval algorithm, IEEE Journal of Selected Topics in Applied Earth Observations and Remote Sensing, 12, 1339–1354, https://doi.org/10.1109/JSTARS.2018.2874968, 2018.

Turner, D. D. and Löhnert, U.: Ground-based temperature and humidity profiling: combining active and passive remote sensors, Atmos. Meas. Tech., 14, 3033–3048, https://doi.org/10.5194/amt-14-3033-2021, 2021.

Vajda, A., Tuomenvirta, H., Jokinen, P., Luomaranta, A., Makkonen, L., Tikanmäki, M., Groenemeijer, P., Saarikivi, P., Michaelides, S., Papadakis, M., Tymvios, F., and Athanasatos, S.: Probabilities of adverse weather affecting transport in Europe: Climatology and scenarios up to the 2050s, Clinical Epigenetics, https://doi.org/10.2/JQUERY.MIN.JS, 2011.

Vakkari, V., O'Connor, E. J., Nisantzi, A., Mamouri, R. E., and Hadjimitsis, D. G.: Low-level mixing height detection in coastal locations with a scanning Doppler lidar, Atmos. Meas. Tech., 8, 1875–1885, https://doi.org/10.5194/amt-8-1875-2015, 2015.

Vakkari, V., Manninen, A. J., O'Connor, E. J., Schween, J. H., van Zyl, P. G., and Marinou, E.: A novel post-processing algorithm for Halo Doppler lidars, Atmos. Meas. Tech., 12, 839–852, https://doi.org/10.5194/amt-12-839-2019, 2019.

van der Kamp, D. and McKendry, I.: Diurnal and Seasonal Trends in Convective Mixed-Layer Heights Estimated from Two Years of Continuous Ceilometer Observations in Vancouver, BC, Boundary-Layer Meteorol., 137, 459–475, https://doi.org/10.1007/s10546-010-9535-7, 2010.

Vivone, G., D'Amico, G., Summa, D., Lolli, S., Amodeo, A., Bortoli, D., and Pappalardo, G.: Atmospheric boundary layer height estimation from aerosol lidar: A new approach based on morphological image processing techniques, Atmos. Chem. Phys., 21, 4249–4265, https://doi.org/10.5194/ACP-21-4249-2021, 2021.

Vogelezang, D. H. P. and Holtslag, A. A. M.: Evaluation and model impacts of alternative boundary-layer height formulations, Boundary-Layer Meteorol., 81, 245–269, https://doi.org/10.1007/BF02430331, 1996.

von Engeln, A. and Teixeira, J.: A planetary boundary layer height climatology derived from ECMWF reanalysis data, J. Climate, 26, 6575–6590, https://doi.org/10.1175/JCLI-D-12-00385.1, 2013.

von Engeln, A., Teixeira, J., Wickert, J., and Buehler, S. A.: Using CHAMP radio occultation data to determine the top altitude of the Planetary Boundary Layer, Geophys. Res. Lett., 32, https://doi.org/10.1029/2004GL022168, 2005.

Wærsted, E. G., Haeffelin, M., Dupont, J. C., Delanoë, J., and Dubuisson, P.: Radiation in fog: Quantification of the impact on fog liquid water based on ground-based remote sensing, Atmos. Chem. Phys., 17, 10 811–10 835, https://doi.org/10.5194/ACP-17-10811-2017, 2017.

Wagner, T. J., Feltz, W. F., and Ackerman, S. A.: The temporal evolution of convective indices in storm-producing environments, Wea. Forecasting, 23, 786–794, https://doi.org/10.1175/2008WAF2007046.1, 2008.

Wagner, T. J., Klein, P. M., and Turner, D. D.: A new generation of ground-based mobile platforms for active and passive profiling of the boundary layer, Bull. Amer. Meteor. Soc., 100, 137–153, https://doi.org/10.1175/BAMS-D-17-0165.1, 2019.

Wang, D., Stachlewska, I. S., Song, X., Heese, B., and Nemuc, A.: Variability of the Boundary Layer Over an Urban Continental Site Based on 10 Years of Active Remote Sensing Observations in Warsaw, Remote. Sens., 12, 340, https://doi.org/10.3390/rs12020340, 2020.

Wang, X. Y. and Wang, K. C.: Estimation of atmospheric mixing layer height from radiosonde data, Atmos. Meas. Tech., 7, 1701–1709, https://doi.org/10.5194/amt-7-1701-2014, 2014.

Wang, Z., Cao, X., Zhang, L., Notholt, J., Zhou, B., Liu, R., and Zhang, B.: Lidar measurement of planetary boundary layer height and comparison with microwave profiling radiometer observation, Atmos. Meas. Tech., 5, 1965, https://doi.org/10.5194/amt-5-1965-2012, 2012.

Weckwerth, T. M., Weber, K. J., Turner, D. D., and Spuler, S. M.: Validation of a water vapor micropulse differential absorption lidar (DIAL), J. Atmos. Oceanic Technol., 33, 2353–2372, https://doi.org/10.1175/JTECH-D-16-0119.1, 2016.

Weitkamp, C.: LiDAR: introduction, in: Laser remote sensing, pp. 19–54, CRC Press, 2005.

Westwater, E. R., Crewell, S., and Mätzler, C.: A review of surface-based microwave and millimeter-wave radiometric remote sensing of the troposphere, URSI Radio Science Bulletin, 2004, 59–80, https://doi.org/10.23919/URSIRSB.2004.7909438, 2004.

White, A.: Mixing depth detection using 915-MHz radar reflectivity data, in: Eighth Symposium on Observations and Instrumentation. 8th Symposium on Meteorological Observations and Instrumentation, Anaheim, CA. American Meteorological Society, Boston MA, pp. 248–250, 1993.

Wiegner, M. and Geiß, A.: Aerosol profiling with the Jenoptik ceilometer CHM15kx, Atmos. Meas. Tech., 5, 1953–1964, https://doi.org/10.5194/amt-5-1953-2012, 2012.

Wiegner, M., Emeis, S., Freudenthaler, V., Heese, B., Junkermann, W., Münkel, C., Schäfer, K., Seefeldner, M., and Vogt, S.: Mixing layer height over Munich, Germany: Variability and comparisons of different methodologies, J. Geophys. Res. Atmos., 111, https://doi.org/10.1029/2005JD006593, 2006.

Wilczak, J. M., Cancillo, M. L., and King, C. W.: A wind profiler climatology of boundary layer structure above the boreal forest, J. Geophys. Res. Atmos., 102, 29 083–29 100, https://doi.org/10.1029/97JD02315, 1997.

Wildmann, N., Bodini, N., Lundquist, J. K., Bariteau, L., and Wagner, J.: Estimation of turbulence dissipation rate from Doppler wind lidars and in situ instrumentation for the Perdigão 2017 campaign, Atmos. Meas. Tech., 12, 6401–6423, https://doi.org/10.5194/amt-12-6401-2019, 2019.

Williams, A., Chambers, S., and Griffiths, A.: Bulk mixing and decoupling of the nocturnal stable boundary layer characterized using a ubiquitous natural tracer, Boundary-Layer Meteorol., 149, 381–402, https://doi.org/10.1007/s10546-013-9849-3, 2013.

WMO: GCOS, 144. Guide to the GCOS Surface Network (GSN) and GCOS Upper-Air Network (GUAN) World Meteorological Organization (WMO), Tech. Rep. GCOS–144, WMO/TD 1558, WMO/TD, https://library.wmo.int/doc_num.php?explnum_id=3855, 2010.

WMO: The GCOS Reference Upper-Air Network (GRUAN): Guide, http://library.wmo.int/pmb_ged/gcos_171.pdf, 2013.

WMO: Workshop on the Review of the GCOS Surface Network (GSN), GCOS Upper-Air Network (GUAN) and related atmospheric networks, https://library.wmo.int/opac/doc_num.php?explnum_id=4013, 2014.

WMO: WMO Global Observing System Upper-air observations, http://www.wmo.int/pages/prog/www/OSY/Gos-components.html#upper, 2017.

Wood, R.: Stratocumulus clouds, Mon. Wea. Rev., 140, 2373–2423, https://doi.org/10.1175/MWR-D-11-00121.1, 2012.

Woolway, R. I., Verburg, P., Merchant, C. J., Lenters, J. D., Hamilton, D. P., Brookes, J., Kelly, S., Hook, S., Laas, A., Pierson, D., et al.: Latitude and lake size are important predictors of over-lake atmospheric stability, Geophys. Res. Lett., 44, 8875–8883, https://doi.org/10.1002/2017GL073941, 2017.

Wu, Y., Zhao, K., Huang, J., Arend, M., Gross, B., and Moshary, F.: Observation of heat wave effects on the urban air quality and PBL in New York City area, Atmos. Environ., 218, 117 024, https://doi.org/10.1016/j.atmosenv.2019.117024, 2019.

Wulfmeyer, V., Pal, S., Turner, D. D., and Wagner, E.: Can Water Vapour Raman Lidar Resolve Profiles of Turbulent Variables in the Convective Boundary Layer?, Boundary-Layer Meteorol., 136, 253–284, https://doi.org/10.1007/s10546-010-9494-z, 2010.

Wulfmeyer, V., Hardesty, R. M., Turner, D. D., Behrendt, A., Cadeddu, M. P., Di Girolamo, P., Schlüssel, P., Van Baelen, J., and Zus, F.: A review of the remote sensing of lower tropospheric thermodynamic profiles and its indispensable role for the understanding and the simulation of water and energy cycles, Reviews of Geophysics, 53, 819–895, https://doi.org/10.1002/2014RG000476, 2015.

Xie, F., Wu, D. L., Ao, C. O., Mannucci, A. J., and Kursinski, E. R.: Advances and limitations of atmospheric boundary layer observations with GPS occultation over southeast Pacific Ocean, Atmos. Chem. Phys., 12, 903–918, https://doi.org/10.5194/acp-12-903-2012, 2012.

Yang, D., Li, C., Lau, A. K.-H., and Li, Y.: Long-term measurement of daytime atmospheric mixing layer height over Hong Kong, J. Geophys. Res. Atmos., 118, 2422–2433, https://doi.org/10.1002/jgrd.50251, 2013.

Yang, S., Petersen, G. N., von Löwis, S., Preißler, J., and Finger, D. C.: Determination of eddy dissipation rate by Doppler lidar in Reykjavik, Iceland, Meteor. Appl., 27, e1951, https://doi.org/10.1002/met.1951, 2020.

Yang, T., Wang, Z., Zhang, W., Gbaguidi, A., Sugimoto, N., Wang, X., Matsui, I., and Sun, Y.: Technical note: Boundary layer height determination from lidar for improving air pollution episode modeling: development of new algorithm and evaluation, Atmos. Chem. Phys., 17, 6215–6225, https://doi.org/10.5194/acp-17-6215-2017, 2017.

Yim, S. H. L.: Development of a 3D Real-Time Atmospheric Monitoring System (3DREAMS) Using Doppler LiDARs and Applications for Long-Term Analysis and Hot-and-Polluted Episodes, Remote. Sens., 12, 1036, https://doi.org/10.3390/rs12061036, 2020.

Zhang, W., Guo, J., Miao, Y., Liu, H., Zhang, Y., Li, Z., and Zhai, P.: Planetary boundary layer height from CALIOP compared to radiosonde over China, Atmos. Chem. Phys., 16, 9951–9963, https://doi.org/10.5194/acp-16-9951-2016, 2016.

Zhang, Y. and Klein, S. A.: Mechanisms affecting the transition from shallow to deep convection over land: Inferences from observations of the diurnal cycle collected at the ARM Southern Great Plains site, J. Atmos. Sci., 67, 2943–2959, https://doi.org/10.1175/2010JAS3366.1, 2010.

Zhang, Y. and Seidel, D. J.: Challenges in estimating trends in Arctic surface – based inversions from radiosonde data, Geophys. Res. Lett., 38, L17 806, https://doi.org/doi:10.1029/2011GL048728, 2011.

Zhang, Y., Seidel, D. J., and Zhang, S.: Trends in planetary boundary layer height over Europe, J. Climate, 26, 10 071–10 076, https://doi.org/10.1175/JCLI-D-13-00108.1, 2013.

Zhou, L., Tian, Y., Wei, N., Ho, S.-p., and Li, J.: Rising Planetary Boundary Layer Height over the Sahara Desert and Arabian Peninsula in a Warming Climate, J. Climate, 34, 4043–4068, https://doi.org/10.1175/JCLI-D-20-0645.1, 2021.